UNIVERSITÀ degli STUDI di VERONA

Dottorato di ricerca in
IMAGING MULTIMODALE IN MEDICINA
CICLO XXII

ADVANCED IMAGE-PROCESSING TECHNIQUES IN MAGNETIC RESONANCE IMAGING FOR THE INVESTIGATION OF BRAIN PATHOLOGIES AND TUMOUR ANGIOGENESIS

S.S.D. BIO/16

Coordinatore: Prof. Andrea Sbarbati

Firma ⎯⎯⎯⎯⎯⎯⎯⎯⎯⎯⎯⎯

Tutor: Dott.ssa Pasquina Marzola

Firma ⎯⎯⎯⎯⎯⎯⎯⎯⎯⎯⎯⎯

Dottorando: Dott. Alessandro Daducci

Firma ⎯⎯⎯⎯⎯⎯⎯⎯⎯⎯⎯⎯

Contents

Chapter 1

Introduction

Magnetic resonance imaging (MRI) is increasingly being used in medical settings because of its ability to produce, non-invasively, high quality images of the inside of the human body. Since its introduction in early 70's, more and more complex acquisition techniques have been proposed, raising MRI to be exploited in a wide spectrum of applications. Innovative MRI modalities, such as diffusion and functional imaging, require complex analysis techniques and advanced algorithms in order to extract useful information from the acquired data.

The aim of the present work has been to develop and optimize state-of-the-art techniques to be applied in the analysis of MRI data both in experimental and clinical settings. During my doctoral program I have been actively involved in several research projects, each time facing many different issues. In this dissertation, however, I will report the results obtained in three most appealing projects I partecipated to. These projects were devoted (i) to the implementation of an innovative experimental protocol for functional MRI in laboratory animals, (ii) to the development of new methods for the analysis of Dynamic Contrast Enhanced MRI data in experimental tumour models and (iii) to the analysis of diffusion MRI data in stroke patients. Particular emphasis will be given to the technical aspects regarding the algorithms and processing methods used in the analysis of data.

1.1 Outline of the thesis

Apart from a brief introduction on magnetic resonance imaging principles, the dissertation is organised in **three parts**, each one of them covering a separate topic dealt with during my doctoral studies. Each chapter is self-contained, in that it gives an introduction about the issue faced in the study, describes the methods and the techniques employed, and concludes with a discussion about the results obtained.

Chapter 3 illustrates the methodology proposed by our group for an innovative method of fMRI (Activation-Induced Manganese Enhanced MRI, AIM-MRI) in rats. The method is based on in-vivo, absolute quantification of Mn concentration in different brain regions performed by fast T_1 mapping and coreg-

istration to a rat brain atlas. This strategy allows to quantify the accumulation of Mn in different regions of the rat brain, which is strictly related to the activation status of each area. This mechanism is similar to what happens in classical functional MRI studies but, in addition, it might be used for functional experiments performed in awake animals.

In chapter 4 we cover the topic of tissues classification from MRI images in some experimental tumour models and present some advanced image-processing techniques we introduced for the analysis of Dynamic Contrast-Enhanced MRI (DCEMRI) data. In particular, we proposed to estimate a set of characteristic features from DCEMRI time profiles which well describe their shape, and then to extract peculiar behaviours which discriminate each tissue inside the tumour by combining cluster analysis and machine learning techniques. We have tested several approaches, each time comparing them with the state-of-the-art techniques of analysis for this kind of data. Finally, the proposed approach has been validated in a real case application in order to assess the efficacy of an anti-cancer therapy.

Chapter 5 addresses the study on post-stroke plasticity carried out in collaboration with the Signal Processing Laboratory of the Swiss Federal Institute of Technology in Lausanne (EPFL). Brain structural connectivity was monitored with Diffusion Spectrum Imaging (DSI), *i.e.* a high angular resolution diffusion MRI technique, during the functional recovery from the stroke, at hyperacute, acute and chronic stages after the lesion onset. The reproducibility of extracted fibre tracts has been extensively studied on healthy subjects, and the parameter set of fiber-tracking algorithm giving the best results was then used in patient analysis. The extracted fibre bundles between each pair of cortical regions were characterized by means of several connectivity measures.

Chapter 2

Magnetic Resonance Imaging

The aim of this chapter is to provide the reader with an overview on the basic principles behind image formation in *Magnetic Resonance Imaging* (MRI). First, we will briefly describe the underlying physics of *Nuclear Magnetic Resonance* (NMR) up to the image formation process. Then, we will discuss the principle of molecular self-diffusion and how it is related to the neuronal architecture of the brain. Diffusion can be measured by an adapted MRI experiment and we will show the connection between the physical principles of diffusion and imaging. We will then present different models of diffusion, in particular the *Diffusion Tensor* (DTI) and the *Diffusion Spectrum* (DSI) imaging.

2.1   NMR physical principles

Nuclei are composed of positively charged *protons* and uncharged *neutrons* held together by nuclear forces. Both protons and neutrons have approximately the same mass, which is about 1840 times as large as the mass of an *electron*, which is negatively charged. Protons, neutrons and electrons possess also an *angular momentum* known as **spin**, which is a fundamental property of nature like electrical charge or mass. Spin comes in multiples of $\pm\frac{1}{2}$. Individual unpaired electrons, protons, and neutrons each possesses a spin of $\frac{1}{2}$. Two or more particles with spins having opposite signs can cancel out each other, such as helium nucleus. This means that only atoms with a net spin can be NMR-active. Anyway, almost every element in the periodic table has an isotope with a non zero nuclear spin. Table 2.1 reports the most-used nuclei exploited in NMR experiments.

Nuclei	γ $_{(MHz/T)}$	% in human body
^{1}H	42.58	0.63
^{31}P	17.25	0.0024
^{13}C	10.71	0.094
^{23}Na	11.27	0.00041

TABLE 2.1: Most-used nuclei in NMR/MRI experiments.

2.1.1 Spin physics

In the presence of an **external magnetic field B_0**, each spin behaves like a small magnetic bar. It aligns almost parallel to the direction of the field (*i.e.* the same way a compass aligns to the magnetic field of the earth). Because of quantum mechanics laws, the behaviour is a bit different from a compass needle. The spin does not align perfectly to the field B_0: due to the torque it experiences from the external magnetic field, it will precess around the field axis, as shown in figure 2.1. The frequency of this **precession motion**, also known as the *Larmor frequency ω_0*, is given by:

$$\omega_0 = \gamma B_0 \tag{2.1}$$

where γ is the *gyromagnetic ratio* specific for each kind of nucleus. Table 2.1 reports γ values for the most-used nuclei.

In an external magnetic field the number of possible values for the angular momentum is $2I + 1$, where I is the *spin quantum number*. The most typical nucleus used in NMR experiments is the **hydrogen nucleus**, which has $I = \frac{1}{2}$. This means ^1H can have two possible orientations, parallel and anti-parallel to B_0 (*i.e.* spin-up and spin-down respectively). These two states possess slightly different energy levels. Populations of the two levels are dependent on both the external magnetic field and temperature. At $37\,^\circ C$ and $1.5\,T$ field strength, the ratio between the two energy levels is 1.000004, so slightly more protons are in the spin-up state. The average of the magnetisation of each proton will give a net magnetisation aligned exactly along the B_0 field.
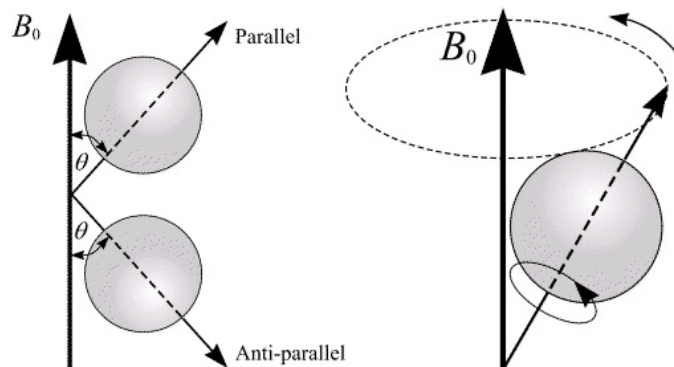
FIGURE 2.1: Each proton aligns parallel, spin $+\frac{1}{2}$, or anti-parallel, spin $-\frac{1}{2}$, and precesses in the external magnetic field B_0. (*image from http://www.easymeasure.co.uk*)

Since the signal of one spin is impossible to measure, spins are generally considered as an ensemble, or *spin-packet*, and are described in terms of precession around a **spin magnetisation vector M**. A spin-packet is a group of spins experiencing the same magnetic field strength. When no external field is applied, ^1H spins are randomly distributed between the spin-up $(+\frac{1}{2})$ and spin-down $(-\frac{1}{2})$ positions, and thus the net spin of the ensemble equals zero. In the presence of an external magnetic field B_0, the spin magnetisation vector M will align itself with the field and the spins start precessing around B_0.

When considering a spin system it is handy to define a *laboratory frame* in which $\mathbf{M}$ appears to be stationary and aligned with $\mathbf{B_0}$. Adopting the conventional NMR coordinate system, the external magnetic field $\mathbf{B_0}$ and the net magnetisation vector $\mathbf{M}$ are both along the z-axis at equilibrium, and the plane orthogonal to the z-axis is the transverse xy-plane.

2.1.2 Measuring the signal

In order to obtain a measurable signal from an NMR experiment the system must absorb energy that can later be emitted and measured. To achieve this, it is possible to induce transitions between the two energy levels, *i.e.* spin-up and spin-down states, exciting the system with an **additional time-varying rotating magnetic field $\mathbf{B_1}$**, generated by a radio-frequency (RF) pulse, acting perpendicular to $\mathbf{B_0}$ and oscillating at the Larmor frequency ω_0.

The RF-pulse tilts $\mathbf{M}$ away from the z-axis and $\mathbf{M}$ starts precessing about the rotating $\mathbf{B_1}$ field. The tip-angle α between $\mathbf{M}$ and the z-axis depends on the duration τ of the RF-pulse and is given by:

$$\alpha = \gamma \mathbf{B_1} \tau \tag{2.2}$$

The cases $\alpha = 90°$ and $\alpha = 180°$ are the most commonly used in NMR experiments. A 90° *pulse* tilts the magnetisation vector $\mathbf{M}$ onto the transverse xy-plane, whilst the 180° *pulse* inverts $\mathbf{M}$ along the longitudinal z-axis.
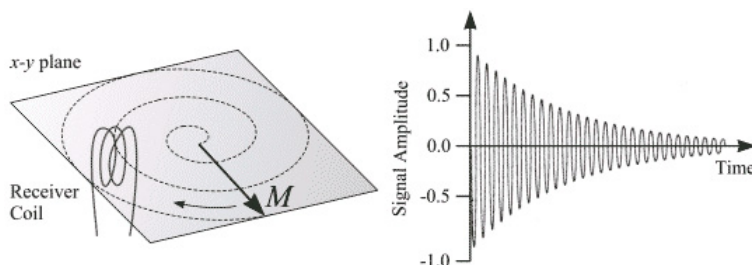
FIGURE 2.2: Signal measurement. The transverse magnetisation induces a current in the receiver coil and the signal is collected. The signal decays over time for relaxation processes. (*image from http://www.easymeasure.co.uk*)

When an RF pulse α is applied to tilt the magnetisation $\mathbf{M}$ away from its equilibrium state, $\mathbf{M}$ can be split into its components: $\mathbf{M_\perp}$ and $\mathbf{M_z}$. Once the RF pulse is removed, $\mathbf{M}$ falls back to its initial position aligned with $\mathbf{B_0}$, *i.e.* $\mathbf{M_z} = \mathbf{M}$ and $\mathbf{M_\perp} = \mathbf{0}$. This process is called relaxation and is discussed in section 2.1.3. During this relaxation process the energy that has been added to the system by the RF pulse is emitted back and can thus be detected. In fact, according to *Faradays's law*, the transverse magnetisation $\mathbf{M_\perp}$ generates a current in a receiver coil onto the xy-plane. The induced signal is called the **free induction decay** (FID). Over time the signal decays while the net magnetisation returns to its equilibrium state, as shown in figure 2.2.

2.1.3 T_1 and T_2 relaxation

There are two mechanisms that make the net magnetisation return to its equilibrium value, the *spin-lattice* (or T_1) and the *spin-spin* (or T_2) relaxation. The difference in the physical properties of different tissue types is reflected in the relaxation times. Relaxation is the mechanism that generates the contrast between different tissue in MRI. Figure 2.3 shows some example images.
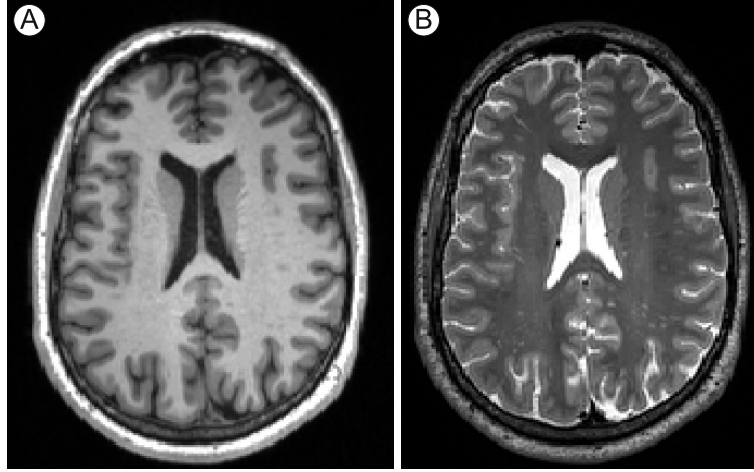
FIGURE 2.3: Images with different contrast. The same slice has been acquired both with T_1-weighted (**A**) and T_2-weighted (**B**) contrast.

The **spin-lattice relaxation** process involves the exchange of energy between the spin-system and the surroundings. At equilibrium, the net magnetisation vector lies along the direction of the applied magnetic field $\mathbf{B_0}$ and is called the equilibrium magnetisation $\mathbf{M_0}$. In this configuration, the z-component of magnetisation $\mathbf{M_z}$ equals $\mathbf{M_0}$. There is no transverse ($\mathbf{M_\perp}$) magnetisation here. The equation governing this behaviour as a function of the time t after its displacement is:

$$\mathbf{M_z} = \mathbf{M_0}(1 - e^{-t/T_1}) \tag{2.3}$$

The time constant which describes how $\mathbf{M_z}$ returns to its equilibrium value is called the *spin-lattice relaxation time*, or T_1. T_1 is the time to reduce the difference between the longitudinal magnetisation ($\mathbf{M_z}$) and its equilibrium value ($\mathbf{M_0}$) by a factor of e.

The **spin-spin relaxation** is the process where neighbouring spins come to thermal equilibrium with themselves. In addition to the precession around field $\mathbf{B_0}$, the net magnetisation starts to dephase because each of the spin-packets making it up is experiencing a slightly different magnetic field and rotates at its own Larmor frequency. The longer the elapsed time, the greater the phase difference. The equation governing this behaviour as a function of the time t after its displacement is:

$$\mathbf{M_\perp} = \mathbf{M_{\perp_0}} e^{-t/T_2} \tag{2.4}$$

The time constant which describes the return to equilibrium of the transverse magnetisation, $\mathbf{M_\perp}$, is called the *spin-spin relaxation time*, or T_2. T_2 is the time to reduce the transverse magnetisation by a factor of e.

Actually, the decay of transverse magnetisation $\mathbf{M}_\perp$ is more complicated. In fact two distinct factors contribute to the dephasing of the magnetisation:

- molecular interactions (pure T_2 molecular effect);

- variations in $\mathbf{B_0}$ (inhomogeneous T_2 effect, or $T_2^\sim$).

The combination of these two factors is what actually results in the decay of the transverse magnetisation. The combined time constant is called T_2^*. The relationship between the T_2 from molecular processes and that from inhomogeneities in the magnetic field is as follows:

$$\frac{1}{T_2^\star} = \frac{1}{T_2} + \frac{1}{T_2^\sim}. \tag{2.5}$$

2.2 Image formation and k-space

As previously mentioned, the Larmor frequency is dependent on the external field. In order to produce small variations in $\mathbf{B_0}$ field, gradient coils are employed in MRI scanners. By using such **polarizing gradient fields**, *i.e.* $\mathbf{G_x}$, $\mathbf{G_y}$ and $\mathbf{G_z}$, varying linearly along a particular axis (x, y and z respectively) but constant in time, the Larmor frequency of each spin-packet changes depending on its position. These variations are used to locate where the emitted signal from each spin-packet originates. Figure 2.4 illustrate this process.
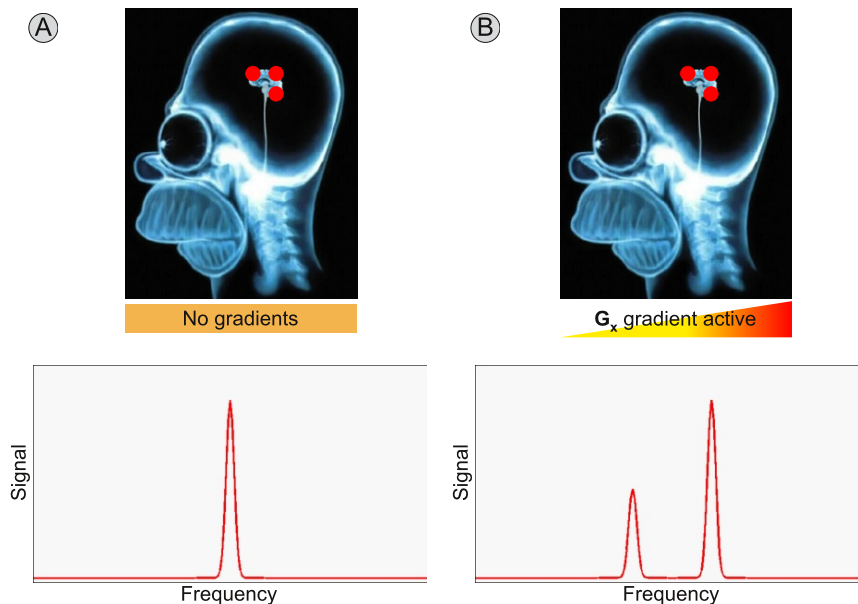
FIGURE 2.4: Spatial encoding. If no gradient is applied (**A**), all the spin-packets (red dots) are experiencing the same magnetic field $\mathbf{B_0}$, so there is only one peak in the NMR spectrum. If a linear gradient $\mathbf{G_x}$ is applied along the x-axis (**B**), spin-packets at different x locations are experiencing different magnetic field strength, *i.e.* $\mathbf{B_0} + x\mathbf{G_x}$, thus in the NMR spectrum there will be two separate peaks. The amplitude of the signals is proportional to the number of spins in a plane perpendicular to the gradient.

Due to this effect, a **slice selection** can be made by letting $\mathbf{B_1}$ oscillate with different frequencies dependent on the choice of the slice to excite. This is achieved by applying a linear magnetic field gradient during the period of application of the RF pulse $\mathbf{B_1}$. A 90° RF pulse contains a band of frequencies. When it is applied in conjunction with a magnetic field gradient, it will rotate only those spins located in the selected frequency band, because only the spins excited with the proper Larmor frequency will be affected by the RF pulse. In fact, when the slice selection gradient $\mathbf{G_z}$ is turned on, the effective magnetic field experienced at the position z is:

$$\mathbf{B}_{\text{eff}} = \mathbf{B_0} + z\mathbf{G_z} \tag{2.6}$$

and thus the resonance frequency of the spins is dependent on their position along the z-axis, and equals to:

$$\omega_{\text{eff}} = \gamma(\mathbf{B_0} + z\mathbf{G_z}) \tag{2.7}$$

Once all spins inside a slice have been selected, the problem of spatially locate them in the transverse xy-plane is still open. Generally, a **phase-encoding gradient $\mathbf{G_y}$** is first applied perpendicular to the slice gradient for a fixed amount of time τ, which introduces a *phase-shift* in the FID signal dependent on the position along the y-axis. The phase-shift is due to the difference in frequency that varies with position, and is given by:

$$\varphi(y) = \gamma(y\mathbf{G_y})\tau \tag{2.8}$$

where τ is the time over which G_y is applied. During the time $\mathbf{G_y}$ is on, spins located in regions where the $\mathbf{G_y}$ strength is high will precess faster than in regions of lower $\mathbf{G_y}$. Thus, when the field gradient is turned off, the frequencies will return to their initial values, but the phase-shifts accumulated in the time τ between nuclei at different positions on the y-axis persist.

The final gradient to be exploited in order to retrieve the spatial location of the spins is the **frequency-encoding gradient $\mathbf{G_x}$**, (also called *read gradient*). This gradient is applied perpendicular to both slice and phase gradients, to form a three dimensional coordinate system, and is turned on while the signal is being sampled. This way, the frequencies of the spins will change again, depending on their position along the x-axis. Once again, the position of the spin is encoded by letting the resonance frequency of each spin to be proportional to its position along the x-axis:

$$\mathbf{B}_{\text{eff}} = \mathbf{B_0} + x\mathbf{G_x} \tag{2.9}$$

Figure 2.5 shows a diagram summarizing the main steps involved in the acquisition of an MRI image.

The resulting signal after successively applying $\mathbf{G_z}$, $\mathbf{G_y}$ and $\mathbf{G_x}$ corresponds to the Fourier-transform of the transverse magnetization $\mathbf{M_\perp}$. This reconstruction method is the so called **Fourier Transform imaging**.

In order to make the Fourier relation between the signal and the magnetization more obvious, a reciprocal spatial frequency space, known as *k-space*, is introduced. The measured signal for a set of gradients, $\mathbf{G_z}$, $\mathbf{G_y}$ and $\mathbf{G_x}$, produces a
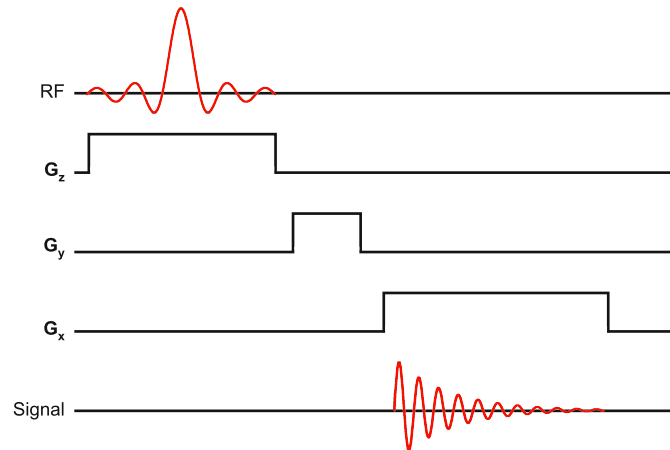
FIGURE 2.5: Diagram of a typical imaging sequence for sampling k-space. The gradient $\mathbf{G_z}$ is responsible for the slice selection, while $\mathbf{G_x}$ and $\mathbf{G_y}$ are responsible for frequency and phase encoding, respectively.

single line in the k-space. Applying repeatedly these gradients in different combinations leads to different samplings of the k-space. Once the k-space has been sampled, the MR image is obtained by applying the inverse Fourier transform.

2.3 Diffusion MRI

Water diffusion in living tissues is highly affected by its cellular organisation. In the brain, experimental evidence suggests that the tissue component mainly responsible for the anisotropy[1] of molecular diffusion observed in white matter is not *myelin*, as one might expect, but rather the *cell membrane* [1]. The degree of myelination of the individual axons and the density of cellular packing seem merely to modulate anisotropy. Furthermore, axonal transport, microtubules, and neurofilaments appear to play only a minor role in anisotropy measured with MR imaging (see figure 2.6).
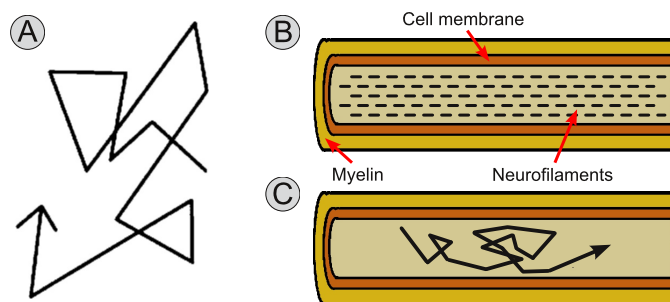
FIGURE 2.6: In a glass of water, the diffusion random motion of water molecules is unrestricted (**A**). Axonal *cell membrane* (**B**) is the main component restricting water diffusion. Thus, even though inside axones (**C**) the diffusion remains a random process, the main diffusion direction is along the axis of the axon.

---

[1]Having properties that differ according to the direction of measurement

Imaging the diffusion process in-vivo gives therefore an insight of the microstructure of the tissue. Anisotropic diffusion in white matter can be used for mapping neuronal connectivity, and structures invisible with other imaging modalities can be localised due to the information contained in the diffusion. Diffusion imaging is therefore a valuable tool to improve our current knowledge of the brain.

2.3.1 What is diffusion?

Diffusion is a mass transport process arising in nature, which results in molecular or particle mixing without requiring bulk motion. Let's imagine to introduce a drop of ink into a glass of water. Initially, the ink appears to remain concentrated at the initial point, but over time it spreads radially, in a spherically symmetric profile. This mixing process takes place without stirring or other bulk motion. The physical law that explains this phenomenon is called **Fick's first law**:

$$\mathbf{J} = -\mathsf{D} \cdot \nabla C \tag{2.10}$$

where $\mathbf{J}$ is the net particle flux, ∇C is the gradient in particles concentration, and the constant of proportionality, D, is called the *diffusion coefficient*. The diffusion coefficient D is an intrinsic property of the medium, and its value is determined by the size of the diffusing molecules and the temperature and micro structural features of the environment in which they lie. The diffusion coefficient for water at 37°C is approximately $\mathsf{D} = 3 \cdot 10^{-3}$ mm^2/s. Thus, if we observe water molecules for, say, 30 ms, they will have displaced, on average, 25 μm in all directions

By the way, a surprising feature of diffusion is that it occurs even in thermodynamic equilibrium, for example in a glass of water kept at a constant temperature and pressure. This appears to be in contrast with the classic way to describe the diffusion process, as expressed above in the Fick's law. This random-motion phenomenon was observed for the first time by **Robert Brown** in 1828; he reported that particles moved randomly without any apparent cause. He stated this by simply observing random movements of pollen grains with his microscope. However, he was unaware of the existence of atoms.

One century later, Albert Einstein used a probabilistic framework to describe the motion of an ensemble of particles undergoing diffusion, which led to a coherent description of diffusion, reconciling the Fickian and Brownian pictures. He introduced the *probability density function* for this purpose (see figure 2.7), which quantifies the fraction of particles that will traverse a certain distance, r, within a particular time-frame, t, or equivalently, the likelihood that a single given particle will undergo that displacement. Provided that the number of particles is sufficiently large and they are free to diffuse, Einstein was able to derive an explicit relationship between the mean-squared displacement of the ensemble, characterising its Brownian motion, and the classical diffusion coefficient D, appearing in Fick's law, given by the so called **Einstein's equation**:

$$\langle r^2 \rangle = 6\mathsf{D}t \tag{2.11}$$

where $\langle r^2 \rangle$ is the mean-squared displacement during the observation time t.
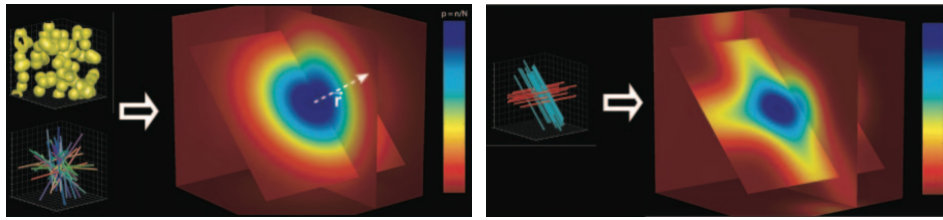
FIGURE 2.7: 3D diffusion *probability density function* within a voxel: containing water or randomly oriented structures that intersect (LEFT) or containing two populations of fibres intersecting at 90° angle (RIGHT). Probability ranges from **low** to **high**.

2.3.2 Diffusion Weighted Imaging

Diffusion Weighted Imaging, or DWI, is the simplest form of diffusion imaging. Despite its simplicity, diffusion-weighted imaging is routinely used in investigations of stroke. Indeed, in acute stroke, the local cell swelling produces increased restriction of water mobility and hence a bright imaging appearance due to high signal intensity in the area of the lesion. Furthermore, a diffusion-weighted image is one of the components needed to reconstruct the complete *probability density function* with more complex diffusion MRI techniques, as we will see later in the chapter.
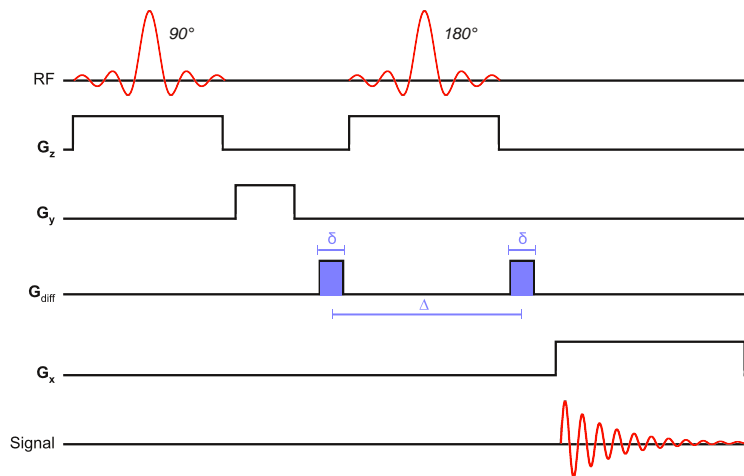
FIGURE 2.8: Standard *diffusion weighted imaging sequence*. Two diffusion gradients pulses ($\mathbf{G_{diff}}$) are added to the classical Spin-Echo sequence ($90° - 180°$) to introduce a phase shift proportional to molecular displacement along the gradient direction.

As shown in figure 2.8, diffusion-weighted sequences are made sensitive to diffusion by the insertion of two additional magnetic field gradient pulses, or **diffusion gradients**, besides the standard $\mathbf{G_x}$, $\mathbf{G_y}$ and $\mathbf{G_z}$ used for spatial encoding. The first of the two gradient pulses in this sequence introduces a phase-shift that is dependent on the strength of the gradient at the position of the spin at $t = 0$. Before the application of the second gradient pulse, which induces another phase-shift dependent on the spin position at $t = \Delta$, a 180° RF pulse is applied to reverse the phase-shift induced by the first gradient pulse.

As long as spins remain stationary, *i.e.* remain at the same location along the gradient axis between the two pulses, the net phase accumulation will be constant irrespective of their position and therefore they will return to their initial state. However, spins that have moved will be subjected to a different field strength during the second pulse and therefore will not return to their initial state but will experience a nonzero phase-shift. If all spins underwent the same net displacement, they would all undergo the same phase change, such that, although the phase had changed, the signal would remain coherent and there would be no concomitant drop in signal amplitude. Under the diffusion process, however, we get a distribution of displacements and thus a distribution of phases. This phase dispersion leads to a loss of coherence and therefore a **reduction in signal amplitude**. The wider the spread of displacements, the greater the loss of signal.

The b-value

In diffusion imaging, b-**value** is often used for describing the diffusion sequence that has been used for the image acquisition. b-value, or simply b, is a quantity which quantifies the degree of diffusion that have been applied in the sequence. For the specific sequence shown in figure 2.8, b equals to:

$$b = \gamma^2 \cdot |\mathbf{G_{diff}}|^2 \cdot \delta^2 \cdot \left(\Delta - \frac{\delta}{3}\right) \tag{2.12}$$

where $|\mathbf{G_{diff}}|$ is the amplitude of the magnetic field gradient pulses $\mathbf{G_{diff}}$, and δ and Δ are their duration and temporal separation, respectively.

It is worth noting that, although the real separation between the two pulses is Δ, the *effective diffusion time* is $t = (\Delta - \delta/3)$, where $\delta/3$ is a correction due to the diffusion which occurs while the gradient pulse is applied. Diffusion motions occurring during the gradient pulse are difficult to quantify, so the smaller the pulses are, the more precise the information about diffusion will be. Even if very short pulse gradients are practically unfeasible, we will try to make them as small as possible, $\delta \ll \Delta$, to be able to consider the displacements during the gradient pulse negligibly small.

Estimation of the diffusion coefficient

So far, we have made the assumption that the molecules are free to move. However, if the diffusing water *molecules encounter any hindrances* along their random walk, such as cell membranes and macromolecules, the mean squared displacement per unit time will be lower than when observed in free water. If we apply Einstein's equation to compute the diffusion coefficient, it will *appear* that the diffusion coefficient D is lower than expected. Thus, the physical diffusion coefficient D is replaced by the *Apparent Diffusion Coefficient*, ADC, which could be estimated from the equation:

$$I_b = I_0 \cdot \exp\left(-b \cdot \mathsf{ADC}\right) \tag{2.13}$$

where I_b is the diffusion-weighted image acquired with a specific b value and I_0 is a reference image without diffusion weighting.

The problem of diffusion-weighted imaging is that the interpretation of the resulting images is not intuitive. In fact, the ADC is strictly dependent on the direction of diffusion encoding, as shown in figure 2.9. To overcome this limitation, one can perform three orthogonal measurements and average the result to obtain a better approximation of the diffusion coefficient.
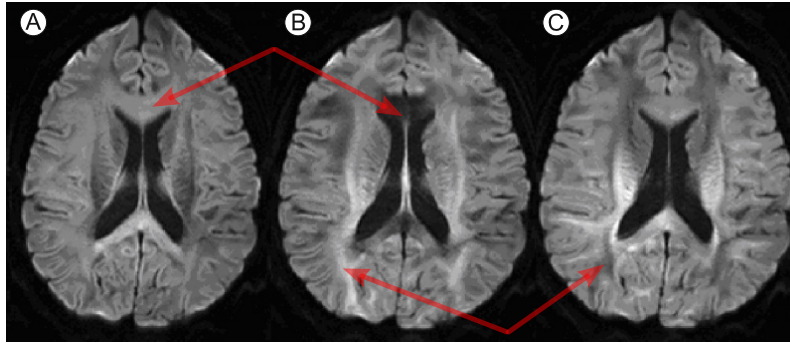
FIGURE 2.9: DWI images obtained, for the same slice, with diffusion gradients oriented in the Inferior-Superior (**A**), *i.e.* through the plane, Left-Right (**B**) and Anterior-Posterior (**C**) direction, respectively. (*image from http://www.med.lu.se*)

2.3.3 Diffusion Tensor Imaging

For the measurement of the coefficient of diffusion, we have assumed that diffusion follows a free-diffusion physical model and is described by an isotropic Gaussian distribution. This model often is too simplistic, especially if we are interested in the orientation of axonal bundles in which diffusion is expected to be anisotropic. Isotropic diffusion has a constant diffusion coefficient, ADC, but when the diffusion varies with directions it is anisotropic and must be modelled with a tensor, **D**.

The *diffusion tensor imaging* (DTI) formalism was introduced by Basser in 1994 [2, 3]. This approach was the first one to provide a unified description of the diffusion from a series of diffusion weighted images. Basser proposed to fit a second order *tensor* to the diffusion data in every voxel to characterise the shape of the underlying diffusion process, as in figure 2.10.
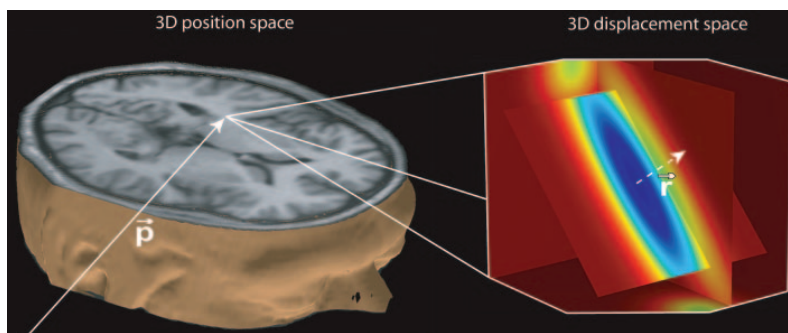
FIGURE 2.10: In *diffusion tensor imaging* every 3D position is associated with a 3D image that encodes the molecular displacement distribution in that voxel.

This **diffusion tensor**, $\mathbf{D}$, is a 3×3 symmetric, semi-positive definite matrix that characterises displacements in three dimensions:

$$\mathbf{D} = \begin{bmatrix} D_{xx} & D_{xy} & D_{xz} \\ D_{xy} & D_{yy} & D_{yz} \\ D_{xz} & D_{yz} & D_{zz} \end{bmatrix} \tag{2.14}$$

The *diagonal elements* of this matrix correspond to diffusivities along three orthogonal axes, while the *off-diagonal* elements correspond to the correlation between displacements along those orthogonal axes. The diffusion tensor $\mathbf{D}$ fully characterises the variation of the diffusion dependent on direction. In fact, $\mathbf{D}$ can be viewed as the three-dimensional **covariance matrix of displacements** in a given time. It is important to realise that, for example, D_{xy} is not the apparent diffusion coefficient measured with a diffusion-encoding gradient applied along the xy-axis; instead, D_{xy} correlates displacements along the x and y-axes.

DTI model is based on the hypothesis that the diffusion is unrestricted and can therefore be modelled by a Gaussian distribution. For purposes of this introduction, then, let us assume that diffusion remains Gaussian but may be anisotropic. In other words, diffusion may be cigar or disc shaped but also may be spherical, as in isotropic diffusion.

The diffusion ellipsoid

By diagonalising the diffusion tensor $\mathbf{D}$, we obtain its *eigenvalues* $(\lambda_1, \lambda_2, \lambda_3$ where $\lambda_1 \geq \lambda_2 \geq \lambda_3)$ and the corresponding *eigenvectors* $(\mathbf{e_1}, \mathbf{e_2}, \mathbf{e_3})$. Since the tensor is symmetric and semi-positive definite, the eigenvalues are always non-negative even though noise can destroy its semi-positivity. The largest eigenvalue and its corresponding eigenvector describe the quantity and direction of the principal diffusion, respectively.
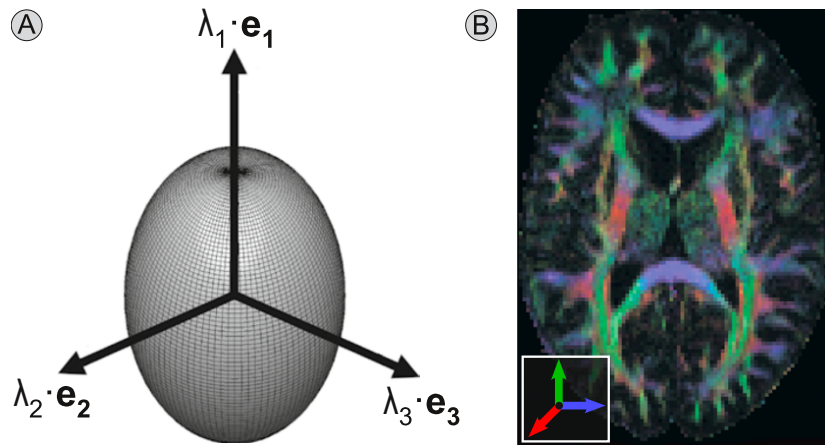
FIGURE 2.11: Diffusion tensor visualisation. In (A) the tensor is represented as an *ellipsoid* whose shape is controlled by its eigenvectors/eigenvalues. In (B) a *color-coded map* is used: RGB colors are used to represent **Inferior-Superior**, **Anterior-Posterior** and **Left-Right** components of the main diffusion direction, respectively.

The diffusion tensor is normally visualised as an **ellipsoid**, as in figure 2.11 A, with the principal axes along the eigenvectors of the tensor **D**, *i.e.* $\mathbf{e_1}, \mathbf{e_2}$ and $\mathbf{e_3}$, and with the length of these axes proportional to the corresponding eigenvalues, *i.e.* λ_1, λ_2 and λ_3. An anisotropic tensor has a distinct cigar shaped look whereas an isotropic tensor approaches the shape of the sphere.

Another practical way of visualising diffusion tensors fields is the so called **color-coded map**. For each voxel, the principal diffusion direction, *i.e.* the one corresponding to the greatest eigenvalue of the tensor **D**, is decomposed into its 3 orthogonal components. Then each component is assigned to a separate channel of an RGB image and the intensity is determined by the *fractional anisotropy* (introduced later in this chapter). In figure 2.11 B, for example, the red channel represents Inferior-Superior direction (I-S), while green and blue channels represent Anterior-Posterior (A-P) and Left-Right axes (L-R), respectively. With this convention, for instance, violet pixels can be seen as water molecules which moves in a L-R/I-S direction.

Estimation of the diffusion tensor

Anisotropic Gaussian distributions have 6 degrees of freedom (rotation and scale) and thus there are only *six unknown elements to determine*. These are estimated from a series of diffusion-weighted images acquired with gradients applied in non-collinear and non-coplanar directions [2, 3]. According to linear algebra, in order to find n unknown variables, at least n simultaneous equations should be solved. The same applies when estimating the diffusion tensor from MR data. Hence, at least 6 diffusion-weighted images must be acquired with gradients applied in *non-collinear and non-coplanar directions*, together with an additional reference non-diffusion-weighted image.

A key component in the estimation of the tensor is the calculation of the relationship between the signal attenuation and the elements of the diffusion tensor for a given gradient amplitude, duration, and separation. As the tensor is a 3×3 matrix, this coupling also takes the form of a 3×3 matrix. In analogy to the scalar b-value used when estimating the scalar ADC coefficient, this matrix is called the $\boldsymbol{b}$**-matrix**, **B**. For details on derivation of this b-matrix, please refer to [4]. Equation 2.13 can thus be rewritten for anisotropic media as:

$$I_{\mathbf{B}} = I_0 \cdot \exp\left(\begin{bmatrix} -b_{xx} \cdot D_{xx} & -b_{yy} \cdot D_{yy} & -b_{zz} \cdot D_{zz} \\ -2b_{xy} \cdot D_{xy} & -2b_{xz} \cdot D_{xz} & -2b_{yz} \cdot D_{yz} \end{bmatrix} \right) \qquad (2.15)$$

where $b_{xx}, \ldots, b_{zz}$ and $D_{xx}, \ldots, D_{zz}$ are the components of the b-matrix **B** and the tensor **D**, respectively.

The simplest estimation approach is by means of **linear algebra**. If $\mathbf{S} = [s_1, s_2, \ldots, s_N]$ is a vector of the log-transformed signal intensities, **B** is a $(N\times6)$ matrix containing the unique elements of the b-matrix for each measurement,

$$\mathbf{B} = \begin{pmatrix} b_{xx}^1 & b_{xy}^1 & b_{xz}^1 & b_{yy}^1 & b_{yz}^1 & b_{zz}^1 \\ \vdots & \vdots & \vdots & \vdots & \vdots & \vdots \\ b_{xx}^N & b_{xy}^N & b_{xz}^N & b_{yy}^N & b_{yz}^N & b_{zz}^N \end{pmatrix}$$

and $\mathbf{D}$ is a vector containing the elements of the diffusion tensor,

$$\mathbf{D} = \begin{bmatrix} D_{xx} & D_{xy} & D_{xz} & D_{yy} & D_{yz} & D_{zz} \end{bmatrix}^{\mathrm{T}}$$

then we can summarise the relationship between the observed signals $\mathbf{S}$ and the diffusion tensor $\mathbf{D}$ as:

$$\mathbf{S} = \mathbf{BD}$$

Therefore, we can estimate $\mathbf{D}$ by simply taking the **inverse of B**:

$$\mathbf{D} = \mathbf{B}^{-1}\mathbf{S} \tag{2.16}$$

Of course, this approach is fine if we have exactly six measurements such that the matrix $\mathbf{B}$ is square. It is usual, however, to acquire more than the bare minimum number of measurements in order to improve SNR of the data. In this case, since the matrix $\mathbf{B}$ is no longer square, the tensor is computed by calculating the **pseudo-inverse of B**:

$$\mathbf{D} = (\mathbf{B}^{\mathrm{T}}\mathbf{B})^{-1}\mathbf{B}^{\mathrm{T}}\mathbf{S} \tag{2.17}$$

Scalars derived from the diffusion tensor

The most clinically useful measure obtained from DTI is currently the *trace* of the diffusion tensor. The trace is the sum of the three diagonal elements of the diffusion tensor, *i.e.* $\mathrm{tr}(\mathbf{D}) = D_{xx} + D_{yy} + D_{zz}$, which can be shown to be equal to the sum of its three eigenvalues (*i.e.* $\lambda_1 + \lambda_2 + \lambda_3$). A very important quantity related to the trace is the **mean diffusivity**, which is given by:

$$\mathsf{MD} = \frac{\mathrm{trace}(\mathbf{D})}{3} = \frac{D_{xx} + D_{yy} + D_{zz}}{3} \tag{2.18}$$

MD can be thought of as the orientationally averaged mean diffusivity, and is high-valued in areas of strong diffusion, such as the ventricles in figure 2.12 A.
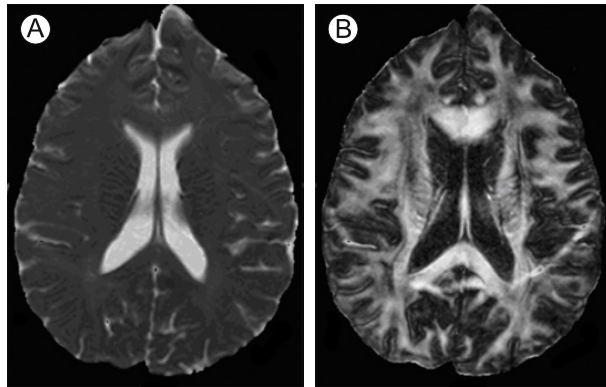
FIGURE 2.12: DTI scalar maps. *Mean diffusivity* (A) and *fractional anisotropy* (B) are the two most important scalars extracted from diffusion tensors.

Another important measure which is possible to obtain from DTI data is the **fractional anisotropy**, FA. The relationship between the eigenvalues of the

tensor reflects the directional characteristics of diffusion. To describe the shape of diffusion with a scalar value, FA is the most commonly used anisotropy index in the literature, and is calculated as follow:

$$\mathsf{FA} = \sqrt{\frac{3}{2}} \frac{\sqrt{(\lambda_1 - \overline{\lambda})^2 + (\lambda_2 - \overline{\lambda})^2 + (\lambda_3 - \overline{\lambda})^2}}{\sqrt{\lambda_1^2 + \lambda_2^2 + \lambda_3^2}} \qquad (2.19)$$

where $\overline{\lambda} = (\lambda_1 + \lambda_2 + \lambda_3)/3 \equiv \mathsf{MD}$ is the mean of the three eigenvalues. FA is properly normalised so that it ranges from 0 (when diffusion is isotropic, *e.g.* inside the ventricles) to 1 (when diffusion is constrained along one axis only, *e.g.* in white matter). Figure 2.12 B shows an example of FA map.

2.3.4 High Angular Resolution Diffusion Imaging

The DTI model performs well in regions where there is only one fibre population (*i.e.* fibres are aligned along a single axis), where it gives a good depiction of the fibre orientation. However, it fails in regions with several fibre populations aligned along intersecting axes, because it cannot be used to map several diffusion maxima at the same time. In such areas, imaging techniques that provide higher angular resolution are needed.

The *q*-space

According to basic MR imaging principles seen in section 2.2, the signal measured with conventional MR imaging is phase and frequency encoded. It is the result of the application of gradients in different directions and with different intensities. The values of the measured signal are organised in a coordinate system known as *k-space*. To transform the acquired rawdata from k-space into a position-encoded visual image, the Fourier transform is applied.

The process in diffusion MRI is analogous. Let us first define a new 3D space, called **q-space** [5], the coordinates of which are defined by a vector **q**. With a single diffusion sequence application one diffusion-weighted image is acquired, which depicts the diffusion-weighted signal intensity in a specific position **q** of the q-space, *i.e.* a specific gradient *strength* and *direction*, for every brain position, as shown in figure 2.13.
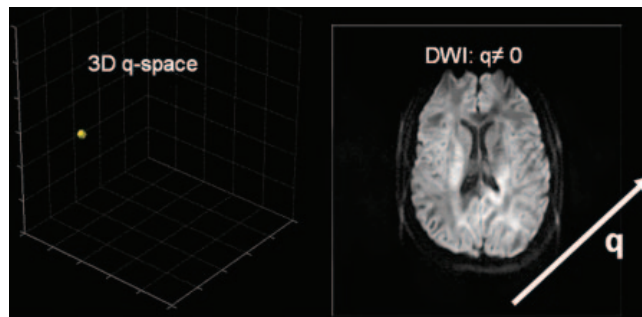
FIGURE 2.13: q-space. One diffusion-weighted image (RIGHT) is the result of sampling the signal at a single point **q** in the q-space (LEFT).

Repeated applications of the sequence with gradients that vary in strength and in direction (*i.e.* with variations of $\mathbf{q}$) allow data sampling throughout q-space. Like data from conventional MR imaging, in which a Fourier transform is applied to the data in k-space, the q-space data are subjected to a Fourier transform in every brain position. The result is a displacement distribution in each brain position, as seen in figure 2.10.

Bearing this in mind, it is possible to review the DTI method with the help of the q-space formalism. In fact, acquiring a DTI dataset means that at least six points in q-space with $\mathbf{q} \neq \mathbf{0}$ and one point with $\mathbf{q} = \mathbf{0}$ have to be sampled, as illustrated in figure 2.14. In general, constant size $\mathbf{q}$ vectors with b of approximately 1000 s/mm^2 are used, whose directions are arranged equally spaced in a sphere.
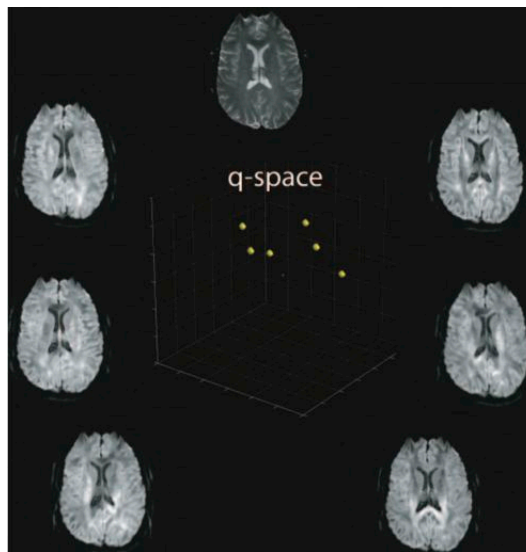
FIGURE 2.14: *Diffusion tensor imaging.* In q-space formalism, DTI samples q-space in at least six different directions, *i.e.* six different $\mathbf{q}$ vectors, with an additional reference image without diffusion-weighting, *i.e.* $\mathbf{q} = \mathbf{0}$. The *direction* but not the *strength* (*i.e.* constant b) of the diffusion gradient is changed for each sampling.

Diffusion Spectrum Imaging

Diffusion spectrum imaging, or DSI, was first introduced by Wedeen in 2000 [6]. DSI attempts to measure directly the *probability density function* of displacement of water molecules, introduced in section 2.3.1, making no assumptions about its shape or tissue micro-structure. This is quite remarkable: in fact, DTI makes a strong Gaussian assumption about the underlying diffusion process, which prevents fibre-crossing to be properly identified by the method.

Figure 2.15 compares the angular resolution of both DTI and DSI in a **region of crossing-fibres**. In the *pons* (yellow box), the *middle cerebellar peduncle* crosses the *corticospinal tract*. In the *centrum semiovale* (red box), the *corticospinal tract* crosses the *corpus callosum* and the *arcuate fasciculus*. The figure clearly depicts that DTI is not able of resolving crossing fibres, whereas DSI is.
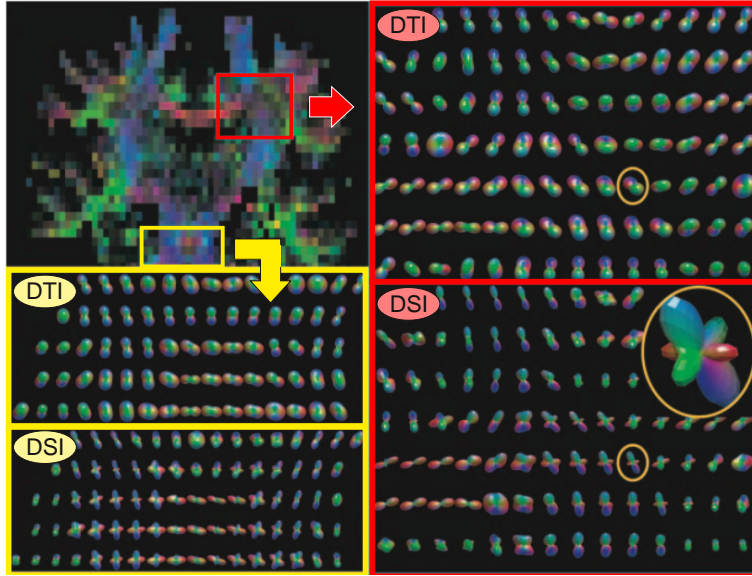
FIGURE 2.15: DTI vs DSI comparison in regions that contain fibre crossings. The **pons** (yellow box) and the **centrum semiovale** (red box) are highlighted.

According to [5], if a particle is moving due to diffusion process from position x_1 to position x_2 in the time-frame Δ between the applications of two gradient pulses $\mathbf{G_{diff}}$, the **signal attenuation** $A(q)$ is then given by:

$$A(q) = \frac{S(q)}{S(0)} = \int \rho(x_1) \int P(x_1, x_2, \Delta) e^{-iq(x_2 - x_1)} dx_1 dx_2 \qquad (2.20)$$

where $q = |\gamma \delta \mathbf{G_{diff}}|$ describes the applied diffusion gradient.

The function $\rho(x_1)$ gives the *spin density* at the time of application of the first pulse, and quantifies the likelihood of finding a spin at location x_1.

The function $P(x_1, x_2, \Delta)$ is called **diffusion propagator** and denotes the likelihood that a particle initially located at position x_1 will have ended up at x_2 after a time Δ.

Unfortunately, both of the previous functions are unlikely to be obtained in practice. By the way, in most applications, this function can be taken to be a constant throughout the water-filled region, where the value of the constant is determined by setting $\int \rho(x_1) = 1$. Moreover, by introducing a *net displacement* variable $x = x_2 - x_1$, it is possible to rewrite the equation 2.20 as follows:

$$A(q) = \int \overline{P}(x, \Delta) e^{-iqx} dx \qquad (2.21)$$

where $\overline{P}(x, \Delta)$ is the ensemble **average propagator** given by

$$\overline{P}(x, \Delta) = \int \rho(x_1) P(x_1, x_1 + x, \Delta) dx_1 \qquad (2.22)$$

This procedure was initially proposed by Stejskal [7] and makes it possible to *estimate the average propagator from signal attenuation data* by inverting the

Fourier transform in equation 2.21. Hence, if the average propagator is reconstructed at each voxel of the image, spatially localised displacement maps can be obtained as in figure 2.10.

The average propagator provides a detailed description of the diffusion and manages to resolve highly complex organisation of fibres. For simplicity, $\overline{P}(\mathbf{x}, \Delta)$ is normally reduced to an **orientation density function**, ODF, through a radial projection of $\overline{P}(\mathbf{x}, \Delta)$ according to:

$$ODF(\hat{\mathbf{r}}) = \frac{1}{Z} \int_0^\infty \overline{P}(\epsilon\hat{\mathbf{r}}, \Delta)d\epsilon \qquad (2.23)$$

where $\hat{\mathbf{r}}$ is a unit vector and Z is a normalisation constant. DSI usually computes $ODF(\hat{\mathbf{r}})$ for each of a finite set of directions $\hat{\mathbf{r}}$ by taking steps along the line in direction $\hat{\mathbf{r}}$, interpolating the discrete propagator $\overline{P}(\mathbf{x}, \Delta)$ to estimate its value at each step, and summing the values over all steps.
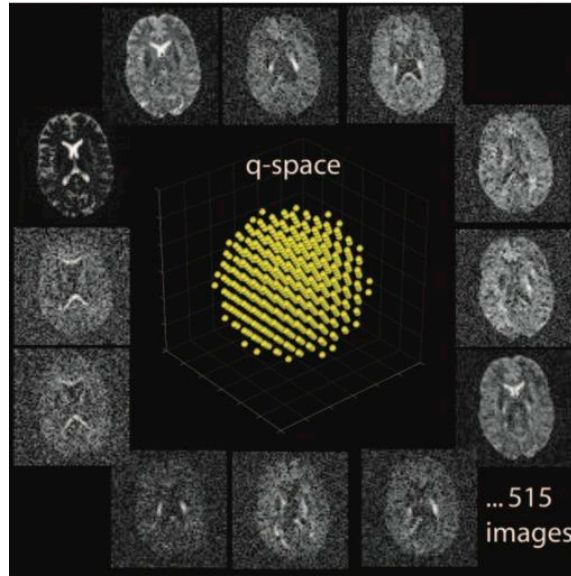
FIGURE 2.16: *Diffusion spectrum imaging.* Each image shows the diffusion-weighted image acquired at the corresponding point in q-space. Every sampling point in q-space corresponds to a specific *direction* and *strength* of the diffusion gradient, *i.e.* **q** vector. In established practice, up to 5 shells at different b values are sampled.

If established practice is followed, 515 diffusion-weighted images are acquired successively, each corresponding to a different **q** vector, that are placed on a cubic lattice within a sphere with a radius of up to five lattice units. The lattice units correspond to different b values, ranging from $b = 0$ (which corresponds to the centre point of the sphere) to, typically, $b = 8000$ s/mm^2 (which is a very high b value). So far, 515 images have been considered necessary to obtain data of good quality, although the acquisition of that number of images is very **time consuming**. Improvements in MR imaging hardware and techniques in recent years, especially multi-channels coils, have allowed to reduce the acquisition time for a whole brain acquisition from the standard 45-60 minutes to approximately 10-20 minutes, making DSI feasible in clinical settings.

Q-ball Imaging

With the purpose of reducing the acquisition time, methods for approximating the ODF have appeared in the last decade. Keeping only directional information means that a lot of unnecessary information is acquired during the measurements. The aim of this section is to provide the reader with some details of one of these approximating method. *Q-ball imaging*, or QBI, was first introduced by Tuch in 2004 [8]. QBI is a way of approximate the ODF avoiding to measure unnecessary information by sampling the diffusion signal directly on the sphere, as in figure 2.17 A.
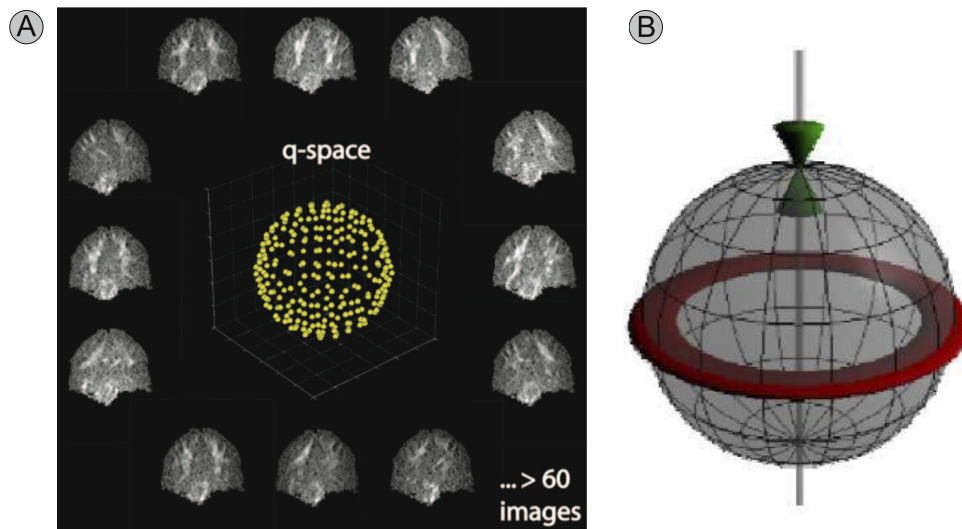
FIGURE 2.17: *Q-ball imaging.* (A) Points on only one shell with a constant b value are acquired in q-space. At least 60 images are necessary to reconstruct an orientation distribution function that is realistic. (B) The FRT assigns a value to a given point on the sphere (pointed by the green arrows), where the point can be seen as a **pole** and the value assigned to it is the integral over the corresponding **equator** (red disk).

Acquisition requirements are therefore more manageable than DSI, although the approximation of the ODF introduces some blurring, which may reduce angular resolution and precision of peak directions. In the absence of noise, the approximation of the ODF becomes more accurate as the fixed b value of the measurements increases. However, in practice, noise becomes more significant as b increases and a good balance needs to be found (see [9, 10] for details).

The approximation of the ODF made in QBI comes from a mathematical trasformation called **Funk-Radon transform**, or simply FRT. The FRT is a transformation of spherical functions that maps one function of the sphere to another, and can be seen as a generalisation of the *Radon transform*[2] to the sphere. Let's see how FRT works with an example. Suppose we want to know the diffusion intensity (*i.e.* the value of the ODF) in a direction that corresponds to the *North Pole* (green arrows in figure 2.17 B) and that the MR signal has been sampled over the whole sphere. If we add together the values of the signal

---

[2]The *Radon transform* is the basis of tomographic reconstructions used to recover images from CT scans.

intensity measured along the equator (red disk), the sum will be proportional to the diffusion intensity at the North Pole. ODF can be estimated by repeating this process for each point of the surface and redefining the equator accordingly.

2.3.5 Fibre tractography

Although a detailed discussion of fibre tractography is beyond the scope of this chapter, a brief explanation is necessary because tractography will be extensively used later in chapter 5.

Brain **fibre tractography** is a rendering method for improving the comprehension and thus the analysis of data from diffusion imaging of the brain. As shown in figure 2.18, it produces trajectories capturing coherent orientations of maximal diffusion that are likely to represent real axonal trajectories.
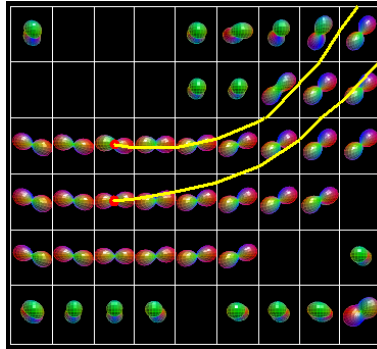
FIGURE 2.18: *Diffusion fibre tractography.* The simplest method exploits diffusion information inside each voxel to propagate trajectories from voxel to voxel capturing coherent orientations of maximal diffusion. *(image from [11])*

However, it's worthy to keep in mind that there are several orders of magnitude between the resolution of the MR acquisitions and the diameter of the axons. Therefore, tractography is only able to map large axonal bundles, and a single fibre produced by any algorithm has to be thought of as representative of a huge coherent set of real anatomical trajectories.

Lots of tractography algorithms have been proposed in the last decade, demonstrating the challenge issued by this topic and the great interest it has raised in the scientific community. A **tractography algorithm** is essentially defined by two main characteristics:

- the type of data it works on (*e.g.* DTI, DSI, QBI ...)

- the technique used to generate the trajectories (*e.g.* *line-propagation* or *energy-minimization* techniques)

They differ a lot in results accuracy, as well as in **time required** to generate the fibres. Generally, high complexity techniques are very accurate, at the price of requiring up to several days to produce a whole-brain tractography. For instance, Gibbs tracking algorithm [12] consists in a one-month process, which is by far too long to be considered for clinical applications, whilst a whole-brain

tractography can be achieved in a couple of minutes with the simpler FACT algorithm. FACT (Fiber Assignment by Continuous Tracking) is the first *deterministic line-propagation algorithm* introduced by Mori in 1999 [13, 14]. Despite the fact that deterministic line-propagation algorithms have been proved to suffer from many limitations, they are still largely used by the scientific community. Several studies have shown that despite these limitations, the FACT algorithm and the related line-propagation techniques allow to accurately reconstruct the major fibre bundles in the brain [15, 16]. In figure 2.19 an example of FACT-based tractography performed on DSI data of an healthy subject is shown.
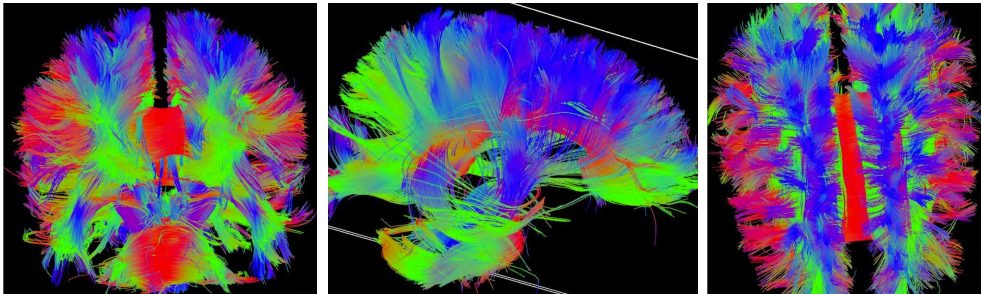
FIGURE 2.19: *Diffusion fibre tractography.* Representative fibre bundles reconstructed from DSI data of an healthy brain.

Diffusion MRI is able to give effective information about the micro architecture of white matter fibre bundles in the brain but, however, it suffers from **many limitations** which may dramatically affect the results of tractography. Except systematic biases arising normally in MRI, *e.g.* aliasing and partial volume effects, noise plays an important role in diffusion fibre tractography. In fact, it may lead to deviations of the principal diffusion direction from the real one of the underlying fibre tract. Furthermore, the limited spatial and angular resolution may lead to detection of imprecise principal directions or even produce unwanted local maxima directions of diffusion (*e.g.* by smoothing two separate diffusion peaks into one). Perhaps the **most important limitation** of tractography is that it is not fully validated. Attempts to clinically validate this technique have been made in the past [17]. Most of these efforts are based on comparisons of tractography results with known neuroanatomy atlases. Thus, diffusion tractography has to be used with caution.

Chapter 3

T_1 mapping and MEMRI

Manganese-enhanced MRI (MEMRI) is a relatively new method for investigation of neuronal pathways, enhancement of brain neuroarchitecture and functional MRI (fMRI) in laboratory animals [18, 19]. On the basis of Mn ions' capacity to enter excitable cells via voltage-gated calcium channels, MRI protocols have been devised that enable accumulation of Mn in active areas of the brain; this application has been termed *activation-induced MEMRI* (AIM-MRI) [18]. Accumulation of Mn in specific brain areas can easily be monitored by MRI thanks to its effect on longitudinal relaxation time. Compared to standard *Blood Oxygenation Level Dependent* (BOLD) fMRI techniques, AIM-MRI has several advantages:

1. higher sensitivity and signal-to-noise ratio, which allows fMRI at high spatial resolution and/or with mild sensory stimulation [19];

2. unlike BOLD, AIM-MRI depends not on blood hemodynamics but directly on neuronal activity;

3. Mn accumulation is visible in standard T_1-weighted images that are superior in terms of anatomical detail to T_2^*-weighted images used in BOLD acquisitions.

AIM-MRI experiments encompass three steps:

1. a certain amount of Mn ions needs to be delivered to the brain parenchyma;

2. the stimulus has to be applied;

3. differential accumulation of Mn in activated brain regions needs to be detected by T_1-weighted MRI.

The first step has been performed using different modalities: intravenous (i.v.) injection (with or without artificial opening of the *Blood-Brain Barrier*, BBB), intracerebral, intraperitoneal (i.p.), or subcutaneous injection. Most of the AIM-MRI experiments reported in the literature have been performed after i.v. infusion of $MnCl_2$ and artificial opening of the BBB [19, 20]. However, some recent

works have reported functional experiments performed after i.v. administration without BBB opening, or i.p. administration [21, 22]. Kuo et al. [21] reported detection of hypothalamic neuronal activity in-vivo after i.v. administration of $MnCl_2$ without compromise of the BBB. Yu et al. [22] demonstrated that AIM-MRI can detect sound-evoked activity in awake mice behaving normally after i.p. administration of $MnCl_2$. I.p. infusion appears particularly interesting because it can be used to study functional response in awake animals, if MRI is performed after the presumed activity has occurred and is preceded by an i.p. injection of Mn [23].

Differential accumulation of Mn in activated and silent brain areas is generally assessed using standard T_1-weighted images and quantified by the enhancement of the signal intensity (SI), which is calculated with reference to the SI before Mn administration or to the SI of brain regions that are known to be unaffected by the specific stimulus. However, SI enhancement can be unreliable when animals are removed from and reinserted into the magnet, as protocols on awake animals require, or when nonactivated areas are not known a priori. Absolute determination of Mn concentration in specific brain areas appears to be a good alternative. Mn concentration can be absolutely quantified by measuring the tissue longitudinal relaxation time through the well-known correlation between the enhancement in the relaxation rate, ΔR_1 and Mn concentration, c:

$$\Delta R_1 = r_1 \cdot c \tag{3.1}$$

r_1 being the longitudinal relaxation of Mn in the brain.

In this study we implemented an MRI protocol based on **fast T_1 mapping** and **coregistration to a rat brain atlas**, which made possible absolute quantification of Mn concentration in different brain regions. The aim of the study was to implement an MRI protocol based on quantitative Mn determination, to be used in AIM-MRI experiments.

3.1 Imaging sequence for fast T_1 measurement

Most T_1 quantification techniques are based on measuring the longitudinal magnetization at different time intervals TI after an inversion or saturation pulse[24]. Conventionally, one dataset with a given TI is acquired after each inversion pulse and the experiment is repeated after a sufficient long recovery period ($>5T_1$) with different TIs (single-point method). This acquisition scheme is highly sensitive and accurate, but it is also very time consuming, so it appears to be unfeasible in most pratical settings.

FLASH (Fast Low Angle SHot) is an fast MRI gradient-echo sequence for rapid acquisitions introduced by [25]. The technique is as simple as revolutionary in shortening MRI measuring times and its introduction allowed a drastic shortening of the measuring times without a substantial loss in image quality. Prepending an inversion pulse to a FLASH MRI sequence, it can be used as a fast and efficient way to measure T_1 values within reasonable time. As shown in figure 3.1, the magnitude of the longitudinal magnetization is acquired continuously during its recovery using a FLASH acquisition scheme, with low excitation flip angles α generally ranging from 5° to 10°.
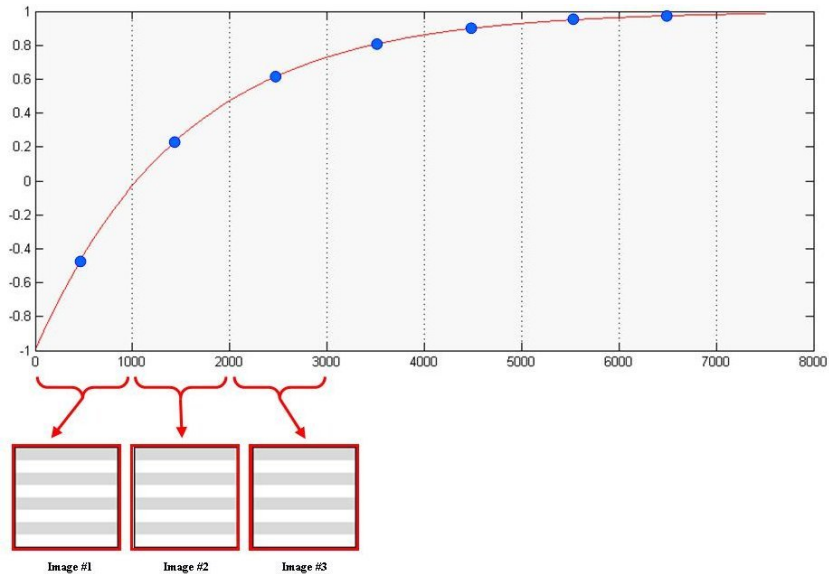
FIGURE 3.1: Acquisition scheme used in a IR-FLASH experiment. After an initial inversion pulse, a set of images are continuosly acquired during the recovery of the longitudinal magnetization (red line).

Despite its great speed-up improvement, FLASH MRI suffers from two intrinsic drawbacks:

- the influence of the excitation pulses on the recovery of longitudinal magnetization even for small flip angles;

- a trade-off between desired image resolution and sampling-rate during the recovery of the magnetization.

These two problems and the corresponding solutions, are discussed in the following two sections.

3.1.1 Effective longitudinal relaxation time $T_1^\star$

The problem of the influence of the small excitation pulses on the recovery of longitudinal magnetization during relaxation studies is well-know in the literature[26]. Briefly, since data is acquired continuosly and each low-angle pulse α is applyed in the steady-state, *i.e.* without waiting the full recovery of the signal, each pulse α alters the magnetization, ending with a measured *effective* $T_1^\star$ value which is shorter than the actual T_1.

Several approaches have been proposed in order to deal with this problem. Inversion recovery prepared TrueFISP[27], for example, is a fully-balanced version of the FLASH sequence which provide the possibility to measure T_1 and T_2 at the same time without the flip-angle influence problem. Moreover, thanks to its fully-balanced peculiarity, TrueFISP allows to exploit higher flip angles (optimal α is between 60° and 70°) and thus allowing to acquire images with higher SNR than IR-FLASH. Nevertheless, TrueFISP is very sensitive to field inhomogeneities and requires an accurate shimming of the magnetic field in the

27
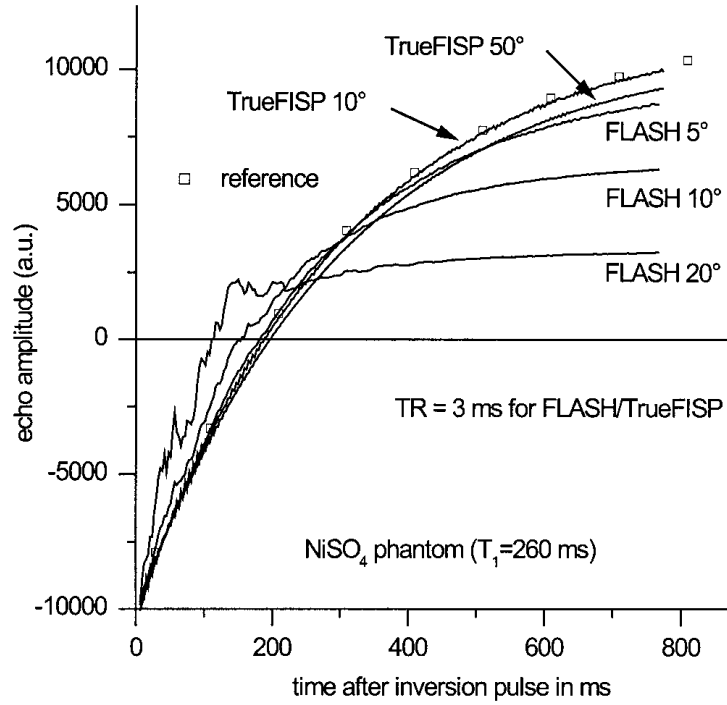
FIGURE 3.2: Recovery of longitudinal magnetization as measured by TrueFISP and FLASH for different flip angles. The squares indicate the reference amplitudes measured separately for different TIs. *(image from [27])*

region of interest. The MRI scanner in our laboratory had some problems with the *shimming* procedure at the time of the experiments. Thus, we could not use the TrueFISP sequence in our studies, so we decided to use IR-FLASH for T_1 measurements. However, this sequence was not implemented in the software bundle of our scanner, so we had to code it from scratch.

In order to calculate the *true* T_1 values from the measured *effective* $T_1^\star$, we exploit corrections suggested in [26]. Briefly, parametric T_1 maps were calculated pixel-by-pixel by least-squares fitting with an in-house developed software written in MATLAB (*MathWorks, MA, USA*). After a denoising step, in each pixel the theoretical expression of the SI:

$$SI(t) = A - B \cdot e^{-t/T_1^*} \tag{3.2}$$

was fitted to the experimental data. The *true* T_1 value was then calculated from the *effective* $T_1^\star$ by

$$T_1 = T_1^* \cdot \left(\frac{B}{A} - 1 \right) \tag{3.3}$$

Pixels in which T_1 values were longer than 3000 ms or shorter than 100 ms were excluded from the analysis.

3.1.2 Segmented acquisition scheme

The acquisition scheme of the FLASH sequence introduces a trade-off between spatial and temporal resolution for the acquired images. Since several images are acquired continuously during the evolution of the magnetization, as the image resolution increase, the allowed number of images inevitably decrease, since the time required to acquire each image becomes higher. For this reason, we modified the sequence in order to acquire the data in an interleaved fashion as shown in figure 3.3. An experiment is composed of several inversion-recovery cycles. During each cycle, after the inversion of the magnetization as usual, only a small portion of each image is acquired. At the end of the process, complete images are obtained by properly concatenating these portions acquired separately. This way, it is possible to split the acquisition in order to have the desired spatial and temporal resolutions. Of course, playing with the segmentation parameters, it is possible to have any combination between a normal IR-FLASH acquisition (*i.e.* one complete image during the recovery) and the TOMROP sequence[28] (*i.e.* only one line at each inversion).
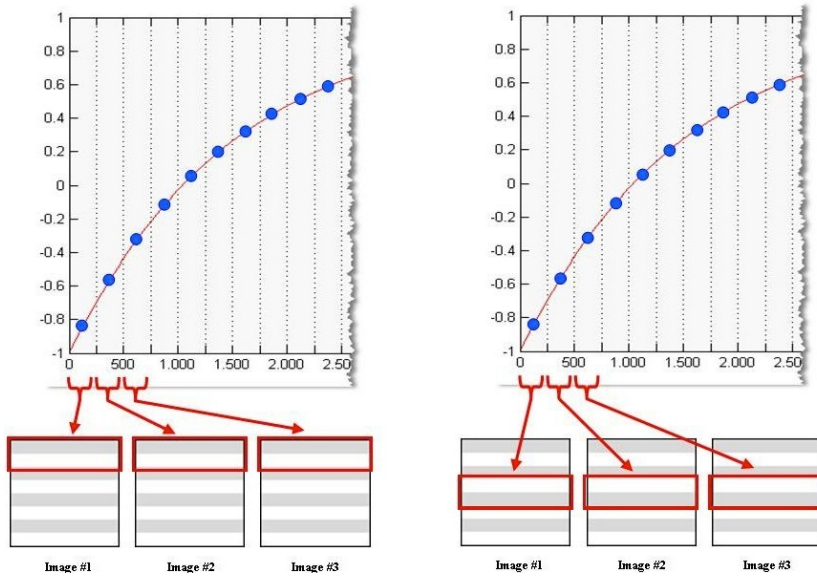
FIGURE 3.3: Segmented acquisition scheme. During the recovery following the first inversion (LEFT) only the lines $1, \ldots, k$ of each image are acquired. During the next inversion (RIGHT), the second part of each image is acquired, lines $k + 1, \ldots, 2k$, and so on upon completion of all parts of the images.

Let's see this process with an example. Suppose we want to acquire high resolution T_1 maps (128×128) of one sample whose estimated T_1 is about 1300 ms. This means we have to take samples of a T_1 recovery evolution that lasts around $5 \cdot T_1 = 6500$ ms. Since 128 lines have to be acquired for each image during this time, and pratical TR values are on the order of 10 ms, it turns out that only

$$(5 \cdot 1300 \text{ ms})/(128 * 10 \text{ ms}) \simeq 5.08 = 5$$

images can be acquired before complete recovery of the magnetisation.

On the contrary, if for example we split the acquisition in 8 segments (*i.e.* $128/8 = 16$ lines of each image acquired during every evolution), it turns out that we can acquire up to

$$(5 \cdot 1300 \text{ ms})/(16 * 10 \text{ ms}) \simeq 40.6 = 40$$

images during the same time interval, which is obviously more accurate to characterize the T_1 exponential recovery.

3.1.3 Calibration

The segmented IR-FLASH T_1 mapping sequence has been calibrated by correlating T_1 values obtained by imaging with values obtained by a *standard spectroscopic inversion recovery sequence*. Agarose gels (2%) containing different amounts of $MnCl_2$ (0.015, 0.03, 0.06, 0.125, 0.25, 0.5, and 1 mM) were prepared. T_1 values determined by imaging, T_1^{IM}, were linearly correlated with those obtained by spectroscopy, T_1^{SP}:

$$T_1^{IM} = 0.9775 \cdot T_1^{SP} + 0.0358$$

and the correlation amounted to $R^2 = 0.997$.

For spectroscopic T_1 measurements, single gel phantoms were inserted into a 3.5 cm inner diameter (i.d.) birdcage coil; an *inversion recovery* sequence with two squared pulses (42 and 84 μs) was used; the inversion times ranged between $1/100$ and five times the expected T_1 value. After the spectroscopic measurement, all the phantoms were inserted into a 7.2 cm i.d. birdcage coil for T_1 mapping using the IR-FLASH sequence. Images were acquired with the same parameters used in in-vivo experiments.

3.2 Coregistration to a rat brain atlas

Coregistration of T_1 maps to the *Paxinos and Watson brain atlas* [29] was performed as described by Schwarz et al. [30], with some modifications.

Briefly, acquired images were exported in the NIFTI-1 file-format, *i.e.* a standard file format expressly created for neuroimaging analysis, which makes it possible to specify in the file header the orientation of images in the reference frame of the scanner gradients. For each animal, T_2-weighted RARE images were used for coregistration to the T_2-weighted template of the rat brain developed by [30]. For the alignment procedure, we used FSL FLIRT software [31] and a *rigid 9 degrees of freedom* transformation. The *normalized correlation* was adopted as the cost function. The transformation matrix determined for the T_2-weighted scan was used to reorient all the other acquisitions of the same subject, exploiting the information about the orientation previously stored in the NIFTI-1 header.

The T_2-weighted *template* provided by Schwartz et al., built up by averaging 97 animals with age/sex matching, has already been coregistered to the Paxinos and Watson brain atlas. As a conseguence, after the coregistration of our scans to this *template*, we could extract ROIs by querying structures from this
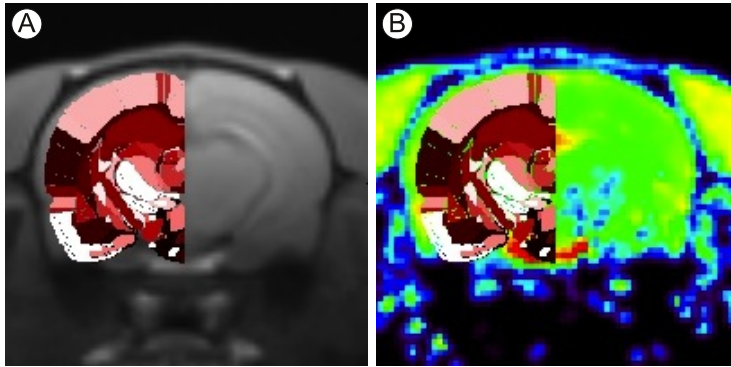
FIGURE 3.4: (**A**) Anatomical dataset of one representative animal co-registered to the Paxinos Brain Atlas (only left hemisphere is shown), and (**B**) the same transformation is used to align also the T_1 map to the atlas.

anatomical brain atlas (figure 3.4). Brain structures of interest were extracted from the atlas and superimposed over the T_1 maps of each subject. Average T_1 values in these regions, as well as in the whole brain, were calculated. Statistically significant differences were assessed by two-way analysis of variance (ANOVA) test for repeated measurements.

3.3   Materials and methods

Manganese solutions were prepared by dissolving 5.34 g of $MnCl_2$ (tetra hydrate; *Sigma-Aldrich, Italy*) in 100 ml of bicine buffer (*Sigma-Aldrich*) to obtain a final Mn concentration of 270 mM. These Mn solutions were administered i.p. to animals at a dose of 0.2 mmol/kg body weight. Twenty-eight male Sprague-Dawley rats (215 ± 23 g; *Harlan, Italy*) were used, subdivided into two groups:

- the **first group** of animals ($n = 8$) received three Mn injections at a dose of 0.2 mmol/kg over a period of 7 days (day 1, day 4, and day 7) and images were acquired on day 8;

- the **second group** of animals ($n = 10$) received two Mn injections at a dose of 0.2 mmol/kg over a 24h period (day 1 and day 2) and images were acquired on day 3. Eight animals were used for the measurement of in-vivo relaxivity.

Two additional animals were used for determination of the frequency dependence of relaxation rate enhancement. All procedures were carried out following italian regulations governing animal welfare and protection.

MRI experiments were carried out using a Biospec System (*Bruker, Germany*) equipped with a 4.7 T, 33 cm bore horizontal magnet (*Oxford, Ltd., UK*), a 20 G/cm gradient insert. A 72 mm birdcage volume coil and a quadrature rat brain shaped coil were used for transmission and signal detection, respectively. After induction of anesthesia in a preanesthesia box with a mixture of air and O_2 containing 5% of isoflurane (*Abbott spa, Italy*), rats were placed supine into

the magnet and maintained with a mixture of air and oxygen containing 2% to 2.5% of isoflurane.

T_1-weighted 3D gradient-recalled echo (GRE) images were acquired to localize the olfactory bulb/anterior cortex endpoint, which was later used as a reference to set transversal acquisitions. Transversal multislice fast spin-echo T_2-weighted images (RARE, Rapid Acquisition with Relaxation Enhancement, $TE_{eff} = 70$ ms) were acquired and used to coregister images to the rat brain atlas (see section 3.2).

Ex-vivo measurements of T_1 in the brain were performed at 37°C by using a Spinmaster (*Stelar, Pavia, Italy*) and an Apollo Spectrometer (*Tecmag, Houston, TX, USA*). The longitudinal spin-lattice relaxation time T_1 was measured through a standard *saturation recovery* sequence [24].

3.4 Mn relaxivity in-vitro and in-vivo

The **in-vitro relaxivity** of Mn in agarose gel was obtained by *least-squares linear fitting* of the relaxation rate values of the gels as a function of Mn concentration. The relaxivity of Mn, as measured by imaging, amounted to

$$r_1^{IM} = 3.74 \pm 0.60 \text{ mM}^{-1}\text{s}^{-1},$$

which was not different from the value obtained using spectroscopy

$$r_1^{SP} = 3.54 \pm 0.59 \text{ mM}^{-1}\text{s}^{-1}.$$

In-vivo relaxivity was measured using $N = 8$ animals. T_1 maps of the whole brain were acquired before and 24h after injection of 0.4 mmol/kg ($N = 2$), 0.3 mmol/kg ($N = 2$), or 0.2 mmol/kg ($N = 4$) of $MnCl_2$. The T_1 value was averaged over the whole brain. After the last acquisition the animals were sacrificed, the brains were removed, and Mn content was measured using *Atomic Absorption Spectroscopy*. The frequency dependence of the relaxation rate enhancement was measured on two additional animals: the first received 0.2 mmol/kg of Mn 24h prior to sacrifice and the other received the same amount of vehicle. T_1 measurement was performed on excised brains in the frequency range between 1 and 55 MHz. The average brain T_1 relaxation times of animals before and 24h after receiving $MnCl_2$, as well as the total Mn content, were determined.

Results are shown in figure 3.5 A, where Mn content is expressed in mM concentration, taking 1.041 mg/ml to be the average density of brain tissue [32]. Mn relaxivity in the brain amounted to

$$r_1 = 5.15 \pm 0.78 \text{ mM}^{-1}\text{s}^{-1},$$

which was higher than in gels, r_1^{IM} and r_1^{SP}, possibly due to binding with proteins or other cellular components, but was substantially lower than data reported in the literature [19, 33]. The low value of relaxivity observed in the present study is attributable to the high frequency (200 MHz), since relaxivity data reported in the literature are generally acquired at 20 MHz [19, 33].

Figure 3.5 B reports the frequency dependence of the relaxation rate enhancement in the rat brain 24h after administration of Mn (0.2 mmol/kg), measured ex-vivo in the range 1 to 55 MHz; the value at 200 MHz was obtained in-vivo by imaging. A clear peak is observed at about 10 MHz and then the relaxation rate enhancement rapidly decreases: at 200 MHz, the relaxation rate is about 10 times lower than its maximum value.
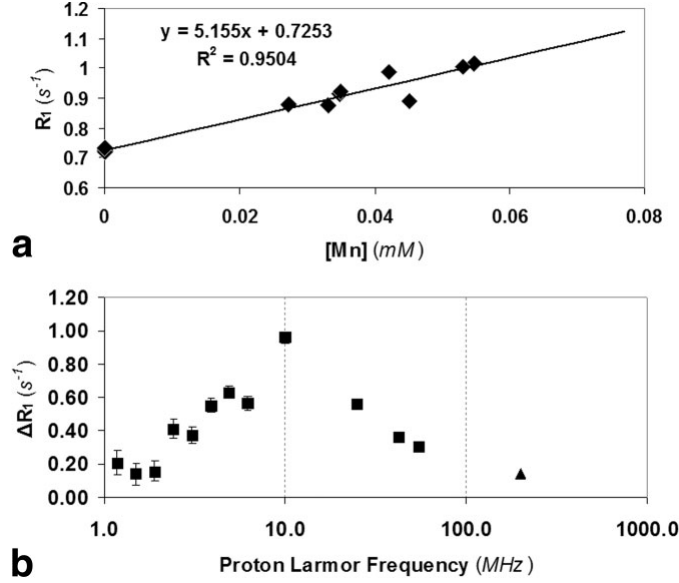
FIGURE 3.5: (A): Average longitudinal relaxation rate of brain tissue as a function of Mn concentration; the slope of the best fitting line represents in-vivo relaxivity of Mn ion (B) frequency dependence of the enhancement of brain relaxation rate, 24h after administration of 0.2 mmol/kg of $MnCl_2$. Data in the range 1 to 55 MHz were measured ex-vivo, while the value at 200 MHz was measured in-vivo by imaging.

3.5 Mn quantification in the brain

For T_1 measurements of the brain, the segmented IR-FLASH sequence described before was used, with the following parameters: $TR/TE = 10/3.6$ ms, $matrix\ size = 128 \times 128$, $FOV = 3.5 \times 3.5$ cm^2, $slice\ thickness = 1$ mm, $\alpha = 5°$, $inversion\ pulse = 5$ ms sech. The acquisition was divided into eight segments in the k-space in order to acquire at least three images before nulling of the signal ($acquisition\ time = 160$ ms per frame). Starting from the olfactory bulb/anterior cortex endpoint, 25 transversal slices were acquired.

Figure 3.6 shows representative 3D acquisitions of rat brain before and at different time points after i.p. administration of 0.2 mmol/kg of $MnCl_2$. The animal was removed and reinserted into the magnet twice (for the 12h and 24h acquisitions) but coregistration of images allowed perfect spatial reproducibility of the slices. It is worth noting that within the first hour after administration, $MnCl_2$ enhanced brain regions without BBB, such as the choroid plexus and pituitary gland, in line with previously reported findings [34]. At later time

points, MnCl$_2$ started to diffuse into brain parenchyma and 24h after administration, enhancement of the choroid plexus had almost disappeared, indicating diffusion from the ventricular space into brain tissue.
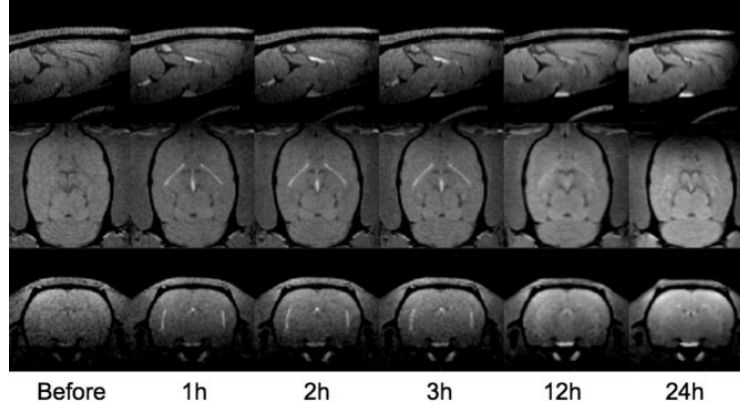
FIGURE 3.6: Transversal, coronal, and sagittal slices from 3D images acquired before and at different time points after administration of 0.2 mmol/kg of MnCl$_2$. The animal was removed and reinserted into the magnet for the 12h and 24h acquisition. Images were coregistered as described in the text.

Figure 3.7 A reports T_1 values measured in different brain regions using two administration protocols; data are reported as mean ± SD over the experimental group. It is clearly apparent that interanimal variability of postcontrast T_1 values is very low (the SD in all the brain regions considered was between 3% and 8% of the T_1 value, *i.e.* of the order of experimental error in T_1 determinations).

I.p. administration of a certain dosage of Mn delivers reproducible amounts of Mn to the brain. This finding is important for potential applications of this protocol in fMRI: interanimal reproducibility of Mn uptake should make it possible to detect differential regional uptake of Mn in stimulated and unstimulated animals. Postcontrast T_1 value averaged over the whole brain amounted to 968 ± 36 ms in the group receiving two Mn injections, which was not different from the average value in the group receiving three injections, 966 ± 43 ms. Figure 3.7 B shows the anatomical regions used for quantitative evaluations. The two administration protocols delivered similar amounts of Mn to different brain regions; postcontrast T_1 values were not statistically different (except in the hippocampus). Figure 3.7 B reports quantitative concentration data obtained from measured T_1 brain values and Mn relaxivity. Mn concentration in the brain areas considered ranged between 0.04 and 0.06 mM.

3.6 Discussion

There is rapidly increasing interest in MEMRI as a technique for functional and morphological imaging [35, 36]. With this work we have proposed an experimental algorithm based on fast T_1 mapping and coregistration of brain images to a rat brain atlas that allows absolute quantification of Mn concentration in selected brain areas, which in principle would allow experimental protocols in
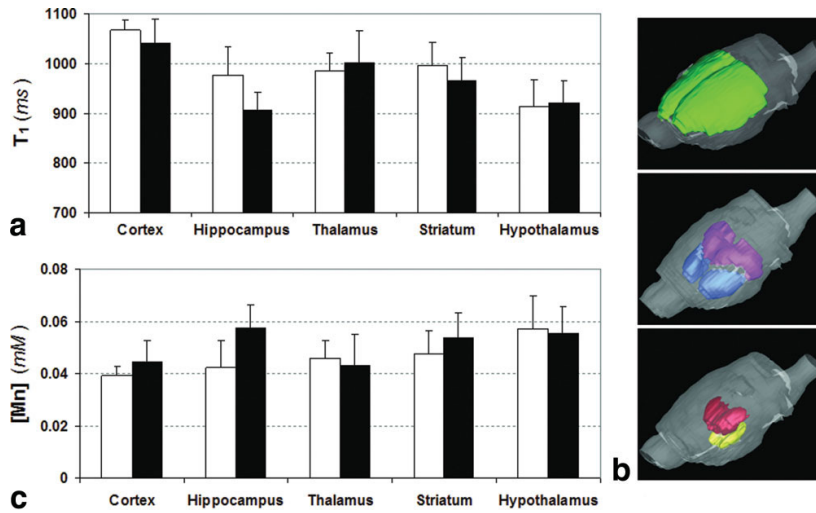
FIGURE 3.7: (**A**) Postcontrast T_1 values measured in different brain regions after two (white bars) or three (black bars) injections of MnCl$_2$. (**B**) Anatomical regions used for quantitative evaluations of relaxation times: the *cortex* in green, *thalamus* in red, *hypothalamus* in yellow, *striatum* in blue, *hippocampus* in pink. (**C**) Concentration of Mn in different brain areas.

which a stimulus is applied to awake animals behaving normally. Compared to standard BOLD fMRI, MEMRI has several advantages. The most important are that it does not measure signals of vascular origin, but events directly related to cellular depolarization, and that thanks to its high in-vivo longitudinal relaxivity, it allows detection of activation with high sensitivity. Relevant toxic effects have been reported for cumulative Mn dosages comparable to those used in the present investigation, although such effects were decreased by administration of fractionated dosages [37]. Mn toxicity is indeed a big disadvantage of MEMRI techniques that is likely to limit their transferability to human studies. Development of Mn-based contrast agents, with slow release of Mn, as well as of acquisition techniques sensitive to very small changes in water T_1 represent possible ways to develop MEMRI protocols suitable for human studies [38].

Here we measured in-vivo Mn relaxivity in rat brain, obtaining a value substantially lower than those reported in the literature [19, 33]. The frequency dependence of brain relaxation rate enhancement induced by the presence of Mn clarifies the origin of this low value: relaxation rate enhancement shows a maximum at low fields, around 10 MHz, and then a typical decreasing trend, as observed when Mn ions are bound to proteins [39, 40] or other cellular components. The abovementioned value for in-vivo relaxivity was used to estimate Mn concentration in different brain areas. With our experimental protocol, typical values for Mn concentrations were in the range 0.04 to 0.06 mM. It is worthwhile to mention that the above concentration values were calculated by using the mean relaxivity of Mn in brain, while the true Mn relaxivity could be dependent on its location and binding status. This approach may result with a not easily quantifiable degree of inaccuracy in calculated concentration values.

In this study we used a fast T_1 mapping technique to quantitatively de-

termine the content of Mn in different brain areas using two administration protocols: three injections over a 7-day period and two injections over a 24h period. In our experimental conditions we injected cumulative dosages of 0.6 and 0.4 mmol/kg of Mn, corresponding to about 120 and 80 mg/kg of MnCl$_2$-4H$_2$O. Surprisingly, our results show that the amount of Mn delivered to the whole brain or to different brain regions (except the hippocampus) did not change significantly with the two administration regimens.

Bock et al. [37] reported saturation in SI enhancement starting from a cumulative dose of 180 mg/kg, administered in six injections of 30 mg/kg each (separated by 48 hours). Apparently, we observed saturation in T_1 values at lower cumulative dosages. However, clearance of Mn from the brain during the 7-day time interval may have played a role. Two animals belonging to the three-injection group were repeatedly imaged from day 8 to day 30. The halftime of Mn concentration was about 8 days, indicating that a substantial fraction of the Mn injected on day 1 would have cleared by the imaging time (day 8).

In conclusion, we have established a protocol based on fast T_1 mapping and coregistration of images to a rat brain atlas that allows absolute quantification of Mn concentration in brain regions. This protocol in principle could be used in functional experiments performed in awake animals.

Chapter 4

DCE-MRI and tumour characterization

In order to grow in size, tumours require adequate oxygen and nutrient delivery, as well as removal of waste products. Angiogenesis, the process by which tumours create a circulatory blood supply, results in the development of abnormal vascular networks. Compounds that fight back tumour growth, either by blocking new vessel formation or destroying existing ones, offer potential targets for novel anticancer therapy. Since angiogenesis inhibitors reduce tumour growth or prevent metastases through primarily cytostatic modes of action, conventional end points based on reduction in tumour size may be inadequate for evaluating clinical response. Thus, alternative imaging biomarkers of angiogenesis are being sought, which could serve as early indicators of drug activity in clinical trials and may facilitate early pharmacodynamic assessments.

4.1 What is DCE-MRI?

DCE-MRI (*Dynamic contrast-enhanced magnetic resonance imaging*) is a non-invasive quantitative method of investigating microvascular structure and function by tracking the pharmacokinetics of injected contrast agents as they pass through the tumour vasculature (figure 4.2). The technique is sensitive to alterations in blood flow, vascular permeability (PS), extracellular extravascular ($\mathsf{v_e}$) and vascular ($\mathsf{v_p}$) volumes. Nowadays, DCE-MRI measurements have been incorporated as biomarkers of drug efficacy of angiogenesis inhibitors in clinical trials. The technique is promising, but its practical application is far from straightforward. The various analysis methods employed have considerable influence on the interpretation of derived parameters as potential biomarkers and/or surrogate end points.

In T_1-weighted DCE-MRI, an bolus of gadolinium contrast agent is injected i.v., enters tumour arterioles, passes through capillary beds and then drains via tumour veins. Gadolinium ions are paramagnetic and interact with nearby hydrogen nuclei to shorten T_1 relaxation times in local tissue water, thus causing increase in signal intensity within each corresponding voxel. The degree of signal

enhancement is dependent on physiological and physical factors. T_1-weighted DCE-MRI analysis generates parameters that represent one of, or combinations of these processes, and can be used to measure abnormalities in tumour vessel flow, blood volume, permeability etc. A comprehensive discussion about the technical aspects of DCE-MRI image acquisition and analysis is beyond the scope of this thesis. By the way, we want to give a brief description of the **two main data analysis methods** that can be applied to DCE-MRI data and which will be used in the rest of this chapter.

4.1.1 Signal intensity vs time curve

Features of the *signal intensity vs time curve* (*i.e.* overall shape, peak, time to peak, area under the curve) represent simple descriptions of contrast agent distribution (figure 4.1). However, these measures show considerable variation between acquisition method and individual examinations, making direct comparison between patients and trials difficult. Conversion of signal intensity into contrast agent concentration data allows more robust analysis of contrast agent kinetics. However the relationship between signal intensity and contrast agent concentration is not linear, making conversion of the signal intensity data far from straightforward [41].
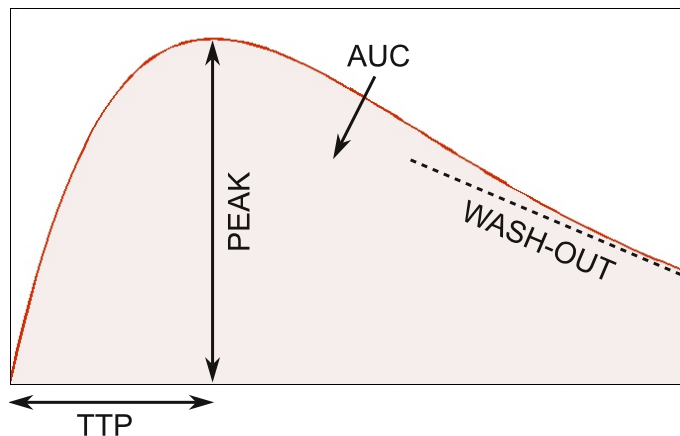
FIGURE 4.1: Representative features that could be extracted from signal intensity vs time curve: `PEAK`, `TTP` (*Time To Peak*), `AUC` (*Area Under the Curve*), `WASH-OUT`.

4.1.2 Pharmacokinetic models

Pharmacokinetic models can be applied to contrast agent concentration data to enable estimates of physiological properties such as flow and capillary endothelial permeability. Figure 4.2 shows a schematic compartmental modelling of the tumour micro-vasculature. Blood flows through the tumour enabling contrast media molecules (black dots in figure) to distribute in two compartments: the blood *plasma volume* v_p and the volume of the *extravascular extracellular space* v_e. Contrast agent leakage is governed by the concentration difference between

plasma and extracellular extravascular space, and by the permeability and surface area of the capillary endothelia PS. Clinically available MRI contrast agents do not leak into the *intracellular space* $\mathsf{v_i}$.
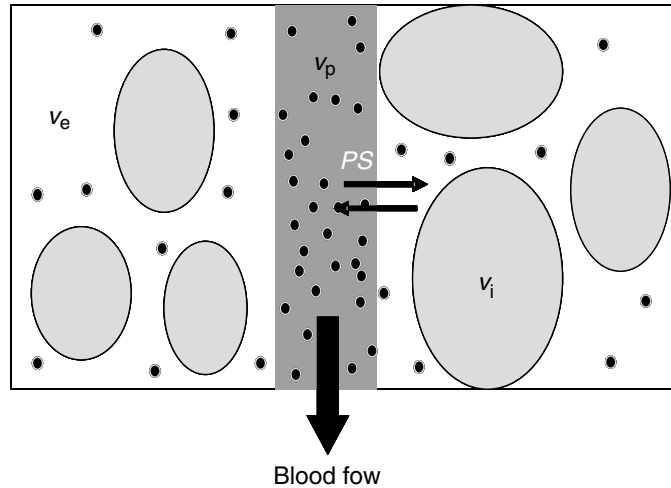
FIGURE 4.2: Compartmental modelling of tumour vasculature. *(image from [42])*

Modelled parameters are more physiologically meaningful than simple descriptors and are independent of acquisition protocol. Several models have been applied to clinical trial data to enable calculation of such parameters, and many of them are equivalent ([43, 44]). These models, however, require direct measurement of an AIF (*Arterial Input Function*) along with the tumour contrast agent concentration - time course curve. AIF is the concentration-time course of contrast agent in the artery supplying the vascular bed. These two functions are then used to quantify the passage of contrast agent through the tumour. Ideally, the AIF should be measured for each examination as it varies from subject to subject and between different measurements, reflecting injection timing, variation in cardiac output, vascular tone and other physiological factors.
Unfortunately, AIF measurement is technically demanding and, at best, produces an indirect measurement from a nearby large artery that may differ from the actual vessel supplying the tumour. For this reason, many groups use an idealized mathematical function instead, which makes no attempt to reflect the true blood supply to the tumour at each examination ([41]). Whichever technique is used, AIF measurement has a major impact on data analysis and clinical results - inaccuracy in the form or scale of the AIF affects the magnitude of all of the modelled parameters and their reproducibility.

It turns out, therefore, that the choice of the analysis technique for DCE-MRI data is not straightforward and reflects a compromise between parameters that are either relatively simple but poorly specific or physiologically congruent but less stable. In the remainder of this chapter we will show how we have used both approaches, *pharmacokinetic models* and *signal intensity vs time curve*, for tumoural tissues characterization in small animals cancer models.

4.2 Model based approach

Tumours possess an extraordinary plasticity that enables them to adapt to drastic microenvironmental changes; this leads to the undesirable development of therapy resistance, recurrence and metastatic process. In recent years, epithelial - stromal interaction in carcinomas is emerging as a crucial factor, which could be involved in their adaptive plasticity [45, 46]. The development of resistance to anti-angiogenic therapies is a clinically important paradigm of tumour plasticity. Clinical studies over the past two decades have demonstrated that treatment with tyrosine kinase pathway inhibitors results in a fleeting period of clinical benefit, after which the disease restart to progress. Four distinct adaptive mechanisms are currently thought to be at the basis of the transitory effects of anti-angiogenic drug [47, 48]:

1. activation of alternative pro-angiogenic signaling pathways,

2. recruitment of bone-marrow-derived endothelial and blood precursors,

3. increased perycite coverage of the tumour vasculature and

4. invasion and metastasis of surrounding or distant tissues.

In the present study we provided evidence of an additional mechanism, that is the development of an aberrant vascular supporting stroma at tumour periphery, following a prolonged anti-angiogenic treatment. For this purpose, we performed a time evolution study in an experimental colon carcinoma model by DCE-MRI to assess tumour vascular responses during 2 weeks of treatment with `SU6668`, a small molecule inhibitor of the angiogenic receptor tyrosine kinases, VEGFR-2 (Flk-1/KDR), PDGFR-β and FGFR1.

4.2.1 Experimental setup

HT-29 human colon carcinoma fragments were implanted s.c. in the flanks of 12 athymic *nu/nu* mice. Treated animals ($n = 7$) underwent daily administration of `SU6668` (200 mg/kg per day, p.o.) for 14 days; control animals ($n = 5$) received Cremophor-based vehicle. `SU6668` is a small molecule multi-tyrosine kinase inhibitor, developed in Sugen (*La Jolla, USA*) and then clinically discontinued because of a better response of an analogue molecule, *sunitinib*.

DCE-MRI was performed at days 0, 7 and 14 on both treated and untreated animals. *Gd-DTPA-albumin* was used as contrast agent according to the protocol described in [49]. Three-dimensional transversal spoiled-gradient echo images were acquired with the following parameters: $TR/TE = 50/3.5$ ms, *flip angle* $= 90°$, *matrix size* $= 128 \times 64 \times 32$, $FOV = 5 \times 2.5 \times 3$ cm^3. The acquisition time for a single scan was 104s. A dynamic scan of 24 images was acquired with 30s time intervals between each image, for a total acquisition time of 53 minutes. The 30s time interval allowed to avoid overheating of the gradient insert. Pre-contrast T_1 values were measured using an inversion recovery FLASH sequence, as shown in section 3.1. The contrast agent was injected in bolus during the time between the first and the second scan. The plasma kinetics of contrast medium was determined ex vivo.

4.2.2 Kps and fPV maps

From DCE-MRI data, *transendothelial permeability* (Kps) and *fractional plasma volume* (fPV) were calculated on a pixel-by-pixel basis as in [50]. To obtain mixed fPV/Kps images in red-green-blue format as in [51], fPV values were assigned to red intensities, and Kps values to green intensities, as in figure 4.3.
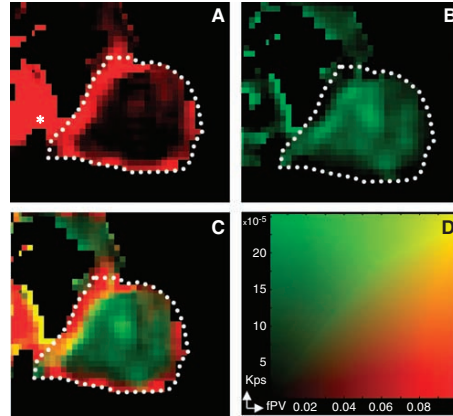
FIGURE 4.3: Mixed images. Representative fPV (**A**) and Kps (**B**) maps were mixed to produce the image (**C**) by the corresponding color scale (**D**). Yellow pixels in the mixed images indicate high fPV and high Kps. White dotted lines represent a manually drawn region encompassing the whole tumour. The central section of the tumour is shown, and the heart is visible left of the tumour (white ∗ in **A**).

The combined fPV/Kps maps clearly showed the architecture of tumour vasculature (figure 4.3 and 4.4). Tumour periphery was characterized by high fPV (red), whereas tumour core had low fPV but detectable Kps (green). The different pattern between the periphery and the core was observed in all untreated tumours and was preserved during their growth. During SU6668 treatment, marked changes in vasculature were clearly identifiable at the tumour periphery, with the appearance of a yellow layer (high fPV and Kps). These unexpected peripheral findings were observed in about 70% of the treated tumours.
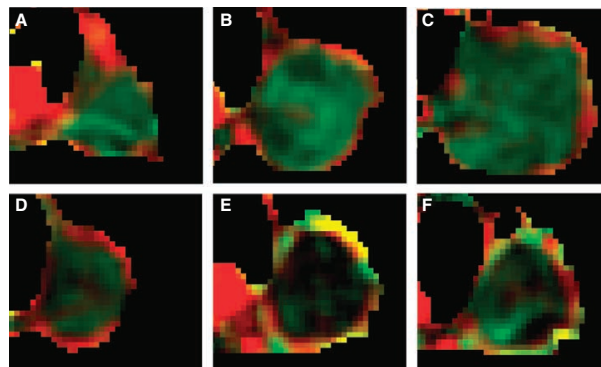
FIGURE 4.4: Mixed images: drug effect vs controls. Representative mixed images of untreated tumour growth at day 0 (**A**), day 7 (**B**) and day 14 (**C**) and of treatment progression at day 0 (**D**), day 7 (**E**) and day 14 (**F**).

4.2.3 Cluster analysis

To provide quantitative analysis taking into account of tumour heterogeneity, an automated operator-independent method, based on cluster analysis, was developed to identify sub-regions inside the tumour.

A volume of interest (VOI) was manually drawn to cover the whole tumour. Each VOI was then segmented into three different compartments by applying a k-means cluster algorithm (implemented in MATLAB, *MathWorks, MA, USA*) to the enhancement curves, $Enh(t)$, defined by:

$$Enh(t) = \frac{SI(t) - SI(0)}{SI(0)} \tag{4.1}$$

where $SI(t)$ and $SI(0)$ are the signal intensity values at time t and 0 respectively.

The L_1 metric (defined as $L_1 = \sum_i |x_i - y_i|$ for vectors x and y) was selected as the 'distance' function for all partitioning steps of the clustering algorithm. Although both from MRI and from histological examination two main tumour compartments were identified (an avascular core and a well-vascularized periphery), a third cluster was considered in the k-means clustering algorithm, to take into account pixels having intermediate vascularization and/or possible partial volume effects.

For each of the three identified clusters, average Kps, fPV and volume were calculated; for the whole VOI, then, mean and Kps and fPV were calculated. Non-parametric test (Wilcoxon) was then applied on the obtained values to statistically compare treated and untreated tumours.
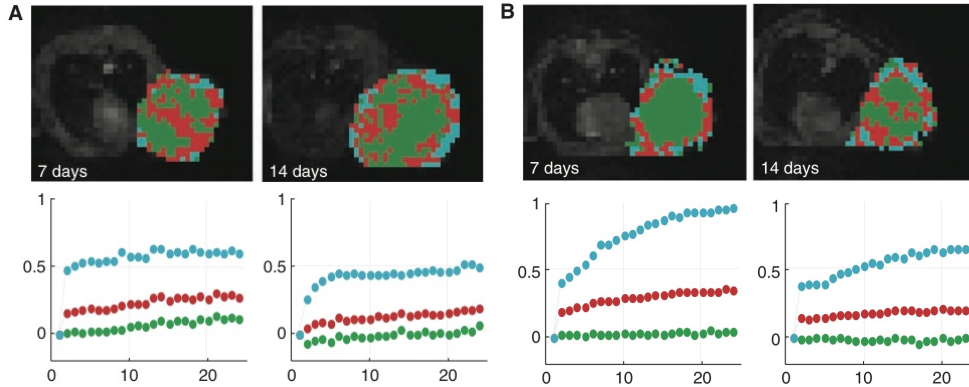
FIGURE 4.5: Cluster analysis automatically identifies sub-regions inside the tumour. Representative results obtained at 7 and 14 days in a control (**A**) and in a treated case (**B**) are shown. An avascular region, an intermediate and a well-vascularized area are identifiable. The time-course of the normalized signal enhancement for each region is shown with the same color below each picture. Number of scans is reported in abscissa. During untreated tumour growth, the identified sub-regions did not substantially change their enhancement pattern, whereas the most marked difference between untreated and treated tumours was observed in the peripheral sub-region.

Cluster analysis allowed identification of sub-regions inside the tumour (figure 4.5), with a peripheral well-enhanced sub-region clearly identified. Full data on all three identified subunits are reported in figure 4.6. The balance between
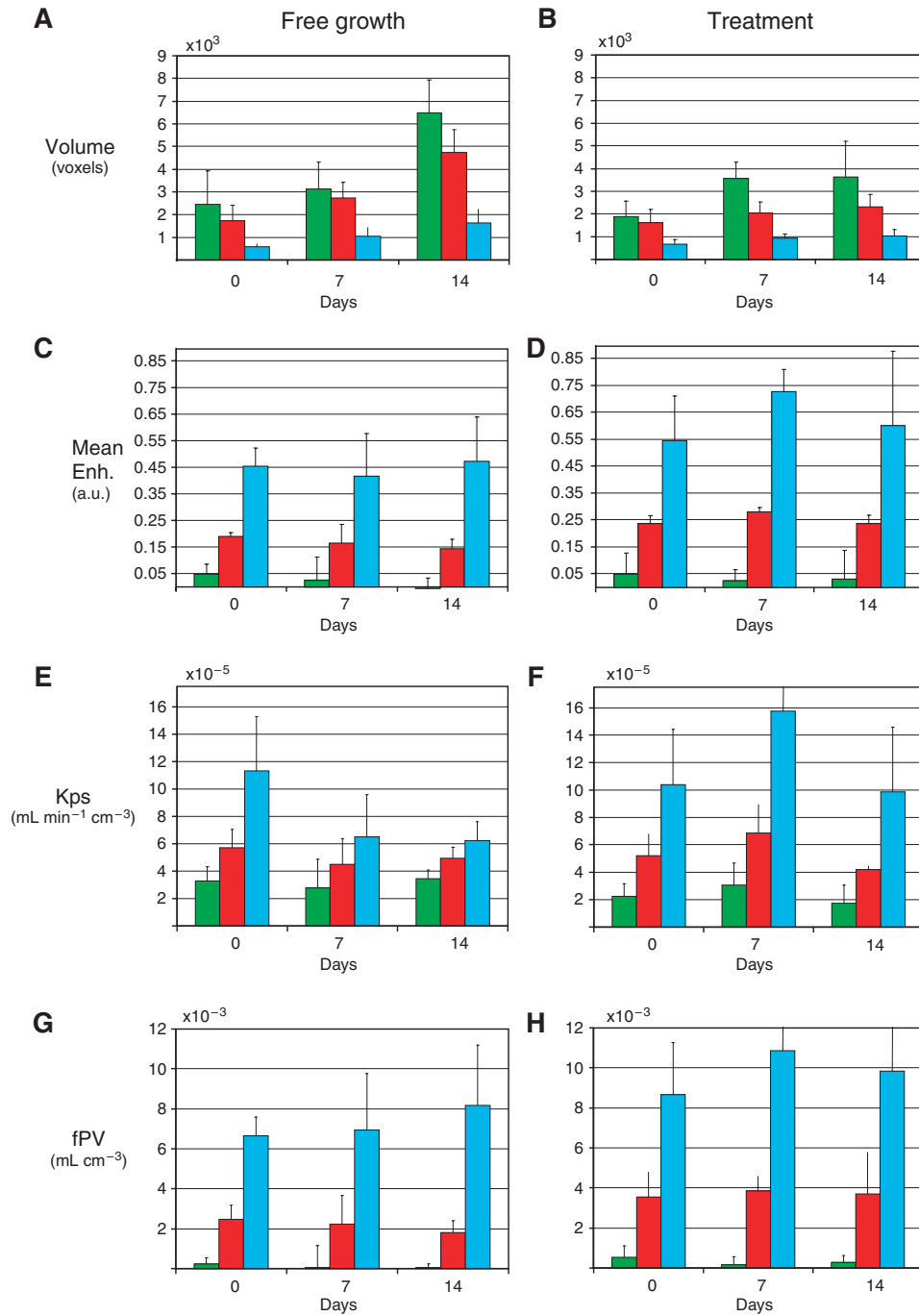
FIGURE 4.6: Summary of volumes and vascular parameters in the whole experiment. Volume (**A** and **B**), mean enhancement (**C** and **D**), Kps (**E** and **F**) and fPV (**G** and **H**) data on the three subunits identified by clustering algorithm, obtained by averaging data from different mice (controls, on the left; treated, on the right) at days 0, 7 and 14. Mean enhancement was taken as the mean value on the normalized enhancement curve. Error bars represent standard deviations across the group of tumours. The three identified sub-regions correspond to avascular, intermediate and well-vascularized areas.

the volumes of the three subunits resulted relatively stable during both untreated tumour growth (when there was an increase in total tumour volume) and anti-angiogenic administration (when there was a limited increase in total tumour volume).

The **most evident changes induced by** `SU6668` occurred in the peripheral sub-region characterized by higher vascular parameters with respect to the semi-necrotic and avascular zones. In this rim area, the progression in untreated tumour revealed a reduction in Kps; on the contrary in the treated tumours an increase was observed comparing day 7 with the pre-treatment point. In particular, Kps and fPV values were significantly higher ($P \leq 0.05$) after 7 days of therapy than the values obtained in the corresponding control tumours (table 4.1). The same table shows that mean values for the whole tumour VOI were not significantly different. At day 14 the higher Kps and fPV values in the treated tumours with respect to controls were not significant at a 0.05 level, because the MRI examination was performed only on three of the five mice that showed hyper-enhancement at day 7.

	DAY 0	DAY 7	DAY 14
Whole tumour			
Kps (10^{-5})			
Controls	5.3 ± 1.2	4.1 ± 1.6	4.4 ± 0.6
Treated	4.7 ± 1.1	5.9 ± 1.4	3.7 ± 0.3
fPV (10^{-3})			
Controls	1.9 ± 0.7	1.9 ± 1.1	1.2 ± 0.3
Treated	3.1 ± 1.2	2.7 ± 0.7	2.7 ± 1.4
Peripheral sub-region			
Kps (10^{-5})			
Controls	11.3 ± 3.5	$6.5 \pm 2.8^*$	6.2 ± 1.1
Treated	10.4 ± 4.0	$15.8 \pm 6.5^*$	9.9 ± 4.7
fPV (10^{-3})			
Controls	6.7 ± 0.8	$6.9 \pm 2.6^*$	8.2 ± 2.4
Treated	8.7 ± 2.6	$10.9 \pm 1.8^*$	9.9 ± 5.7
% of Volume			
Controls	13.4 ± 3.2	15.6 ± 5.2	12.4 ± 1.5
Treated	16.2 ± 2.1	14.1 ± 2.6	15.0 ± 3.7

TABLE 4.1: Mean Kps ($ml\,min^{-1}cm^{-3}$) and fPV ($ml\,cm^{-3}$) values obtained both on the whole tumour and the peripheral sub-region segmented by cluster analysis. Both values were calculated averaging on the whole tumour groups. The mean percentage volumes of the peripheral sub-region are also reported. The asterisk (*) indicates a significant difference (at a 0.05 level) in the comparison between treated and controls.

4.2.4 Histological examination

At day 14 mice were sacrificed and their tumours were excised for H&E histological examination. Two animals belonging to the treated group were killed at day 7. After fixation in zinc fixative for 6 hours, tumours were cut in half on a plane corresponding to that used for the MR images. After embedding in paraffin, 5 mm thick slices were cut and stained with H&E. Figure 4.7 shows the the comparison between control and treated tumours.
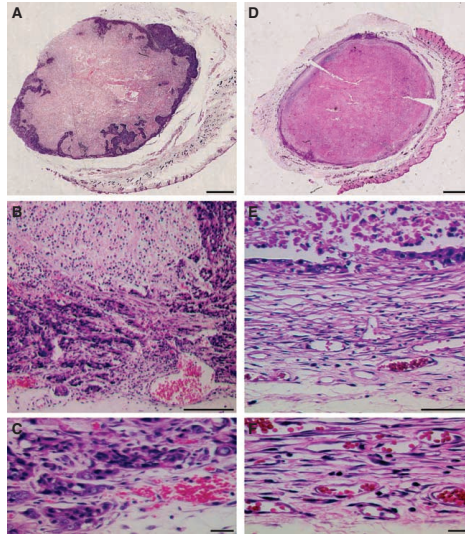
FIGURE 4.7: Histological sections from a control (**A**-**C**) and a treated (**D**-**F**) tumour at day 14. Scale bar, 1.5 mm (**A**-**B**), 125 mm (**C**), 60 mm (**D**), 10 mm (**E**-**F**).

In the control case (Figure 4.7 A-C), the whole section revealed the presence of a peripheral zone densely populated by viable neoplastic cells with nested intrusion into the contiguous semi-necrotic areas (**A**). Inside this matrix of viable cells, some vessels were detectable, which were particularly enlarged at the interface with tumour capsule, in a zone immediately contiguous (but external) to viable tumour tissue (**B**). At high magnification (**C**), the tumour cells appeared mixed with loose connective tissue.

After 7-14 days of treatment (Figure 4.7 D-F), a marked decrease in the thickness of viable peripheral layer was clearly detectable all around the external tumour border (**D**). The viable neoplastic cells contained in this rim appeared almost completely replaced by an increased amount of loose connective tissue (**E**), characterized by numerous small vessels (**F**), which presumably were responsible for the peripheral hyper-enhancement observed by DCE-MRI.

4.2.5 Discussion

DCE-MRI is now being used as an in vivo biomarker to evaluate the efficacy of angiogenesis inhibitors and other cancer treatments [52, 42]. The potential of DCE-MRI to evaluate intra-tumoural heterogeneity and investigate its relationship with response to therapy was recently emphasised [53]. One approach to investigate heterogeneity is based on histogram analysis of the distribution of pharmacokinetic parameters inside the tumour, which allows to demonstrate a rim-core difference in drug effect [54]. To overcome the limitation of the analysis of distribution based on a single or a small number of summary parameters, statistical techniques like principal component analysis (PCA) have been proposed [55]. Alternatively, cluster-analysis algorithms like k-means, closely related to PCA [56], can be used to obtain unsupervised and automatic VOI segmentation to account for tumour heterogeneity.

To develop an approach independent from any pharmacokinetics model, we have directly analysed the enhancement curves instead of using calculated Kps/fPV values. However, as the scanner gain could change between examinations, the signal intensity values were normalised to pre-contrast values. The successive evaluation of pharmacokinetic parameters on the obtained clusters, and in particular on the peripheral sub-region, proved to be more sensitive to the alteration induced by anti-angiogenic therapy than the analysis performed on the whole tumour VOI.

Our results raise the hypothesis that cancer-associated stroma is involved in the ability of carcinomas to adapt to anti-angiogenic therapy. Prolonged SU6668 administration promoted abnormal development of the stromal compartment at the periphery of the treated tumours: this rim appeared significantly more perfused with respect to control tumours, consistently with the well-recognised role of stroma in tumour vasculature organisation. Our findings may suggest a different and more comprehensive mechanism of resistance to anti-angiogenic therapies, which encompasses those already described by [48].

The observations at days 7 and 14 complement previous findings [49], where the standard effect of anti-angiogenic drugs, namely a decrease in peripheral Kps and fPV, was observed in treated tumours at early time points (24 hours to 3 days of treatment). Because anti-angiogenics cannot be expected to function as effective tumour therapy on their own, regimens combining them with chemo-irradiation are essential for local tumour treatment [57]. Anti-angiogenics induce pathophysiologic changes that can have a positive influence on tumour response to more conventional therapies [58]. The appearance of an efficient vasculature and the decrease in tumour cell density, observed at the tumour periphery after prolonged SU6668 administration, could increase the sensitivity of this part of the tumour to a subsequent chemo-irradiation. On the other hand, this unexpected stromal reaction might potentially lead to an overall increase in tumour aggressiveness.

4.3   Machine learning approach

Machine learning techniques are becoming important to support medical researchers in analyzing biomedical data. For instance, in the context of cancer imaging, methods for the automatic isolation of areas characterized by different tumoral tissues development are crucial for diagnosis and therapy assessment [59]. In this study, morphological and functional parameters obtained with DCE-MRI are analyzed by combining clustering[1] and classification techniques [60].

Our method extends a previous work from our group [61], and brings **two main advantages** to the current state of the DCE-MRI analysis. First, it allows a more stable and robust feature extraction step from DCE-MRI raw data. In fact, as highlighted in [62, 63, 64] the standard quantification of DCE-MRI data by means of pharmacokinetic models [65], suffers from large output

---

[1]We adopt the terms *segmentation* and *clustering* with the same meaning, *i.e.* a consistent partition of data into classes with high inter-class variance and low intra-class variance [60].

variability, which is a consequence of the large variety of models employed. Here, we propose to work directly on the raw signals by extracting few and significative features which robustly summarize the time-curve shape of each voxel. Second, we focus on the *automation* of the whole data-analysis process by exploiting the effectiveness of the machine learning techniques on the proposed applicative scenario. A three-step procedure is introduced:

Signal Features Extraction: in the first step we extract a few standard curve parameters [64, 66]. The aim is to define a compact representation of the signals curve shape of each voxel, which effectively summarize the expected behavior by medical researchers. Note that the same features are used for all the subjects and for all the kinds of tumor.

Automatic Voxels Segmentation: in the second step we cluster subjects' voxels, based on the features previously extracted, using the *Mean Shift* clustering algorithm (MS) [67]. We have chosen the MS method since it effectively performs a clustering of multi-dimensional data lying on regular grid (*i.e.* the image) by combining *spatial* and *feature* relations into the same framework [67]. Although the MS clustering approach allows a precise data segmentation, it requires a careful tuning of a free parameter, namely the *bandwidth*. For this reason, we propose to estimate such parameter on a small subset of the subjects, being supported by the medical researchers, that validate the segmentations.

Voxel Classification: in order to improve the automation of the proposed system, tissue segmentation inside a tumour can be treated as a classification problem on which a classifier is trained to distinguish among the regions previously extracted by the MS clustering procedure. A *Support Vector Machine* (SVM) is applied as classifier [68]. In particular, voxels of the same cluster are fed with the same label into the classifier. This way, the SVM becomes able to perform segmentations on new unseen subjects with the same kind of tumor.

In a previous paper from our group [61], we proposed the introduction of the MS clustering algorithm in order to analyze DCE-MRI data. In that case, we focused on standard tumor microvessels parameters, such as *transendothelial permeability* (Kps) and *fractional plasma volume* (fPV), obtained voxel-by-voxel from intensity time curves. By the way, even if the use of Kps and fPV parameters is employed in many recent researches [69], such standard parameters, based on the definition of a particular pharmacokinetic model, suffers from large output instability [62, 63, 64].

In this study, we were inspired by recent works focused on the use of **machine learning techniques** for DCE-MRI tumor analysis [64, 66, 70, 71]. In [64] the curve patterns of the DCE-MRI pixels are analyzed in the context of musculoskeletal tissue classification. Several features are extracted to represent the signals shape such as the maximum signal intensity, the largest positive signal difference between two consecutive scans, and so on. Then, the classification is carried out by introducing a thresholding approach. In [66] the authors proposed the use of the MS algorithm [67] for the clustering of breast DCE-MRI

lesions. In particular, pixels are clustered according to the area under the curve feature. Since the results are over-segmented, an iterative procedure is introduced to automatically selecting the clusters which better represent the tumor. In [70] a learning-by-example approach is introduced to detect suspicious lesions in DCE-MRI data. The tumoral pixels are selected in a supervised fashion and fed to a SVM which is trained to perform a binary classification between healthy and malicious pixels. The raw n-dimensional signal is used as multidimensional vector. In [71] a Neural Network was applied on dynamic contrast agent MRI sequences as a nonlinear operator in order to enhance differences in the signal courses of pixels of normal and injured tissues.

In this study we wanted to emphasize the use of machine learning techniques as a mean to produce stable and meaningful segmentation results in an automatic fashion. Furthermore, our approach should allow to speed up the analysis of DCE-MRI data, ensuring a higher throughput, that turns out to be useful in the case of massive analysis. For the purposes of the present work, the experimental setup is not significantly different from the one described in the previous section. In this case, *human mammary and pancreatic carcinoma* fragments were subcutaneously injected in the right flank of 42 female rats at the level of the median-lateral (see [69] for details).

4.3.1   Signal features extraction

From the raw DCE-MRI signal intensity vs time curves, few and stable features has been extracted. Figure 4.1 shows a scheme of the visual meaning of some representative features. For each voxel, the time-intensity curve has been normalized as shown in equation 4.1. Furthermore, data was filtered with a smoothing function in order to minimize errors due to outliers collected during the feature extraction step. More in details, the extracted features are:

- `TTP`. Time To Peak is the time interval between contrast agent injection and the time of maximum of signal intensity (SI).

- `AUC`. Area Under the Curve is the integral of the whole time-intensity curve.

- `AUC`$_{\texttt{TTP}}$. It is the integral of the time-intensity curve between contrast injection and the time of the maximum of signal intensity.

- `WR`. Washout Rate is the mean approximate derivatives of the last part of the time-intensity curve.

Note that proposed features depend only by the time-signal observed on a single voxel being independent by the respective contextual neighborhood.

In order to give the same weight to all of these features during the clustering procedure, a standardization procedure has been performed, *i.e.* the range of each feature was normalized to the *unit interval*.

4.3.2 Mean-shift clustering

The theoretical framework of MS arises from the *Parzen Windows* technique [60], which, in particular hypotheses of regularity of the input space (such as independency among dimensions, see [67]), estimates the density at point $\mathbf{x}$ as:

$$\hat{f}_{h,k}(\mathbf{x}) = \frac{c_{k,d}}{nh^d} \sum_{i=1}^{n} k\left(\left\|\left\|\frac{\mathbf{x} - \mathbf{x}_i}{h}\right\|\right\|^2\right) \tag{4.2}$$

where d indicates the dimensionality of the data processed, n is the number of points available, and $k(\cdot)$ is the kernel profile, that models how strongly the points are taken into account for the estimation, in dependence with their distance to $\mathbf{x}$, influenced by the h term. Finally, $c_{k,d}$ is a normalizing constant, depending on the dimensionality of the data and on the kernel profile.

MS extends this static expression differentiating equation 4.2 and obtaining the gradient of the density, which is:

$$\nabla\hat{f}_{h,k}(\mathbf{x}) = \frac{2c_{k,d}}{nh^d}\left[\sum_{i=1}^{n} g\left(\left\|\left\|\frac{\mathbf{x}_i - \mathbf{x}}{h}\right\|\right\|^2\right)\right]\left[\frac{\sum_{i=1}^{n}\mathbf{x}_i g\left(\left\|\left\|\frac{\mathbf{x}_i-\mathbf{x}}{h}\right\|\right\|^2\right)}{\sum_{i=1}^{n} g\left(\left\|\left\|\frac{\mathbf{x}_i-\mathbf{x}}{h}\right\|\right\|^2\right)} - \mathbf{x}\right] \tag{4.3}$$

where $g(x) = -\frac{\partial k(x)}{\partial x}$. In the above equation, the first term in square brackets is *proportional* to the normalized density gradient, and the second term is the so called *Mean Shift vector* $M_v(x)$, which is guaranteed to point towards the direction of maximum increase in the density (see [67] for details).

Therefore, the MS vector can define a path leading to a stationary point of estimated density. The modes of the density are such stationary points. More in details, starting from a point $\mathbf{x}$ in the feature space, the *Mean Shift procedure* consists in calculating the Mean Shift vector at $\mathbf{x}$, which will lead to location $\mathbf{y}^{(1)}$; this process is applied once again to $\mathbf{y}^{(1)}$, producing location $\mathbf{y}^{(2)}$ and so on, until a convergence criterion is met, and a convergence location $\mathbf{y}$ is reached. The Mean Shift procedure is guaranteed of being convergent [67].

In the MS-based clustering, or simply MS clustering, the first step is made by applying the MS procedure to all the points $\{\mathbf{x}_i\}$, producing the convergency points $\{\mathbf{y}_i\}$. A consistent number of close convergency locations, $\{\mathbf{y}_i\}_l$, indicates a mode μ_l. The clustering operation consists in marking the corresponding points $\{\mathbf{x}_i\}_l$ that produces the set $\{\mathbf{y}_i\}_l$ with the label l. This happens for all the convergency location $l = 1, 2, \ldots, L$.

In this clustering framework, the only interventions required by the user involve the choice of the **kernel profile** $k(\cdot)$ and the **bandwidth** value h. As usual, the *Epanechnikov kernel* is adopted as kernel profile [67]. This way, the meaning of the kernel bandwidth parameter is more intuitive. In fact, the kernel bandwidth parameter controls the level of detail by which the data space is analyzed; a large bandwidth means general analysis (few convergence locations), while a small bandwidth leads to a finer analysis (many convergence locations).

As previously stated, we used the MS algorithm on the $4-$dimensional space defined by the signals features extraction step. Since the **bandwidth selection is crucial** to find the correct segmentation (in the histological sense), we were

supported by the medical doctors during this fine-tuning procedure. It is worth noting that also subjects with the same tumor need different settings of the bandwidth. Therefore, we have applied the MS clustering only on a subset of subjects with the same kind of tumor. Once the medical doctors had validated MS clustering results, we used a classifier to distinguish the different kind of tumoral tissues, in order to be more suitable to generalize the results.

4.3.3 SVM classification

The involved classifier is the binary *Support Vector Machine* [68]. SVMs are suitable for our purposes since from DCE-MRI data we extracts a *n-dimensional feature array* for each voxel, as required by the SVM framework. Moreover, SVMs have already shown their efficacy on several domains, by performing a data-driven classification while being able to effectively generalize the results [60]. A SVM constructs a maximal margin hyperplane in a high dimensional feature space, by mapping the original features through a kernel function. We tried several kernel functions, but the most effective turned out to be the *Radial Basis Function* (RBF). Since the RBF kernel was used, **two parameters C and** γ needed to be estimated. Furthermore, in order to extend the SVM to a multi-class framework, the *one-against-all approach* is carried out [60].
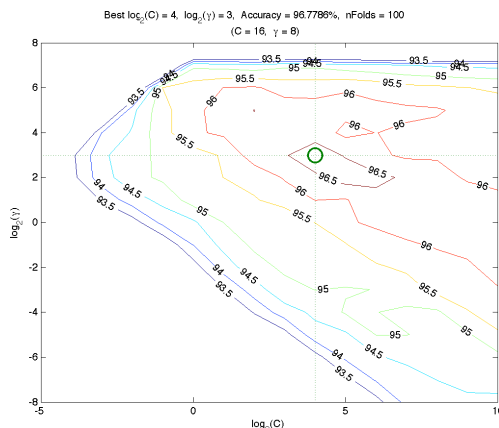
FIGURE 4.8: Representative results of the combination of *grid search* with *leave-one-out cross-validation* for the estimation of the two SVM parameters C and γ.

According to suggestions reported in [72], data has been properly normalized and parameters were estimated by combining *grid search* with *leave-one-out cross-validation*. Figure 4.8 shows this procedure. First, the **training set**, *i.e.* all the *n-dimensional feature arrays* extracted by the *Mean Shift* clustering step and validated by medical doctors, is separated into several folds. Each fold is sequentially considered as the **validation set**, *i.e.* the set of *n-dimensional feature arrays* on which testing the accuracy of the current (C, γ), and the rest are for training. The average of accuracy on predicting the validation sets is the **cross validation accuracy**.

As mentioned above, in our framework, such learning-by-example approach has been introduced in order to better generalize the results. In fact, SVMs

are able to automatically detect the most discriminative characteristics of the clusters detected by the previous MS segmentation step. Moreover, the training procedure is intuitive and the testing (*i.e.* the classification) is faster than the clustering itself.

4.3.4 Results and discussion

Signals features validation

As first experiment, we evaluated the effectiveness of the segmentation by comparing the clusters obtained from the signal features with those obtained from the standard tumor microvessels parameters Kps and fPV. In both cases we have carefully tuned the bandwidth, in order to find the best segmentation according with histological principles supported by medical doctors. Figure 4.9 shows the central slice of a tumour segmented with both the approaches. *Mean* of normalized signals intensity curves (equation 4.1) belonging to the same cluster, as well as the *median* and *standard deviation*, are plotted in the figure. Even if the two approaches seem to give apparently similar segmentations, an accurate inspection of statistical properties of these clusters reveals the better results achieved with our approach.
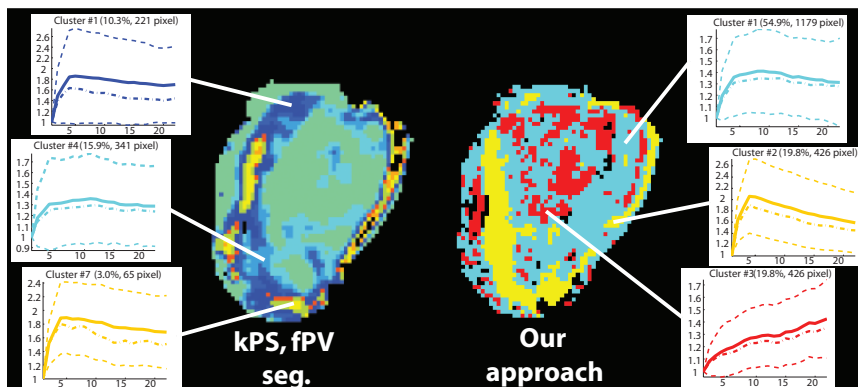
FIGURE 4.9: Segmentation comparison. The segmentation built on the Kps and fPV maps (LEFT) and our approach (RIGHT). We also reported the *mean* (solid line), *median* (dot-solid line), and *standard deviation* (dashed-line) of the signal.

In fact, it is possible to see that:

1. in general, good Kps and fPV based segmentations tend to be characterized by a large number of clusters. With a lower number of clusters, obtained by increasing the bandwidth of the MS algorithm, the segmentation decays in quality. We have shown the three most meaningful clusters, out of nine;

2. the intra-cluster variance is, in general, high;

3. the mean curves of the clusters do not appear so different among each other as expected.

It is worth noting that, **with our clustering approach**:

1. the clusters are less in number and meaningful;

2. the intra-class variance is lower;

3. the profile of the mean curves are coherent with the expected behavior of the signals (in a histological sense).

More in details, in the necrotic poorly vascularized region (*i.e.* cluster #3) the contrast agent concentration enhances linearly. On the contrary, the active area (*i.e.* cluster #2) evidences a more rapid enhancement. The peak of the curve is reached in the early side of the signal and then it decades slowly. Finally, DCE-MRI signals of the area associated to cluster #1 show a rapid enhancement with a slow decay, meaning that zones of tissue previously vascUlarized are approaching a necrotic state.

Pipeline validation

Following the proposed pipeline, we completed the experiment by segmenting an additional subject (beside the one used for signal feature validation) affected with the same kind of tumor of the previous cases. As mentioned before, different parameters have been used to estimate the best clustering results in both subjects.

Therefore, the SVM is trained to recognize the three extracted classes. Indeed, the tissue classification is performed to a third unseen subject with the same tumor. Figure 4.10 shows four slices of both the segmentation obtained from the training and the testing subjects respectively. Moreover, it is shown also the respective statistics collected on each cluster provided by the classifier. Note that the extracted regions and the respective statistics in both the cases in Figure 4.10 A and Figure 4.10 B exhibit the same behavior.

FIGURE 4.10: Experiment 1. Clustering results obtained with the *Mean Shift* algorithm (**A**) and the SVM classifier (**B**) respectively. The curves of the *mean*-signals are also visualized for all the clusters.

The classification has been **validated in two ways**. The first one is based on

the comparison with the analysis made by medical doctors, which confirmed the observations described above. As an additional validation, we have applied the MS clustering algorithm also to the third subject, once again by carefully tuning the parameters. By using the new obtained clustering results as the actual ground-truth, the SVM-based voxel classification reached the 89% of accuracy.

The same proposed pipeline has been tested on three different subjects with a **new kind of tumor**. Again, subjects #1 and #2 are used to train the SVM, while the subject #3 represents the test. Figure 4.11 shows the clustering results and the related statistics. Also in this case the behavior of the SVM classifier is coherent with the clustering results and in accordance with the medical researchers expectations.
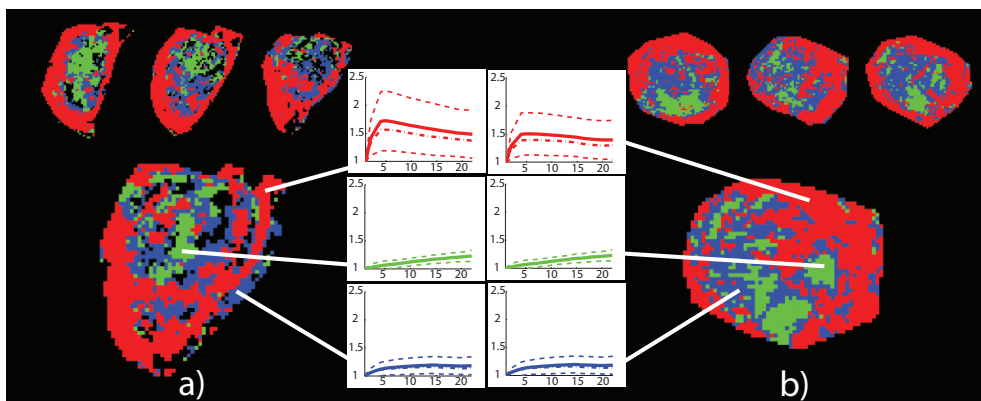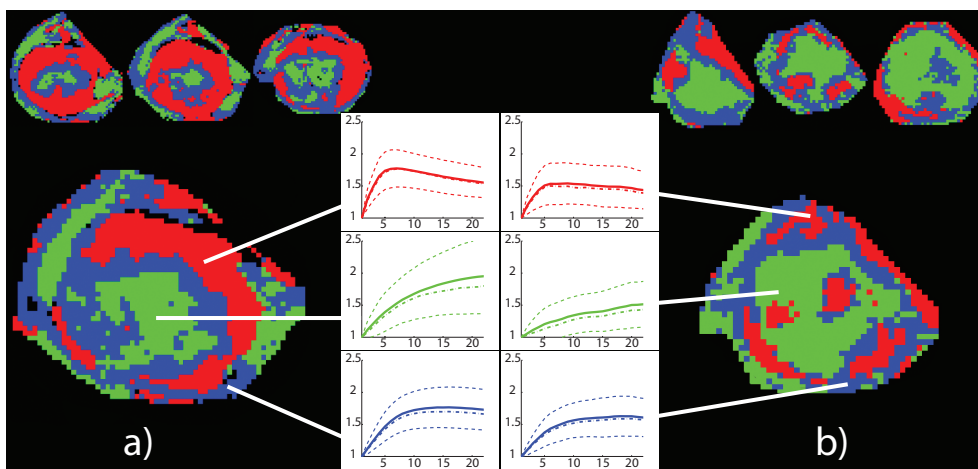

FIGURE 4.11: Experiment 2. Clustering results obtained with the *Mean Shift* algorithm (**A**) and the SVM classifier (**B**) respectively. The curves of the *mean*-signals are also visualized for all the clusters.

We have carried out further experiments on new subjects affected by different kind of tumors by observing mainly the same behavior: stable clusters of meaningful regions and well-defined behaviour, as expected by the medical doctors.

Discussion

With this work we introduced a new methodology aimed at improving the analysis and the characterization of tumour tissues. The multidimensional output obtained by non invasive tissue analysis, namely, the DCE-MRI technique has been considered. The signals from each voxel have been parameterized by few and compact features which robustly summarize signal profiles, as expected by the medical doctors. We have shown that the proposed signals features perform better than standard tumor microvessels parameters in segmenting the data. Moreover, we have shown the effectiveness of the proposed method based on the **combination of clustering and classification techniques**. Our results enlightened the evidence of a histologically meaningful partition of the tumour, which individuates tissue areas differently involved with the development of the tumor.

The proposed method achieves **two goals**:

- it permits an analysis of the tissue more precise and

- faster than the manual analysis classically performed.

These results assess that the proposed machine learning approach well behaves with medical segmentation and classification issues in the context of DCE-MRI data analysis.

4.4 Application to the efficacy evaluation of an anticancer therapy

In this study, tumour morphology and functional perfusion are obtained by DCE-MRI techniques. We propose a *learning-by-example approach* to classify tumoural regions characterized by heterogeneous vascular perfusion. Data are analyzed with the aim of investigating the volume changes in the identified regions for both untreated and treated tumours. As a result, a method for in-vivo evaluation of treatment efficacy becomes available to assess anticancer therapies.

The proposed analysis is based on three main phases: (i) features extraction from raw time-intensity curves, (ii) representative tumour areas identification, and (iii) overall voxel-by-voxel classification. In the first phase, few robust features that compactly represent the response of the tissue to the DCE-MRI analysis are computed. The second step provides a manual identification of tumour samples that are representative of the typical tumour aspects. Such samples are carefully and manually chosen by a medical researcher on a small portion of input data by observing the different behavior of the time-intensity signals within different kind of tumoural regions (*i.e.* necrotic or still alive zones). Finally, in the third step, an SVM is trained to classify voxels according to the regions (*i.e.* typologies of tumour tissue) defined by the previous phase. In this way, the SVM is able to automatically detect the most discriminative characteristics of the manually identified regions by extending such capability to classify unseen subjects.

In the present work we extend the basic framework proposed in section 4.3, to assess the treatment efficacy of anticancer therapies. The above described analysis is applied on two groups of animals (treated and control) at two time points (*i.e.* T_0 and T_1). At the end of the treatment period (time point T_1) the differences in tumour evolutions between the two groups were assessed by measuring volumetric differences on the various detected regions.

4.4.1 Materials and methods

Experimental design

Tumours were induced by subcutaneous injection of *human carcinoma cells* in nude mice ($n = 11$). Ten days after cells injection animals were randomly assigned to the treated ($n = 6$) and control group ($n = 5$). Animals belonging to

the treated and control group received an experimental drug and vehicle, respectively, for a period of 7 days. All animals were observed by MRI before (time T_0) and after the treatment (time T_1). A further group of mice ($n = 5$) bearing the same kind of tumour was used in the training step of the classification procedure.

Data acquisition

Animals were examined using DCE-MRI with *MS-325* (*Vasovist®, Schering Germany*) as contrast agent. Mice were anesthetized by inhalation of a mixture of air and O_2 containing $0.5 - 1\%$ isofluorane, and placed in a prone position inside a 3.5 cm i.d. transmitter-receiver birdcage coil. Images were acquired using a Biospec tomograph (*Bruker, Karlsruhe, Germany*) equipped with a 4.7 T, 33 cm bore horizontal magnet (*Oxford Ltd., Oxford, UK*).

DCE-MRI experiments were performed as previously described (see [49, 69, 73] for details). Briefly, after tumour localization, a dynamic series of three-dimensional transversal spoiled-gradient echo images were acquired with the following parameters: $TR/TE = 50/3.5$ ms, $flip\ angle = 90°$, $matrix\ size = 256 \times 128 \times 16$, $FOV = 6 \times 3 \times 2.4$ cm^3. The acquisition time for a single 3D image was 102s; dynamic scans of 25 images were acquired at 5s intervals (total acquisition time approximately 45 minutes). The contrast agent was injected in bolus during the time interval between the first and the second scan at 100 μmol/kg dosage.

Proposed method

At each time point, signal intensity values have been normalized to the pre-contrast value and filtered using a smoothing function to minimize fluctuations due to movement artifacts or noise. To account for tumour heterogeneity, seven classes have been fixed by combining a-priori knowledge of medical experts with the observation of signal shape behaviors (see A-G in figure 4.12):

- **Classes A and D**, are characterized by contrast agent wash-out(*i.e.* clear defined peak followed by a decrease). These regions correspond to highly vascularized and viable tumor tissue. Regions A and D differ by the value of maximum intensity.

- **Classes B and E**, reveal contrast agent accumulation (*i.e.* increasing trend). Presumably, this areas correspond to viable tissue with reduced vascularization, evidencing the transition of the tumor toward a necrotic state. Again, regions B and E differs by the value of maximum intensity.

- **Class C**, contains voxels with negligible enhancement, typically due to necrotic and not vascularized tissue.

- **Classes F and G**, have been introduced to account for intermediate patterns (*i.e.* initial increasing trend followed by a plateau phase).

By following the proposed pipeline, few and stable signal features are identified to model the different DCE-MRI curve classes. In particular the following
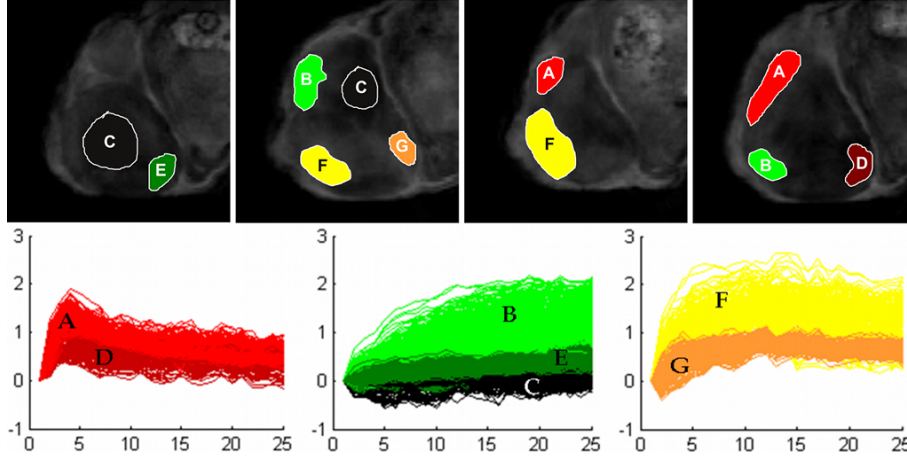
FIGURE 4.12: Sample regions used for SVM training. To account for tumour heterogeneity seven classes (A-G) were chosen by a-priori knowledge. Source data used to select the sample regions (TOP), and the relative DCE-MRI curves of the whole training set are reported (BOTTOM).

curve characteristics are chosen: *time-to-peak* (TTP), *peak value* (PEAK), *area under the curve* (AUC), *initial area under the curve* (AUC$_{TTP}$), and *wash-out rate* (WR) (see figure 4.1). Therefore, in order to apply a learning-by-example approach, several samples of each identified class need to be fed to the classifier. As mentioned above, such phase is carried out manually by medical experts. Figure 4.12 TOP shows some representative regions which are used to build the training set. In figure 4.12 BOTTOM the signals curve of the whole selected samples are reported. Signals are colored according to their respective class by evidencing the expected curve shape.

A binary SVM classifier is used to distinguish among the several tumoural tissue classes. The effect of the previously selected features in the classification has been assessed by comparing the results obtained using:

- only two (PEAK and TTP) features,

- all the five features (TTP, PEAK, AUC, AUC$_{TTP}$, WR), and

- directly the raw n-dimensional time-series.

The accuracy of the training phase of the SVM has been 89.1%, 95.4% and 99.8% using two features, five features and raw signals, respectively. This comparison allows a better identification of the most discriminative features by possible introducing a model selection phase.

Finally, in each tumour, the percentage volumes covered by each of the seven classes have been calculated to evaluate the time-dependent changes in control and treated tumours. The values obtained have been averaged over the experimental groups and statistically compared by paired t-test.

4.4.2 Results and discussion

The rate of tumour growth is strongly affected by the treatment; in fact average tumour volumes, as determined by MRI, increased as follow:

	T_0		T_1	
CONTROLS:	575 ± 104	mm^3	1821 ± 191	mm^3
TREATED:	553 ± 187	mm^3	788 ± 227	mm^3

TABLE 4.2: Tumour growth course in *control* and *treated* groups.

Table 4.3 summarizes the results of quantitative analysis in the treated and control groups. For each animal, the percentage volume attributed by the SVM classifier to each of the seven classes of signal intensity is reported before treatment (time point T_0) and after treatment (time point T_1).

		A		B		C		D		E		F		G	
		T_0	T_1	T_0	T_1	T_0	T_1	T_0	T_1	T_0	T_1	T_0	T_1	T_0	T_1
rawdata	Control	0,1	0,3	37,0	32,2	0,3	13,5	0,1	2,1	0,7	32,6	60,7	13,8	1,0	5,5
		1,7	1,4	12,4	22,5	4,6	5,7	2,6	2,5	8,2	9,2	68,3	56,2	2,3	2,5
		6,0	11,4	12,8	20,4	0,1	8,7	1,6	2,3	1,2	18,4	74,2	32,8	4,1	6,0
		4,3	7,1	4,9	16,0	0,6	4,6	1,7	2,7	3,8	23,7	83,6	38,3	1,2	7,6
		5,1	7,3	18,4	12,1	0,5	13,6	0,8	4,4	2,1	15,1	69,5	41,4	3,6	5,9
	Treated	14,3	9,0	13,1	12,6	1,5	4,4	4,9	3,0	4,5	9,4	58,7	55,6	3,1	6,0
		1,2	4,8	28,6	39,9	0,6	4,2	0,7	1,6	3,4	12,0	60,0	34,1	5,5	3,5
		3,4	13,5	34,1	19,1	0,3	1,5	3,3	3,9	3,4	10,6	50,0	43,4	5,5	8,0
		12,1	5,2	8,4	26,3	0,2	2,4	2,4	1,1	1,4	4,0	73,4	56,6	2,2	4,4
		5,0	11,2	21,0	23,2	4,8	4,3	6,7	8,0	8,6	13,6	47,0	30,0	6,8	9,7
		2,3	4,6	24,9	10,0	4,2	4,2	2,1	2,1	8,0	7,3	53,7	68,7	4,7	3,1
2 features	Control	0,1	0,4	32,4	23,7	3,3	22,7	0,1	1,2	3,3	27,1	58,8	18,3	2,0	6,7
		3,3	1,8	13,2	20,9	7,5	6,8	2,0	1,4	6,3	11,3	63,4	53,7	4,3	4,1
		4,4	10,0	7,3	17,2	0,4	8,6	1,2	2,0	2,9	18,3	77,6	36,4	6,2	7,4
		8,3	8,2	7,7	15,3	1,6	9,1	2,8	2,0	2,9	19,4	74,2	37,2	2,5	8,9
		5,1	7,6	14,9	9,2	1,9	16,7	1,1	4,0	5,6	15,5	64,8	40,9	6,6	6,2
	Treated	18,0	12,0	10,9	11,3	2,1	4,9	4,0	2,9	4,2	11,1	53,9	50,5	6,9	7,3
		1,3	4,5	19,5	29,8	2,7	5,5	0,5	1,0	10,0	11,7	58,0	40,9	8,1	6,6
		2,9	16,8	24,2	20,7	0,7	3,7	3,2	3,9	4,1	12,5	56,8	31,3	8,2	11,1
		15,7	4,3	11,7	16,7	0,3	8,6	2,9	1,0	2,1	9,0	63,6	55,0	3,6	5,4
		5,2	13,3	16,4	20,0	5,1	7,8	5,6	9,2	7,4	16,3	49,7	19,5	10,5	13,9
		2,5	7,1	21,1	10,4	4,4	8,8	1,6	2,7	8,2	9,8	56,3	56,4	5,9	4,8

TABLE 4.3: Percentage volume attributed by SVM classification algorithm to each of the seven classes A-G in each subject at time T_0 and at time T_1. Results relative to classification performed on rawdata and two features (TTP and PEAK) are shown.

Data reported in table 4.3, averaged over the different experimental groups, are shown in figure 4.13 A (relative to the **classification obtained by using raw data**). In the control group there is a significant ($p < 0.05$) increase of the percentage volume covered by the classes C and E (*i.e.* the less enhancing portions of the tumours). Concomitantly, a significant ($p < 0.01$) decrease of the class F is observed. An increase in the scarcely enhanced tissue (mainly necrotic tissue) is typically observed during fast tumour growth. The increase of this tissue is less pronounced in treated tumours as expected from their reduced rate of growth. The percentage volume attributed to A and D classes (wash-out regions that correspond to well vascularized tissue) is not significantly affected by treatment (or normal tumour growth) in agreement with the fact that the

biological target of the herein investigated therapeutic treatment is represented by tumour cells and not by vasculature.

Figure 4.13 B shows percentage volumes of A-G classes, averaged over the whole experimental group, relative to the **classification obtained by using 2 features**. Qualitatively, the alterations in percentage volumes of the different classes between time T_0 and T_1 are in agreement with those reported in figure 4.13 A, although there are some differences in their statistical significance. In selected animals standard histological and *CD31-immunohistochemical* examinations have been performed post-mortem according to [49]. These examinations qualitatively confirm the main findings of the present study.
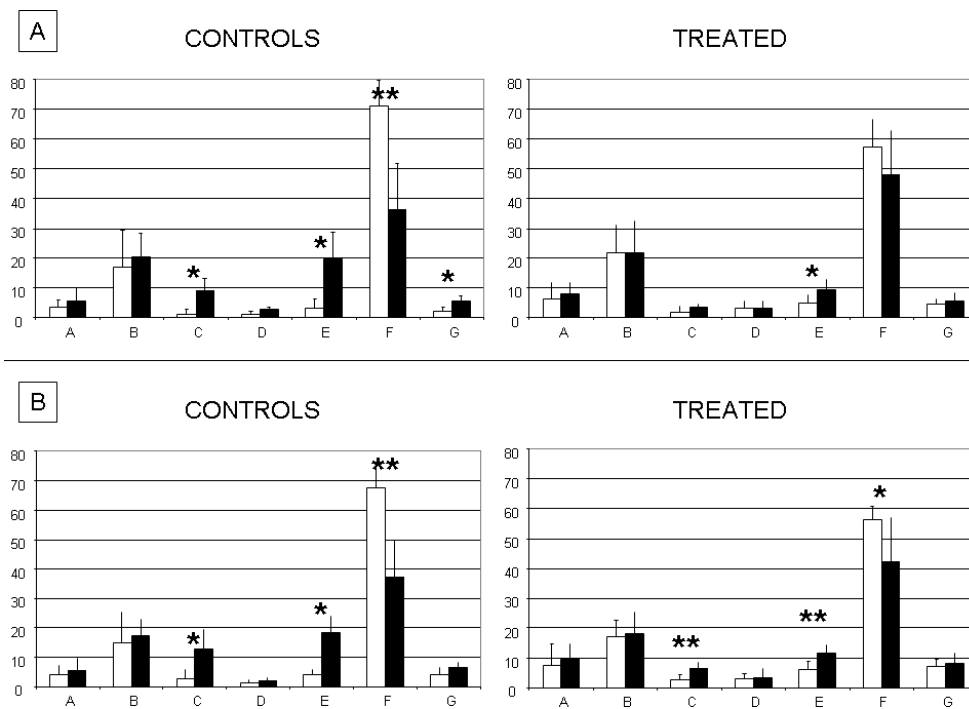

FIGURE 4.13: Percentage volume attributed by the SVM to each of the seven classes A-G averaged over the different experimental groups (control and treated). White bars represent values at time T_0, black bars at time T_1. Data reported in (**A**) are relative to the classification obtained by using **rawdata**; data reported in (**B**) are relative to the classification obtained by using **2 features** (PEAK and TTP). Asterisks indicate t-test significance at a 0.05 (*) and 0.01 (**) level comparing T_0 vs T_1.

The differences between percentage volumes of a given class obtained by using directly the rawdata or two features (table 4.3) are always less than 6% of the total volume. Comparable results (data not shown) are observed by using all the five defined features. These findings suggest that the identified features are able to summarize correctly the discriminative characteristic of the original DCE-MRI signals with respect to the addressed classification problem. The stability of the proposed method with respect to the number of classes has not been tested at this stage.

Figure 4.14 shows segmentation of tumour images obtained with SVM in two representative animals (vehicle and drug treated) before and after the treatment. The substantial increase in the necrotic portion of the control tumour, typical of fast growing tumours, can be visually appreciated.
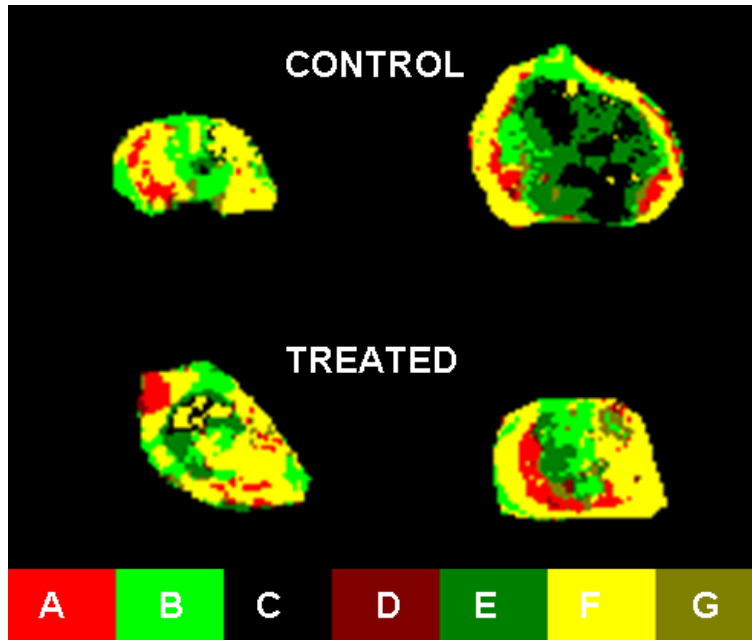

FIGURE 4.14: Representative segmentations in control and treated tumours at time T_0 (LEFT) and T_1 (RIGHT). The colorbar depicts the colors used to identify A-G classes.

In order to evaluate the effectiveness of the proposed method, we compared the regions obtained by SVM to those obtained by the standard k-means clustering algorithm (here $k = 7$). Figure 4.15 shows representative results obtained in two animals at time T_1 when using both algorithms on raw time-series. Each curve represents the time dependence of mean signal intensity over the extracted clusters. Both algorithms detect the necrotic areas (scarcely enhanced tissue), however whilst SVMs are able to distinguish between wash-out and accumulation regions, k-means depicts mainly regions with similar enhancement, as shown in figure 4.15 TOP. Moreover, even the meaning of the viable tumor areas is more clear when regions are detected with SVM.
In fact, by looking at figure 4.15 BOTTOM it is possible to infer the limited presence of highly vascular regions (*i.e.* classes A and D) being the viable area mainly characterized by the intermediate class B. Such considerations are not feasible from the k-means clustering. Nevertheless, with SVM-based segmentation the identification of corresponding regions among different subjects is obtained by construction, as opposed to k-means clustering for which such identification is not trivial (and in general for standard unsupervised segmentation methods). Therefore, the use of a data-driven algorithm appears unable to highlight regions with stable aspects and medical meaning, which can be only detected by a learning-by-example algorithm, such as SVM.
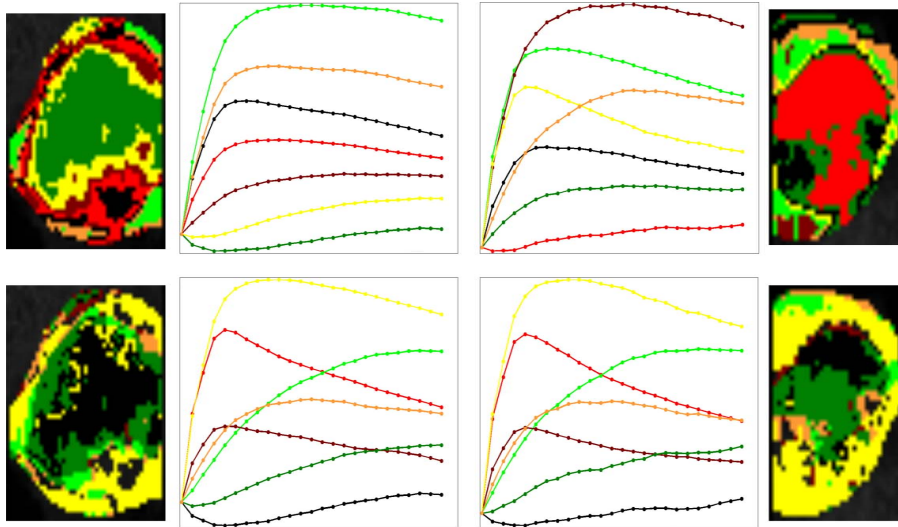
FIGURE 4.15: Clustering results obtained with *k*-means (TOP) and SVM (BOTTOM) in two representative animals at time T_1: one control (LEFT) and one treated (RIGHT). The time-dependence of mean signal intensity for the extracted clusters is reported. Tumoral regions detected with our approach satisfy better the expected properties and the mean signal shapes are coherent with the taxonomy previously described.

In this study we wanted to apply and test the effectiveness of the *proposed machine learning approach* in a real case quantitative evaluation of DCE-MRI cancer data. Summarizing, we have applied such technique in the analysis of DCE-MRI data to assess the effect of treatment with an experimental anti-cancer therapy. The SVM has been trained to detect biologically meaningful tumour regions of contrast agent accumulation and wash-out, as well as regions with negligible enhancement, attributable to necrotic tissue. The proposed approach enabled the computation of percentage tumour volumes of functional and biologically well-defined regions and allowed to follow their modifications during the treatment with an experimental drug. Our results have shown the significative increase of necrotic volume on untreated subjects as confirmed by histological validation, and suggest that this approach could be useful in the analysis of heterogeneous tumour tissues and of their response to therapies.

Chapter 5

Diffusion MRI and post-stroke plasticity

Stroke is a major public health issue with high incidence, mortality and morbidity. It represents the third cause of death in the over-65 years population and the first cause of disability. Most patients with brain attack do not achieve complete recovery and the significant disability among survivors has a great impact on health care and society [74]. There is increasing evidence that function recovery after cortical injury is largely attributable to adaptive plasticity in the remaining cortical and sub-cortical apparatus [75]. The term **brain plasticity** encompasses all possible mechanisms of neuronal reorganisation:

- recruitment of pathways that are functionally homologous to, but anatomically distinct from, the damaged ones;

- synaptogenesis;

- dendritic arborisation;

- reinforcement of existing but functionally silent synaptic connections, especially at the periphery of the damaged core [76].

The overall goal of this study is to use diffusion MRI to obtain a reproducible measure of *hyperacute*, *acute* and *chronic* motor network plasticity after stroke.
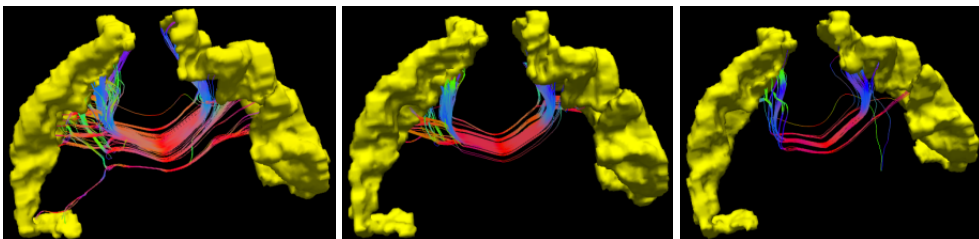

FIGURE 5.1: Patient affected by stroke. Hyperacute, acute and chronic white-matter connections are shown, respectively. In this particular case, it is possible to see a progressive loss of inter-hemispheric connectivity between *precentral* cortical regions.

5.1 Background and motivations

Structural plasticity after stroke have been extensively studied in the experimental research field. Animal studies suggest that intact cortical regions surrounding an infarct may contribute to return of function. Improved long-term synaptic potentiation in perilesional areas has been shown to occur a few weeks after stroke [77, 78]. Relevant changes have been described in rats within peri-infarct cortex including an increase in dendrites, synapses, and levels of proteins related to axonal outgrowth [79, 80, 81].

Focal cortical lesions provoke distant dendritic remodelling [78] and induce stem cells to differentiate into projection neurons that establish long-distance cortical connections [82]. Carmichael et al. [83] showed that after cortical stroke the peri-infarct cortex is structurally abnormal and develops new horizontal cortical connections by axonal sprouting. Complex interactions such as diaschisis (a change in functional output caused by a disturbance in an area of the brain distant to, but anatomically connected with, the primary site of injury) lead to loss of output from damaged brain areas to adjacent or distant brain areas. This demonstrates the capacity of the adult brain to establish new neuronal circuits in cortical injury models other than stroke. Pharmacological interventions that amplify these cellular events, such as amphetamine [79], basic fibroblast growth factor [80], or nerve growth factor [81], have been related to improved outcome. In association with these cellular events, studies of animals recovered from a cortical stroke show reorganisation of motor and sensory representational maps along the infarct rim [84, 85].

5.1.1 Recent human studies

To date, human brain plasticity has been studied using many different techniques including *positron emission tomography* (PET), *electro-encephalography* (EEG), *functional magnetic resonance imaging* (fMRI), *transcranial magnetic stimulation* (TMS) and *magneto-encephalography* (MEG).

Compared to **EEG**, the other techniques are more accurate tools to create a spatial map of the cortex and to examine changes in structural organisation of sensory and motor areas [86].

TMS and **MEG** allow the detection of sensorimotor areas reshaping, as a result of either neuronal reorganisation or recovery of the previously damaged neural network. But although both have a high temporal resolutions they also have limitations: TMS provides only bi-dimensional scalp maps, whereas MEG, even if giving three-dimensional mapping of generator sources, does so by means of inverse procedures that rely on the choice of a mathematical model of the head and the sources. In addition to it, these techniques do not test movement execution and sensorimotor integration as used in everyday life [87].

PET and **fMRI** are both based on the phenomenon that an increase in a brain region's neuronal activity (induced by movement or task execution) is accompanied by concomitant increase in local blood flow and blood oxygenation. The need for radio-labeled ligands in PET makes it both expensive and limits the number of times a given patient can be studied. The fMRI Blood Oxygen Level

Dependent (BOLD) signal arises from an increase in the oxy/deoxy-hemoglobin ratio in the draining veins of areas of increased neuronal activation. As a result, fMRI is the imaging method of choice in most studies of stroke recovery [88]. Numerous functional imaging studies in patients recovering from hemiparetic stroke have described different changes in cortical function both in the lesioned and in the contralateral hemisphere [89, 90, 91, 92, 93]. However, traditional fMRI studies inform essentially about reorganisation of cortical representational maps and can locate only the cortical regions subserving particular cognitive functions.

5.1.2 DSI as a tool for connectivity analysis

Better insights into stroke recovery might be facilitated by the development of techniques that non-invasively measure brain-network changes after stroke. As we have seen in section 2.3, **diffusion MRI** is a novel MRI technique which measures the molecular diffusion of water along neural pathways. In particular, its variant called *Diffusion Spectrum Imaging* (DSI) is able to resolve multiple fibre directions within a single voxel and therefore detect intravoxel white matter fibres crossing as well as white matter insertions into cortex.

The employment of this non-invasive imaging modality which is capable of measuring neural connectivity in-vivo can provide invaluable information on how human cerebral cortex communicates and integrates information across different processing areas and, more important for this project, *how these connections are modifying during post stroke brain reorganisation.*

Our hypothesis was that diffusion imaging could show motor network changes over time that correlate with the degree of the recovery. Understanding the modifications of connectivity between functional brain areas after stroke could allow a precise reconstruction of cerebral plasticity mechanisms and tissue architecture changes after a focal injury, opening new perspectives for future virtual reality rehabilitation programs and robot-assisted movement therapy.

5.2 Materials and methods

5.2.1 Patients enrollment

Twelve patients ($n = 12$) have been carefully selected to participate in this study at the Centre Hospitalier Universitaire Vaudois (CHUV) of Lausanne, Switzerland, and twelve normal subjects ($n = 12$) have been enrolled as controls. Control group (age: 57.5 ± 15) has been age and sex matched with patient group (age: 58.4 ± 17).

Inclusion criteria for patients was the diagnosis of stroke in the superficial *middle cerebral artery* (MCA) territory and *motor symptoms*. The diagnosis of **MCA stroke** was based on the contemporary presence of ischemic stroke lesion in hyperacute MRI scan and motor deficit signs. To evaluate symptoms and functional recovery throughout the rehabilitation, the NIHSS (*National Institute of Health Stroke Scale*) and the FIM (*Functional Independence Measure*) scores have been used.

5.2.2 Experimental design

Stroke patients underwent MRI examination three times:

- **time-point 1**, at hyperacute stage ($0 - 72$ hours after stroke onset);

- **time-point 2**, during rehabilitation (4 ± 1 weeks after stroke);

- **time-point 3**, at the end of rehabilitation (24 ± 2 weeks after stroke).

Concerning the control group, healthy subjects underwent MRI examination only twice within a 1 month interval ($\pm$ 1 week).
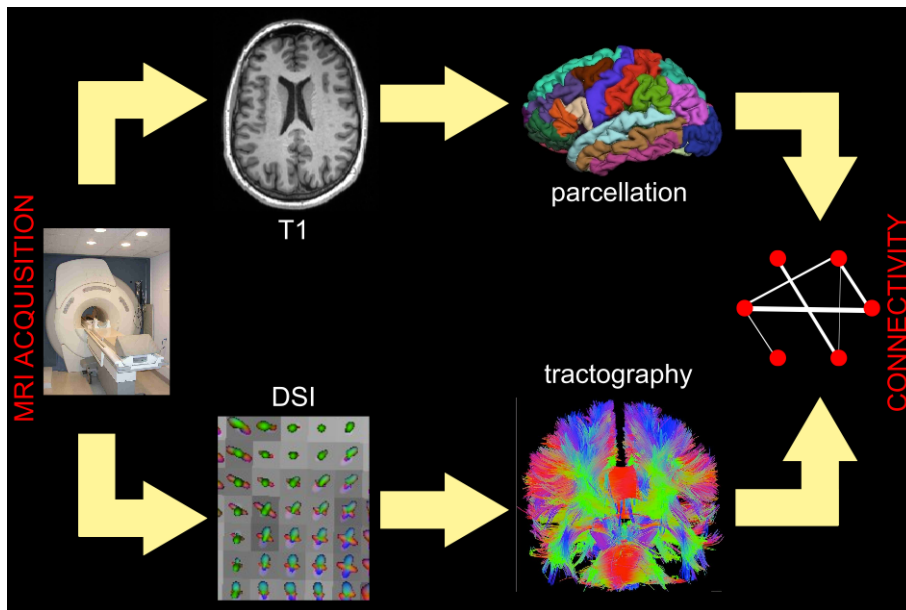

FIGURE 5.2: Workflow used for connectivity analysis.

The workflow for **brain connectivity analysis** is illustrated in figure 5.2 (see [94] for more details). The methodology consists of four main steps:

1. acquisition of diffusion MRI acquisition with DSI technique, as well as of an additional structural T_1 weighted image;

2. white matter fibre-tracking reconstruction;

3. white matter-grey matter interface partition into regions of interest;

4. analysis of the connections between each pair of extracted regions.

During each MRI session, one DSI dataset as well as T_1 and T_2 weighted images have been acquired. From the anatomical T_1 weighted images, a *parcellation*[1] consisting of 33 cortical regions of interest (ROIs) were mapped from each hemisphere using Freesurfer software [95]. DSI scan has been used to reconstruct the

---

[1]Here, we use the term parcellation as a synonym for segmentation of the surface between white-matter (WM) and grey-matter (GM)

main fibre bundles in the brain with a line-propagation tractography algorithm. By combining the output of these two steps we were able to create the **graph of brain connectivity**, *i.e.* for each pair of cortical ROIs we extracted all fibre bundles which connect them. In particular, we were interested in charachterizing the motor connectivity plasticity after stroke. For this resons, we consider intra and inter-hemispheric connections between the primary motor areas M1 and the secondary area SMA, from the parcellation obtained with Freesurfer. Every cortical ROI, *i.e.* M1 or SMA, extracted by Freesurfer has been associated to a node in the graph. We denoted by $ROI(v)$ the ROI that is associated with the node v. Two nodes v_1 and v_2 are connected with an edge $e = (v_1, v_2)$ if there exists at least one fibre extracted with the tractography algorithm with end-points in $ROI(v_1)$ and $ROI(v_2)$. Then, for each edge e it is possible to define several *weight* functions, $w_1(e), w_2(e), \ldots, w_n(e)$ which measure distinct properties of the connectivity between the two ROIs v_1 and v_2, *e.g.* density of connections, mean length, total number of fibres etc.

5.2.3   MRI protocol

All measurements were performed at 3 T (*Trio a Tim System, Siemens, Erlangen, Germany*) using a 32 channel head coil. Diffusion spectrum imaging scans were acquired with the following parameters: $TR/TE = 6600/138$ ms, $FOV = 212 \times 212$ mm, 34 *slices, voxel size* $= 2.2 \times 2.2 \times 3$ mm, 258 *diffusion directions*, $b = 8000$ s/mm^2. Orientation distribution functions (ODFs) were reconstructed using TrackVis software [96]. High-resolution T_1 weighted MPRAGE images were acquired with the following parameters: $TR/TE = 2400/3$ ms, $FOV = 256 \times 240$ mm, 160 *slices, voxel size* $= 1 \times 1 \times 1.2$ mm. In order to improve the accuracy of within time-point registrations (see next section), additional high-resolution T_2 weighted images were also acquired: $TR/TE = 3000/84$ ms, $FOV = 202 \times 230$ mm, 48 *slices, voxel size* $= 0.45 \times 0.45 \times 3$ mm.

5.3   Image registration

Since acquisitions with distinct MRI techniques (*e.g.* T_1, T_2, DSI) produce images which contain usually very different information about the underlying tissue structure and/or function, proper integration of useful data obtained from the separate images is often desired. The first step in this integration process is to bring the different images involved into spatial alignment, a procedure referred to as *registration*. For more details on medical image registration methods, please refer to these comprehensive surveys [97, 98, 99].

Concerning the present study, registration techniques have been exploited in two separate contexts:

- **Within time-points**. Since as we saw in section 5.2.2 the goal of the proposed workflow is to extract fibres (coming from the DSI acquisition) connecting each pair of cortical regions (coming from the T_1 scan), the two datasets must be spatially registered one another.

- **Between time-points**. We have used Freesurfer to extract cortical parcellations from T_1 scans, because of its ability to produce very accurate results in healthy subjects. In case of stroke patients, however, the lesions may negatively affect the results of parcellation and the tweaking of algorithm's parameters is very tricky. In order to reduce biases caused by lesions and to speed-up the parcellation process, we decided to apply Freesurfer only at the chronic stage and to exploit registration algorithms for applying the cortical segmentation to the other time-points.

5.3.1 Within time-points

At each stage of functional recovery from the stroke, *i.e.* the three time-points, structural and diffusion scans have to be registered for every patient. Even though T_1 and DSI images come from the same subject, if only a linear registration approach were used, the results would not be much accurate. As shown in figure 5.3 TOP, *spatial distortions* induced by the EPI[2] acquisition scheme are not taken into account with only linear transformations. This is particularly
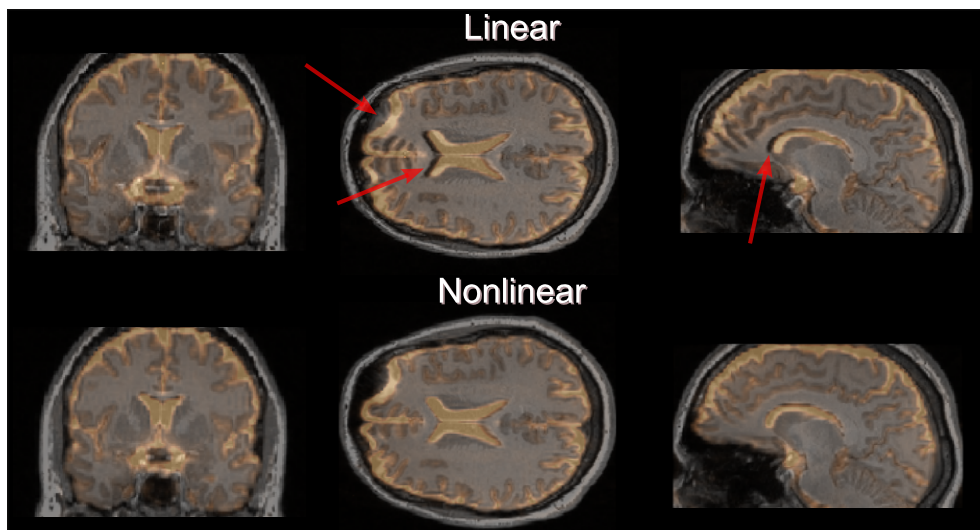

FIGURE 5.3: *Linear* vs *non-linear* registration comparison. T_1 (greyscale) has been overlaid onto DSI (gold image). Linear methods do not manage to correct the spatial distortions induced by EPI (pointed by red arrows), whereas non-linear algorithms do.

evident in the frontal lobe, where DSI (gold image) appears to be shrunk in the Anterior-Posterior direction in comparison to the T_1 (greyscale image). It's worth highlighting that this contraction may deeply influence the results of the present connectivity analysis, because even the *corpus callosum* appears to be significantly affected by these distortions, and thus all the fiber bundles passing through it could potentially be biased or even stopped. This kind of artifact has been found in almost every subject.

---

[2] *Echo planar imaging* (EPI) is a very fast imaging sequence often employed to speed-up diffusion acquisitions.

Geometric EPI distortions are a well known problem in the MRI community, and several approaches have been proposed for their correction. According to [100], these correction methods can be divided into two groups: (i) *field-map* based and (ii) *image registration* based. The most accurate is the field-map based approach, but it relies on the acquisition of an additional image, the so called *field-map*, which estimates the inhomogeneities of the magnetic field $\mathbf{B_0}$. Thanks to these inhomogeneity maps, it is possible to estimate the degree of distortion which was induced in EPI data, and therefore correct the images. Unfortunately, such additional data was not available for the present study, because these field-maps were not acquired at all. Thus, we had to correct EPI distortions with an image-registration approach.
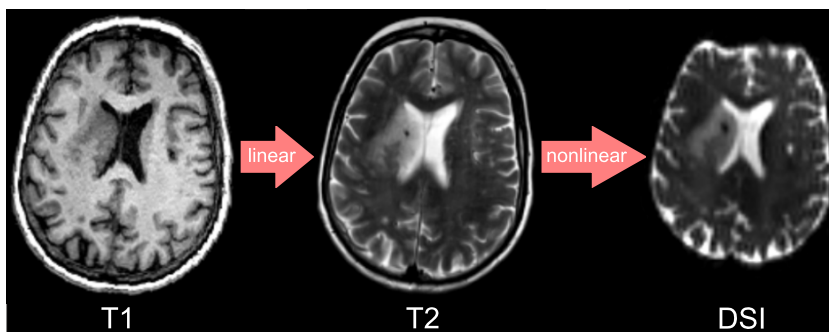

FIGURE 5.4: Two-steps registration workflow. First, the T_1 is linearly registered to the T_2, because even if they have different contrast there are no distortions among them. Then, since T_2 and DSI images have similar constrast, we use non-linear registration techniques in order to correct spatial distortions introduced by EPI (top of DSI scan).

Figure 5.4 illustrates the **two-steps worflow** used for $T_1 \rightarrow$ DSI non-linear registration. First, the T_1 image was linearly registered with the anatomically undistorted T_2 acquired separately. Since these two images have different contrast, but there are no distortions among them, a 6 degree-of-freedom linear trasformation is enough. At this aim, we used FSL FLIRT software [31] with *mutual information* metric. Then, the undistorted T_2 scan was registered to the first image with $b = 0$ in the DSI dataset using a deformable registration algorithm, with *sum of squared differences* metric and *cubic B-spline* modeled deformation field. The non-linear registration was carried out with FSL FNIRT software [101]. Since FNIRT only incorporates the sum of squared differences metric, it was not possible to directly register the T_1 to the DSI, because they have different contrast.

This issue was solved by using the additional T_2 image as an intermediary step. However, even if T_2 and DSI images have similar constrast, they differ in some anatomical details particularly important in the context of non-linear registration. As clearly visible in figure 5.4, the skin outside the skull appears hyper-intense in T_2 images, whereas it is almost invisible in the DSI scan. Hence, if we used the registration without any constraints, the algorithm would try to align the surface of the brain in DSI scans with the skin visible in T_2 images. To solve this issue, we had to inform the algorithm about the brain boundaries of each involved scan, *i.e.* T_2 and DSI, by means of *binary mask* images. This

allowed to preserve the global brain shape, but at the same time being able to perform non-linear local deformations in order to account for EPI distortions. Figure 5.3 BOTTOM shows non-linear registration results for one representative subject. Similar results were obtained for each time-point of all patients.

5.3.2 Between time-points

As seen before, the recovery from stroke has been monitored at three different stages: hyperacute, acute and chronic. Therefore, for each time-point, a cortical parcellation has to be provided. Freesurfer is a white-grey matter segmentation tool which performs very well and produces accurate results. However, it is very time consuming (up to 24-36 hours of computation per single parcellation) and, in case of patients with brain lesions, fine tuning its parameters is a very tricky operation. For these reasons, we decided to apply Freesurfer only at the chronic stage and to exploit registration algorithms for applying the extracted parcellation to the other time-points. At the chronic stage, in fact, most of the tissues involved in the stroke appear more clearly in T_1 images, and thus it is easier to tweak the parameters and guide Freesurfer in producing a more accurate parcellation of the remaining cortical surface not affected by the stroke.
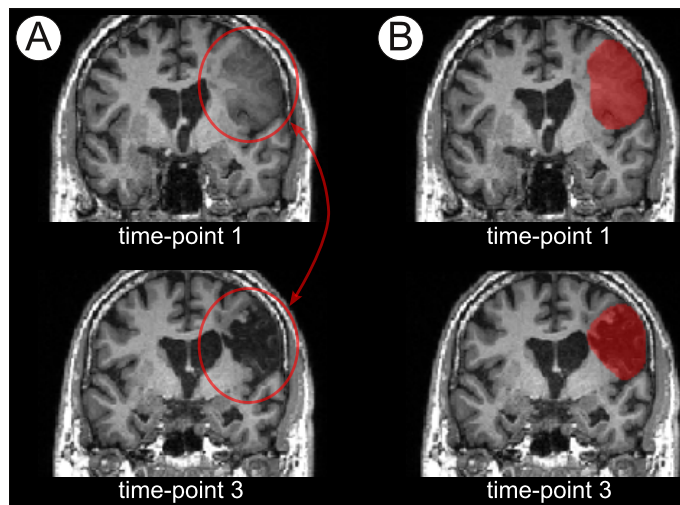

FIGURE 5.5: Between time-points registration. Figure (A) shows the same slice of a patient at hyperacute (top) and chronic (bottom) stages of the recovery after the stroke. Tissues involved by the lesion look very different at various stages, causing the registration among them to be particularly hard. To solve this, proper binary masks covering the lesion at each time-point are needed, as shown in (B).

The registration between the three time-points have been carried out using once again FSL FLIRT software, by using a 6 degree-of-freedom linear trasformation to match the T_1 images coming from each time-point. Since in this case the registration is applied on images with the same contrast, the correlation-ratio metric has been used. This is true for every pixel except in the areas involved by the stroke; in fact, tissues affected by stroke look very different at various stages of the disease (see figure 5.5 A). Moreover, in some cases, the

presence of edema may introduce some deformations in regions surrounding the lesion. For these reasons, even if registration is performed within the same subject, very big differences actually exist between the images. To solve this and to improve accuracy of registrations, proper binary masks covering the lesion at each time-point are needed, as shown in figure 5.5 в. These binary masks were manually drawn with the help of an expert neurologist.

5.4 Reproducibility of DSI tractography

Diffusion spectrum imaging is increasingly explored in clinical research. The quantitative value of the DSI technique, however, has still to be established. In this context, a better understanding of the reproducibility and the anatomical correspondence of the DSI tractography results is thus required. Although reproducibility has been studied comprehensively for diffusion tensor imaging [102], only few studies have considered this topic for Q-ball imaging and DSI analysis [103, 104]. Anatomical correspondence has been demonstrated in human DSI examinations for selected brain structures [16, 105]. For this reason, prior to processing patients data in order to search for variations in some properties of fibre connections which correlate with stroke recovery, we decided to investigate reproducibility and anatomical correspondence in serial DSI scans by focusing on the choice of tractography reconstruction parameters. Evaluations are based on connectivity measurements between cortical regions and on comparison with a histological atlas [106].

To this aim, we exploited the data of the twelve subjects in the control group to perform several tests with different combinations of tractography parameters, by using an in-house modified version of a standard line-propagation algorithm [107]. In particular, we were interested in the effects on the reproducibility and anatomical corrispondence of extracted fibres which arise from the modification of the following parameters:

- **turn angle**, *i.e.* the maximum allowed angle in the line-propagation procedure when following a fibre from one voxel to another;

- **ODF sharpening**, *i.e.* the level of filtering applied to the DSI data in order to make its diffusion maxima sharper.

The reproducibility was evaluated by means of the *Coefficient of Variation* (CV) between the tractography results at the two time-points. CV is defined as:

$$CV = \frac{\sigma}{\mu} \tag{5.1}$$

where μ and σ are, respectively, the mean and the standard deviation of the measures which has been used to study the connectivity at the two time-points. Since ground-truth data of calculated fibre tractography is not available, we assume that a reduced CV is a *better* result for serial scans. The correctness of this notion is supported by visual comparison with a connectivity atlas.

It is worth noting that in healthy subjects of all ages we do not expect any changes in connectivity or fibre properties during a 1-month period. Thus, CVs

above zero are attributed to variations arising from the image acquisition, reconstruction and/or tracking procedures. Anatomical correspondence was evaluated by comparing the results with a histology based connectivity atlas [106].

5.4.1   Fibre-crossing in the corona radiata

Crossing-fibres regions are very challenging in diffusion MRI. Because of its high angular resolution, DSI is a diffusion technique which is capable to resolve such crossing fibres. However, as we saw in chapter 2, DSI reconstruction method relies on Fourier transform and because of the low resolution of the 3D lattice it uses, this procedure can introduce some blurring of the ODF, causing some peaks to eventually become indistinguishable, as depicted in figure 5.6.
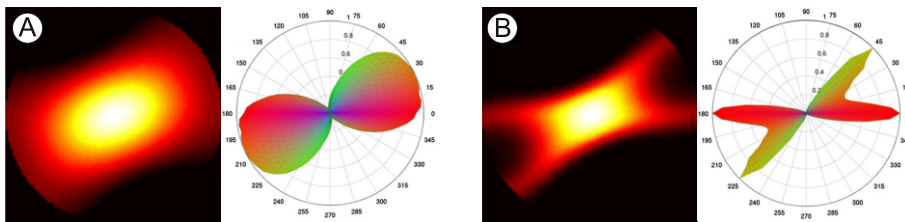

FIGURE 5.6: Blurring effect in DSI reconstruction. A 45° crossing-fibres region has been simulated. In (**A**) the reconstruction with the standard DSI method is shown. (**B**) shows results from an alternative reconstruction method [108].

Since such alternative reconstruction methods [108, 109, 110] were relatively new at the time of the present study, we decided to simply apply a *sharpness filter* to the data. This way, we managed to recover smaller but very important fibre bundles which otherwise would have been suppressed with the standard reconstruction method. This was particularly important for **elderly patients** in the *corona radiata* region, highlighted in figure 5.7 A, where the fibre bundles coming out from the *corpus callosum* (CC) are covered by the bigger *corticospinal tract* (CST) bundle. In figures 5.7 B-C it's easy to note that horizontal
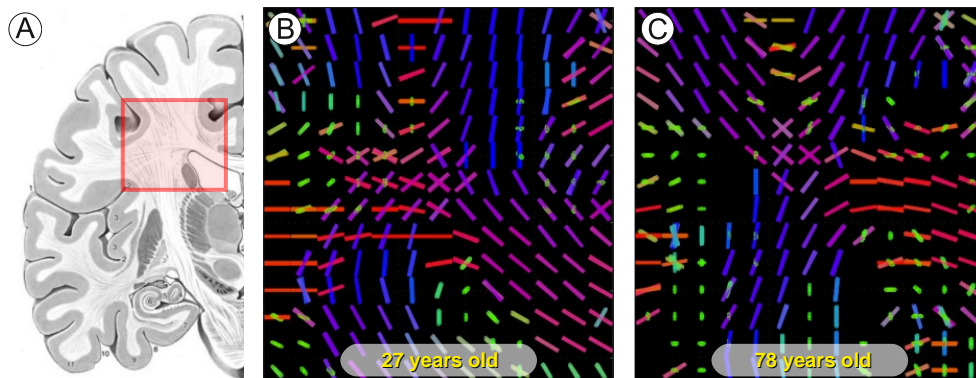

FIGURE 5.7: (**A**) Fibre-crossing in the *corona radiata*. *ODF maxima* obtained with standard DSI algorithm, with no sharpness filter, are shown for a *young* (**B**) and an *elderly* subject (**C**). Colored sticks are used to represent the diffusion maxima in every voxel and help to identify the local axonal orientation of underlying fibre populations.

red sticks out from CC, which are crossing the vertical blue sticks of the CST, are present in a young subject but not in an old one. However, both these tracts are deeply involved in the motor system. Hence, their proper identification turns out to be of particular importance for the purposes of the present study.

5.4.2 Effects of tractography parameters

When dealing with tractography algorithms, tweaking the parameters is a critic factor. Notably, the *turn angle* (TA) and the *ODF sharpening* (SF) play an important role as they act as a compromise between the loss of actual fibres and the inclusion of aberrant ones in final reconstructions. In fact, **increasing the TA** results in recovering more fibre bundles. Concerning the regions of interest for the present study, it is possible to recover more connections leaving the CC and pointing to the motor cortex. Moreover, if we **increase the SF**[3] on the data, the horizontal fibres which exit from the CC and pointing toward the lower part of the motor cortex can be successfully recovered. However, **increasing both TA and SF** results in recovering many more bundles, but the price to pay is the inclusion of lots of aberrant fibres.
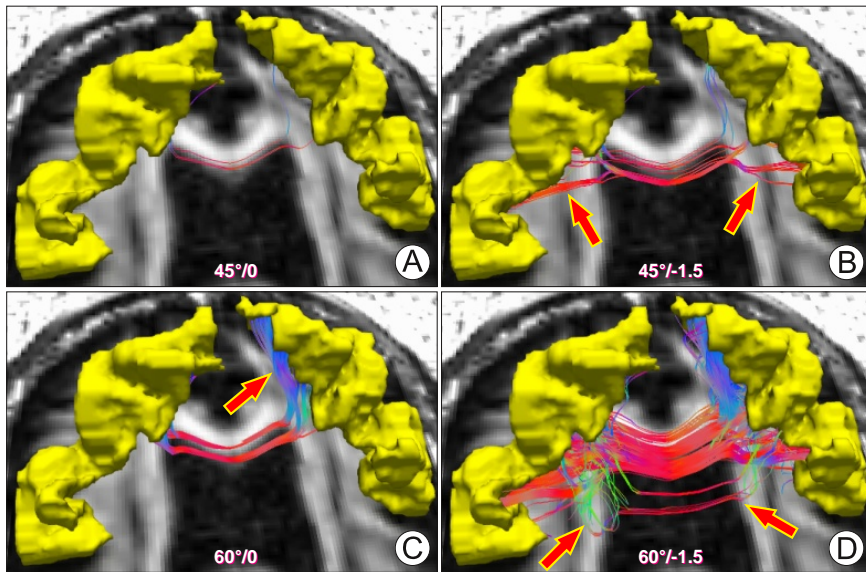
FIGURE 5.8: Tractography of the M1-M1 connections (yellow ROIs) in a healthy 64 years old subject. Reconstructions were performed with: (**A**) TA = 45° and SF = 0, (**B**) TA = 45° and SF = −1.5, (**C**) TA = 60° and SF = 0, (**D**) TA = 60° and SF = −1.5.

Figure 5.8 demonstrates the anatomical correspondence of the M1-M1 connections in a 64 year old healthy subject using four different parameter combinations. Tractography results using parameter set 1 (TA = 45° and SF = 0) showed only a few scattered fibres (subplot **A**). Parameter set 2 (TA = 45° and SF = −1.5) resulted in consistently more fibres (subplot **B**), pointing toward the lower part of the motor cortex (as indicated by the arrows in the subplot **B**). Parameter set 3 (TA = 60° and SF = 0) provides similar results with further

---

[3]Lower values of SF correspond to higher sharpness filter of the data

superior connections (blue bundles indicated by the arrow in subplot **C**) but less horizontal connections which, instead, were properly recovered with higher SF. The parameter combination 4 (TA = 60° and SF = −1.5) revealed more fibre bundles, including the horizontal and vertical ones found in subplot **B** and **C**, though also anatomically meaningless fibres appeared (subplot **D**).

Double ODF approach

To balance the effects of both turn angle and ODF sharpening, we introduced a simple modification in the tracking algorithm, which managed to recover most of the anatomically correct fibre bundles while reducing the inclusion of meaningless fibres. The idea is to reconstruct **two distinct ODFs** maps from DSI:

- one using the normal ODF reconstruction method, *i.e.* SF=0, and

- an additional one with sharpness filter applied on it, *i.e.* SF<0.

It is important to keep in mind that sharpening the data allows to recover some smaller bundles which have been blurred during the reconstruction process, but it could also introduce some spurious small peaks due to noise. Thus, we can exploit the information about smaller diffusion peaks contained in sharpened ODF by **constraining the algorithm** to use this information only in conjunction with a restricted turn angle. If such information doesn't allow the algorithm to propagate the fibre through the voxel, causing a meaningless termination of the tracking in white matter regions, then a compatible direction should be sought for in the additional ODF, namely the one with no sharpness filter. This ODF contains only the most probable diffusion directions, eventually blurred, thus the algorithm can safely increase the turn angle. If the tracking procedure manages to propagate the fibre thanks to this information, then the algorithm will continue using the sharpened ODF until the next stop, and so on.
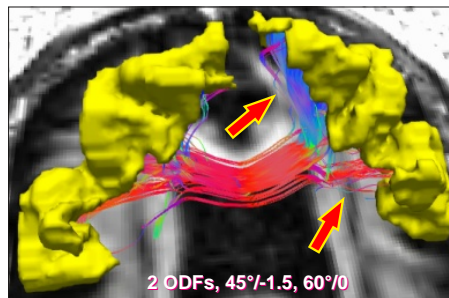
FIGURE 5.9: Double ODF approach. Tractography of the M1-M1 connections in a healthy 64 years old subject, performed using 2 ODFs/voxel

Figure 5.9 shows the results of tracking obtained using the double ODF approach with the following parameter set: 2 ODFs/voxel, TA = 45°/SF = −1.5 and TA = 60°/SF = 0 if the tracking stopped in a white matter region. Comparing these results with figure 5.8, it easy to see that most meaningful superior and horizontal fibres were successfully reconstructed, especially those indicated by the arrows in subplots **B** and **C**. At the same time, meaningless fibres were greatly reduced. Similar results were obtained in all subjects.

5.4.3 Measures of connectivity

Another important issue that need to be answered in order to perform quantitative analysis with DSI is *how to measure connectivity*. In literature, even if some efforts have been made in order to identify a stable and accurate measure of connectivity [111], most of the groups generally quantify the connectivity between two regions simply counting the **numbers of fibres**, *i.e.* number of fibres normalised by the total of extracted fibres in the brain, or trying to estimate the **density of fibres**, *i.e.* number of fibres normalised by the volume of both regions [103, 112]. In the following, we will call them count and density, respectively. They are defined as:

$$\mathsf{count}(R_1, R_2) = \frac{\text{number of fibres between } R_1 \text{ and } R_2}{\text{total number of fibres in the brain}} \tag{5.2}$$

$$\mathsf{density}(R_1, R_2) = \frac{\text{number of fibres between } R_1 \text{ and } R_2}{volume(R_1) + volume(R_2)} \tag{5.3}$$

where R_1 and R_2 are two cortical regions of the brain and $volume(\cdot)$ gives the volume of the region. Anyway, during our experiments we found that both measures revealed to be quite unstable. In fact, even big bundles such as CST gave high variability between the two time-points of the healthy subjects. This is probably due because there are several orders of magnitude between the resolution of MR acquisitions and the diameter of the axons, and so the actual density of fibres is a challenging concept to be characterised with MRI.
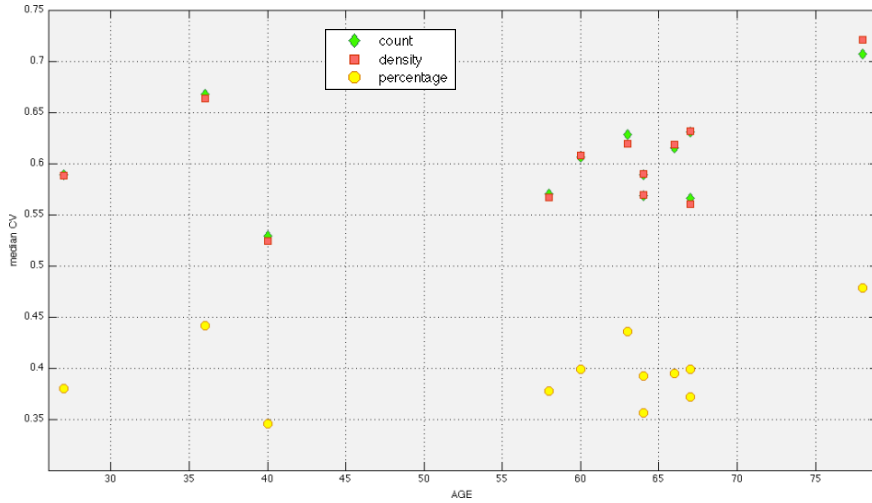
FIGURE 5.10: *Coefficient of variation* (CV) of connectivity measures. count, density and percentage have been plotted. For each subject, CV has been calculated from the two time-points for each pair of ROIs connections, and the median has been plotted.

At this aim, we have introduced a **new connectivity measure**, defined as:

$$\mathsf{percentage}(R_1, R_2) = \frac{\text{number of connected voxels between } R_1 \text{ and } R_2}{volume(R_1) + volume(R_2)} \tag{5.4}$$

which tries to quantify how two cortical regions are interconnected by simply counting the number of voxels which have at least one fibre connecting to the

other region. In doing this, it doesn't matter if a voxel $v_1 \in R_1$ has several connections pointing to the region R_2; the important information is that it is connected to the other region. This way we are trying to avoid the estimation of the density of that connection; instead, we are more interested in the percentage of the region R_1 which is involved in connections with the other region R_2.

Figure 5.10 compares the accuracy of the aforementioned measures of connectivity for a given tractography reconstruction. The graph reports, for each subject, the average CV between the two time-points calculated over each pair of cortical ROIs, by using the count, density and percentage measures of connectivity, respectively. The percentage metric (yellow circles) clearly exhibits the best performance, in that it gives lower CV values over all ages, thus being able to characterise the connectivity by means of a more stable and reliable property.

5.4.4 Reproducibility results

To investigate reproducibility of DSI tractography, several tests have been performed by varying the following parameters:

- 3 turn angles, *i.e.* TA = $\{30°, 45°, 60°\}$;

- 3 sharpness filters, *i.e.* SF = $\{0, -0.75, -1.5\}$;

- 1 or 2 ODFs per voxel.

For each subject and for each combination of parameters, the average CV between the two time-points calculated over each pair of cortical regions (ROIs) has been estimated. The connectivity between two ROIs was quantified using the three measures just introduced, count, density and percentage, respectively.
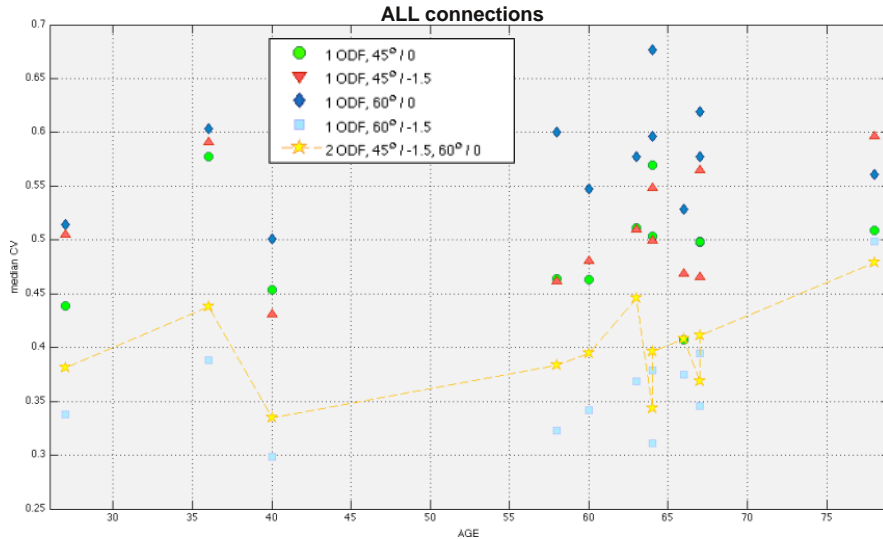

FIGURE 5.11: Reproducibility of DSI tractography for *all brain connections*. The average CV between the two time-points is plotted for each subject. The connectivity between two ROIs was quantified using the percentage measure. Only a subset of all tested combinations of parameters have been reported.

Figure 5.11 reports the results for the reproducibility comparison for a subset of all tested combinations of parameters, where the connectivity was estimated by means of the `percentage` measure. Comparable results were found with the combinations not included in the figure. The **double-ODF approach** (yellow line) clearly performs well, in that it gives CVs lower than most of the other combinations of parameters. It's worthy to note that also the tractography performed with 1 ODF and TA = 60°/SF = −1.5 parameters (lightblue squares) appears to have similar reproducibility scores. However, it's important to remember that this parameter set introduces a lot of aberrant fibres (recall figure 5.8 D). Therefore, it turns out that the double-ODF approach manages to achieve a high reproducibility while reducing the number of anatomical non-existent fibres. For completeness, figures 5.13 A-B report the results of the reproducibility comparison by means of the two other measures of connectivity, `count` and `density`, respectively.
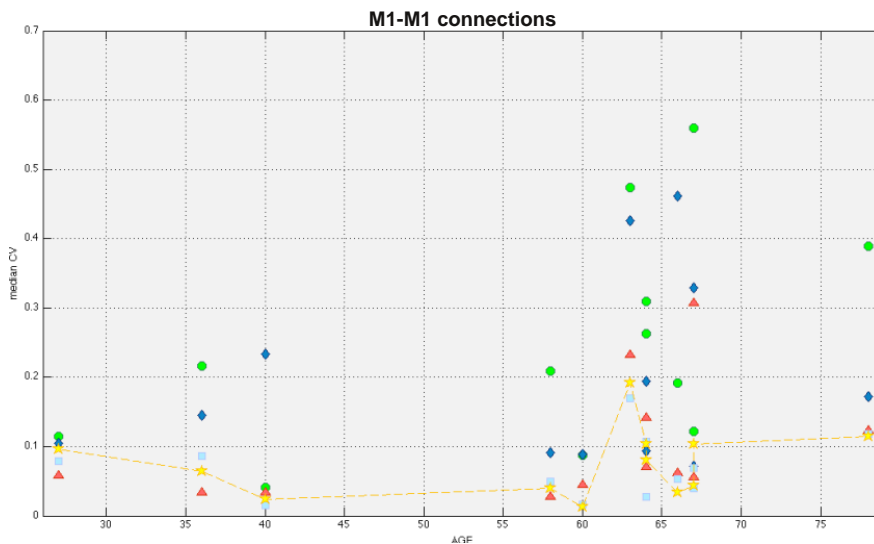
FIGURE 5.12: Reproducibility of DSI tractography in the case of *M1-M1 connections* only. The connectivity between two cortical areas was quantified using the `percentage` measure. Similar results have been obtained with the other connectivity measures (data not shown).

Finally, as reported in figure 5.12, the double-ODF approach was found to be particularly advantageous in the M1-M1 analysis for **elderly subjects** (> 50 years). In fact, whereas most methods seem to get worse as the age increases, the CVs in the case of the double-ODF approach appear to be quite stable compared to the others. This could be due to the fact that widely used DSI reconstruction parameters have been optimized in young healthy subjects [113]. Normal aging, however, may lead to changes in MRI properties and contrast. Consequently, these reconstruction parameters may appear suboptimal for older subjects. We speculate that certain diseases may further influence the reconstruction results. This issue appears to be very interesting and worthy to be fully explained, and thus it will be part of some future projects.

Summarising, DSI tractography results demonstrate to be very sensitive to the choice of reconstruction parameters. In particular in serial scans and when investigating inhomogeneous subject populations a careful adaptation of reconstruction parameters may render the results more reproducible and accurate. Concerning this, by *simultaneously* modulating the *sharpness filter* and limiting the inclusion of anatomical non-existent fibre bundles by restricting the *turn angle*, we managed to improve the standard line-propagation fibre-tracking algorithm increasing its reproducibility for subjects of all ages while keeping invariate the computional time.
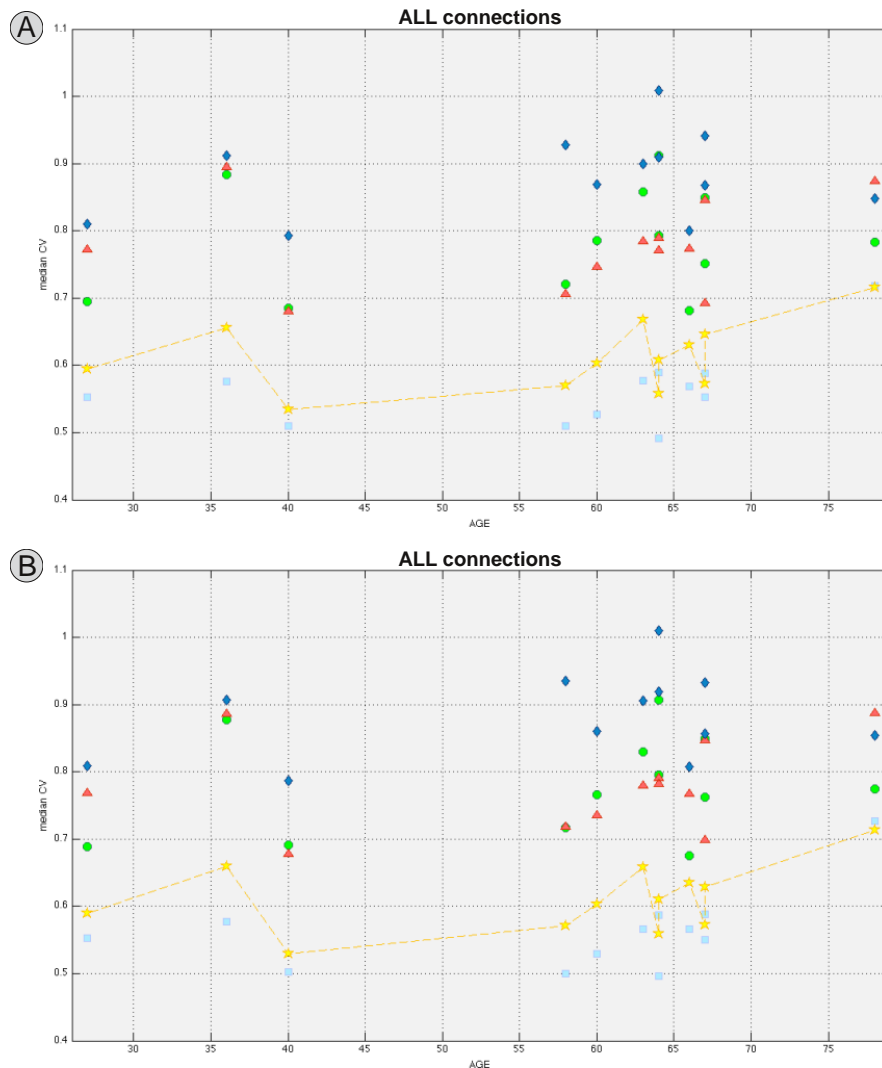

FIGURE 5.13: For sake of completeness, the reproducibility of DSI tractography has been compared also by measuring the connectivity between cortical regions with count (A) and density (B) measures. Similar results were found with these two metrics; however, as already seen in the chapter, percentage appeared to be more stable (lower CVs values).

5.5 Preliminary results

We so far analysed the data from 3 time-points of 8 patients following the steps reported above. All the patients functionally recovered at six month after stroke, as reported in table 5.1 by means of ranking, NIHSS and FIM scores:

	Hyperacute	**Six months**
Ranking	2.88 ± 0.99	1.38 ± 0.52
nihss	10.00 ± 5.48	2.63 ± 2.13
fim	94.25 ± 26.26	121.50 ± 7.52

Table 5.1: *Functional recovery* of the 8 patients so far analysed by means of ranking, NIHSS and FIM scores. Mean $\pm$ standard deviation values are reported at hyperacute (*i.e.* time point 1) and chronic (*i.e.* time point 3) stages.

In this group of patients with strokes affecting the motor cortex we could observe remodeling of the connectivity over six months after stroke both in the hemisphere ipsilateral to the stroke and in the healthy hemisphere contralateral to the lesion. In addition, we found interesting changes in the interhemispheric connections between the *primary motor areas* M1 and the *secondary motor areas* SMA (Supplementary Motor Area).
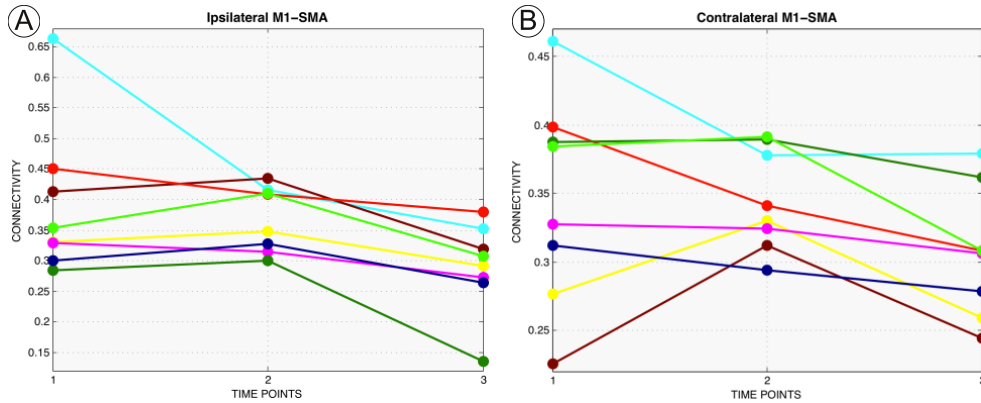
Figure 5.14: Connectivity at the three time points of *ipsilateral* (**A**) and *contralateral* (**B**) connections between M1 and SMA areas for the eight patients so far analysed. The connectivity was measured by means of the `percentage` metric.

As expected, the connectivity between the M1 area and the SMA area **ipsilateral to the stroke** region showed a substantial decrease over the six months follow-up after the acute event, figure 5.14 A. The most dramatic reduction was observed in the youngest patient, who was 25 years old at the time of the stroke (cyan profile). This observation is in line with previous functional MRI (fMRI) studies reporting ipsilesional dysfunction of the M1 to SMA coupling in patients affected from sub-cortical stroke [114, 115]. In our case, this phenomenon could of course also be due to the direct lesion effect in these areas provoked by the stroke. In order to clarify this point, further assessment of stroke volume and M1 involvement in the stroke area should be performed in future.
Interestingly, also the M1-SMA connections in the **contralateral hemisphere**

underwent a structural remodeling: 6 out of 8 patients showed a progressive decrease of the connectivity between the primary and the secondary motor area considered, as shown in figure 5.14 B. Considering that SMA is known to inhibit the M1 area [116], this could mean that the contralateral motor area structurally remodel in order to disinhibit the unaffected M1 as a compensatory mechanism during motor function recovery. However, this mechanism was not observed in 2 out of 8 patients (brown and yellow profiles).
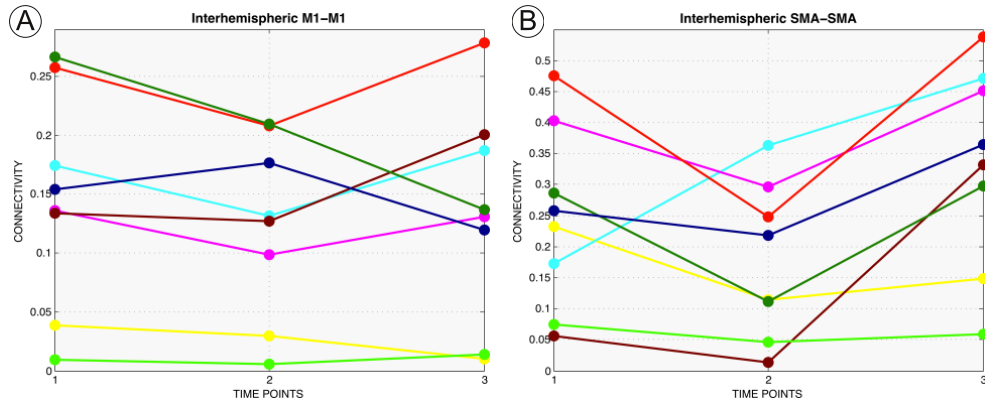

FIGURE 5.15: Connectivity at the three time points of *interhemispheric connections* between primary (**A**) and secondary (**B**) motor areas for the eight patients so far analysed. The connectivity was measured by means of the `percentage` metric.

Concerning the **interhemispheric connections**, figure 5.15 A shows that the connections between the ipsi and contralateral M1 areas slightly increased in 4 out of 8 patients during the process of functional recovery. In other 2 patients these connections did not substantially change whereas in the last 2 patients they slightly decreased. In addition, all the patients showed a clear relative increase of interhemispheric connections between the secondary motor areas SMA, as clearly visible in figure 5.15 B.

The increase of interhemispheric connections between primary and secondary motor areas could be part of a compensatory mechanism during functional recovery after stroke. It's very well known that the M1-M1 and SMA-SMA interhemispheric connections have reciprocal inhibitory influences [117, 118]. It has also been reported that, in patients with chronic stroke and good functional recovery, the degree of the inhibitory influences between M1-M1 and SMA-SMA areas decreases [114, 115]. These findings seem also to clearly confirm the hypothesis that there is reorganization within the SMA after stroke [119]. The SMA has been shown to be plastic under different circumstances. For example, SMA reorganization has been reported in healthy subjects trained with increasing force [120] and in stroke patients asked to perform index-finger tapping [90, 121]. Indeed, enhancement of SMA activity, (*i.e.* by high-frequency transcranial magnetic or direct current stimulation) has been suggested as a potential means for ameliorating M1 dysfunction after stroke [122, 123].

In summary, our preliminary results show potential structural mechanisms of brain rewiring underlying the recovery of function after stroke. Future analysis should confirm or confute these findings.

Chapter 6

Conclusions

As already pointed out, this dissertation is based on three different projects, each one covering a separate topic. For this reason, each previous chapter has its own conclusions at the end of it. However, at this point it's worthwhile to summarise the main contributions of the present work.

Concerning the project on manganese-enhanced MRI technique illustrated in chapter 3, we successfully established a methodology for the absolute quantification of Mn concentration in the rat brain. This method is based on fast T_1 mapping and coregistration of images to an anatomical brain atlas. The sequence for fast T_1 mapping has been tested on ex-vivo data end calibrated with spectroscopic measurements. Furthermore, the spatial coregistration to the anatomical brain atlas allowed to identify the regions in which Mn accumulates. This way, from the calculated Mn concentrations it is possible to infer the location of regions activated during a specific task. This protocol, thus, may allow to conduct functional MRI experiments in which a stimulus is applied to awake animals behaving normally.

In the field of experimental tumour models characterisation, the classification of the tissues affected by the tumour is crucial. Classical DCEMRI analysis methods employ pharmacokinetic models which effectively describe the vascular perfusion in the region of the tumour, but suffer from large output variability. At this aim, we proposed to work directly on DCEMRI data with a model-free approach, combining clustering and machine learning techinques in order to infer the most discriminative properties of the data which allow to better classify the involved tissues. We have shown that this analysis method performs better than standard model based approaches in producing histologically meaningful partitions of the tumour. Moreover, we successfully validated it in a real case application for the evaluation of the efficacy of an anti-cancer therapy, thus demonstrating the effectiveness of our proposed approach.

Finally, in the stroke project, brain connectivity has been monitored with Diffusion Spectrum Imaging in order to study the plasticity of the human brain from a structural point-of-view during its functional recovery after the stroke. To obtain the necessary sensitivity to structural modifications, a careful survey on fibre tracts reproducibility, reconstructed by an in-house developed fibre-

tracking procedure, has been conducted on healthy subjects. By using the parameter set giving the best reproducibility, connections between primary and secondary motor areas have been carefully extracted. Our preliminary results have given evidences of potential structural mechanisms of brain rewiring underlying the recovery of function after stroke. These findings are in line with well-known results obtained by functional MRI and pave the way for getting more insights about brain plasticity mechanisms.

Bibliography

[1] C. Beaulieu, "The basis of anisotropic water diffusion in the nervous system - a technical review," *NMR Biomed*, vol. 15, no. 7-8, pp. 435–55, 2002.

[2] P. J. Basser, J. Mattiello, and D. LeBihan, "Estimation of the effective self-diffusion tensor from the NMR spin echo," *J Magn Reson B*, vol. 103, pp. 247–54, Mar 1994.

[3] P. J. Basser, J. Mattiello, and D. LeBihan, "MR diffusion tensor spectroscopy and imaging," *Biophys J*, vol. 66, pp. 259–67, Jan 1994.

[4] J. Mattiello, P. J. Basser, and D. Le Bihan, "The b matrix in diffusion tensor echo-planar imaging," *Magn Reson Med*, vol. 37, pp. 292–300, Feb 1997.

[5] P. T. Callaghan, *Principles of nuclear magnetic resonance microscopy*. Oxford, England: Clarendon, 1991.

[6] V. J. Wedeen, "Mapping fiber orientation spectra in cerebral white matter with Fourier transform diffusion MRI," in *8th Annual Meeting of the ISMRM*, pp. 82–82, 2000.

[7] E. Stejskal, "Use of spin echoes in a pulsed magnetic-field gradient to study anisotropic, restricted diffusion and flow," *The Journal of Chemical Physics*, vol. 43, no. 10, pp. 3597–3603, 1965.

[8] D. S. Tuch, "Q-ball imaging," *Magn Reson Med*, vol. 52, pp. 1358–72, Dec 2004.

[9] D. C. Alexander and G. J. Barker, "Optimal imaging parameters for fiber-orientation estimation in diffusion MRI," *Neuroimage*, vol. 27, pp. 357–67, Aug 2005.

[10] D. C. Alexander, "Multiple-fiber reconstruction algorithms for diffusion MRI," *Ann N Y Acad Sci*, vol. 1064, pp. 113–33, Dec 2005.

[11] X. Gigandet, *Global Brain Connectivity Analysis by Diffusion MR Tractography: Algorithms, Validation and Applications*. PhD thesis, Jan 2009.

[12] B. W. Kreher, I. Mader, and V. G. Kiselev, "Gibbs tracking: a novel approach for the reconstruction of neuronal pathways," *Magn Reson Med*, vol. 60, pp. 953–963, Oct 2008.

[13] S. Mori, B. J. Crain, V. P. Chacko, and P. C. van Zijl, "Three-dimensional tracking of axonal projections in the brain by magnetic resonance imaging," *Ann Neurol*, vol. 45, pp. 265–9, Feb 1999.

[14] R. Xue, P. C. van Zijl, B. J. Crain, M. Solaiyappan, and S. Mori, "In vivo three-dimensional reconstruction of rat brain axonal projections by diffusion tensor imaging," *Magn Reson Med*, vol. 42, pp. 1123–7, Dec 1999.

[15] T. E. Conturo, N. F. Lori, T. S. Cull, E. Akbudak, A. Z. Snyder, J. S. Shimony, R. C. McKinstry, H. Burton, and M. E. Raichle, "Tracking neuronal fiber pathways in the living human brain," *Proc Natl Acad Sci U S A*, vol. 96, pp. 10422–7, Aug 1999.

[16] J. D. Schmahmann, D. N. Pandya, R. Wang, G. Dai, H. E. D'Arceuil, A. J. de Crespigny, and V. J. Wedeen, "Association fibre pathways of the brain: parallel observations from diffusion spectrum imaging and autoradiography," *Brain*, vol. 130, pp. 630–53, Mar 2007.

[17] C. P. Lin, W. Y. Tseng, H. C. Cheng, and J. H. Chen, "Validation of diffusion tensor magnetic resonance axonal fiber imaging with registered manganese-enhanced optic tracts," *Neuroimage*, vol. 14, pp. 1035–47, Nov 2001.

[18] I. Aoki, S. Naruse, and C. Tanaka, "Manganese-enhanced magnetic resonance imaging (MEMRI) of brain activity and applications to early detection of brain ischemia," *NMR Biomed*, vol. 17, pp. 569–80, Dec 2004.

[19] A. C. Silva, J. H. Lee, I. Aoki, and A. P. Koretsky, "Manganese-enhanced magnetic resonance imaging (MEMRI): methodological and practical considerations," *NMR Biomed*, vol. 17, pp. 532–43, Dec 2004.

[20] I. Aoki, C. Tanaka, T. Takegami, T. Ebisu, M. Umeda, M. Fukunaga, K. Fukuda, A. C. Silva, A. P. Koretsky, and S. Naruse, "Dynamic activity-induced manganese-dependent contrast magnetic resonance imaging (DAIM MRI)," *Magn Reson Med*, vol. 48, pp. 927–33, Dec 2002.

[21] Y.-T. Kuo, A. H. Herlihy, P.-W. So, and J. D. Bell, "Manganese-enhanced magnetic resonance imaging (MEMRI) without compromise of the blood-brain barrier detects hypothalamic neuronal activity in vivo," *NMR Biomed*, vol. 19, pp. 1028–34, Dec 2006.

[22] X. Yu, Y. Z. Wadghiri, D. H. Sanes, and D. H. Turnbull, "In vivo auditory brain mapping in mice with Mn-enhanced MRI," *Nat Neurosci*, vol. 8, pp. 961–8, Jul 2005.

[23] A. Van der Linden, N. Van Camp, P. Ramos-Cabrer, and M. Hoehn, "Current status of functional MRI on small animals: application to physiology,

pathophysiology, and cognition," *NMR Biomed*, vol. 20, pp. 522–45, Aug 2007.

[24] E. Kaldoudi and S. C. R. Williams, "Relaxation time measurements in NMR imaging. Part I: Longitudinal relaxation time," *Concepts in Magnetic Resonance*, vol. 5, no. 3, pp. 217–242, 1993.

[25] A. Haase, J. Frahm, D. Matthaei, W. Hanicke, and K. D. Merboldt, "FLASH imaging. Rapid NMR imaging using low flip-angle pulses," *Journal of Magnetic Resonance (1969)*, vol. 67, no. 2, pp. 258–266, 1986.

[26] R. Deichmann and A. Haase, "Quantification of T1 values by SNAPSHOT-FLASH NMR imaging," *Journal of Magnetic Resonance (1969)*, vol. 96, no. 3, pp. 608–612, 1992.

[27] K. Scheffler and J. Hennig, "T1 quantification with inversion recovery TrueFISP," *Magn Reson Med*, vol. 45, pp. 720–3, Apr 2001.

[28] G. Brix, L. R. Schad, M. Deimling, and W. J. Lorenz, "Fast and precise T1 imaging using a TOMROP sequence," *Magn Reson Imaging*, vol. 8, no. 4, pp. 351–6, 1990.

[29] G. Paxinos and C. Watson, *The rat brain in stereotaxic coordinates*. 4th ed., 1998.

[30] A. J. Schwarz, A. Danckaert, T. Reese, A. Gozzi, G. Paxinos, C. Watson, E. V. Merlo-Pich, and A. Bifone, "A stereotaxic MRI template set for the rat brain with tissue class distribution maps and co-registered anatomical atlas: application to pharmacological MRI," *Neuroimage*, vol. 32, pp. 538–50, Aug 2006.

[31] M. Jenkinson and S. Smith, "A global optimisation method for robust affine registration of brain images," *Med Image Anal*, vol. 5, pp. 143–156, Jun 2001.

[32] B. M. Weaver, G. E. Staddon, and W. W. Mapleson, "Tissue/blood and tissue/water partition coefficients for propofol in sheep," *Br J Anaesth*, vol. 86, pp. 693–703, May 2001.

[33] W. Nordhøy, H. W. Anthonsen, M. Bruvold, H. Brurok, S. Skarra, J. Krane, and P. Jynge, "Intracellular manganese ions provide strong T_1 relaxation in rat myocardium," *Magn Reson Med*, vol. 52, pp. 506–14, Sep 2004.

[34] J. H. Lee, A. C. Silva, H. Merkle, and A. P. Koretsky, "Manganese-enhanced magnetic resonance imaging of mouse brain after systemic administration of MnCl2: dose-dependent and temporal evolution of T1 contrast," *Magn Reson Med*, vol. 53, pp. 640–8, Mar 2005.

[35] F. Serrano, M. Deshazer, K. D. B. Smith, J. S. Ananta, L. J. Wilson, and R. G. Pautler, "Assessing transneuronal dysfunction utilizing manganese-enhanced MRI (MEMRI)," *Magn Reson Med*, vol. 60, pp. 169–75, Jul 2008.

[36] J. Yang, P.-L. Khong, Y. Wang, A. C.-Y. Chu, S.-L. Ho, P.-T. Cheung, and E. X. Wu, "Manganese-enhanced MRI detection of neurodegeneration in neonatal hypoxic-ischemic cerebral injury," *Magn Reson Med*, vol. 59, pp. 1329–39, Jun 2008.

[37] N. A. Bock, F. F. Paiva, and A. C. Silva, "Fractionated manganese-enhanced MRI," *NMR Biomed*, vol. 21, pp. 473–8, Jun 2008.

[38] A. C. Silva and N. A. Bock, "Manganese-enhanced MRI: an exceptional tool in translational neuroimaging," *Schizophr Bull*, vol. 34, pp. 595–604, Jul 2008.

[39] S. Aime, L. Anelli, M. Botta, M. Brocchetta, S. Canton, F. Fedeli, E. Gianolio, and E. Terreno, "Relaxometric evaluation of novel manganese(II) complexes for application as contrast agents in magnetic resonance imaging," *J Biol Inorg Chem*, vol. 7, pp. 58–67, Jan 2002.

[40] F. M. Cavagna, P. Marzola, M. Daprà, F. Maggioni, E. Vicinanza, P. M. Castelli, C. de Haën, C. Luchinat, M. F. Wendland, and M. Saeed, "Binding of gadobenate dimeglumine to proteins extravasated into interstitial space enhances conspicuity of reperfused infarcts," *Invest Radiol*, vol. 29 Suppl 2, pp. S50–3, Jun 1994.

[41] G. Parker and D. Buckley, *Tracer kinetic modelling for T1-weighted dynamic contrast-enhanced MRI*, vol. Dynamic contrast-enhanced Magnetic Resonance Imaging in Oncology, pp. 81–92. 2005.

[42] J. P. B. O'Connor, A. Jackson, G. J. M. Parker, and G. C. Jayson, "DCE-MRI biomarkers in the clinical evaluation of antiangiogenic and vascular disrupting agents," *Br J Cancer*, vol. 96, pp. 189–95, Jan 2007.

[43] P. S. Tofts and A. G. Kermode, "Measurement of the blood-brain barrier permeability and leakage space using dynamic mr imaging. 1. fundamental concepts," *Magn Reson Med*, vol. 17, pp. 357–67, Feb 1991.

[44] H. B. Larsson, M. Stubgaard, J. L. Frederiksen, M. Jensen, O. Henriksen, and O. B. Paulson, "Quantitation of blood-brain barrier defect by magnetic resonance imaging and gadolinium-DTPA in patients with multiple sclerosis and brain tumors," *Magn Reson Med*, vol. 16, pp. 117–31, Oct 1990.

[45] L. A. Liotta and E. C. Kohn, "The microenvironment of the tumour-host interface," *Nature*, vol. 411, pp. 375–379, May 2001.

[46] M. M. Mueller and N. E. Fusenig, "Friends or foes - bipolar effects of the tumour stroma in cancer," *Nat Rev Cancer*, vol. 4, pp. 839–849, Nov 2004.

[47] O. Casanovas, D. J. Hicklin, G. Bergers, and D. Hanahan, "Drug resistance by evasion of antiangiogenic targeting of VEGF signaling in late-stage pancreatic islet tumors," *Cancer Cell*, vol. 8, pp. 299–309, Oct 2005.

[48] G. Bergers and D. Hanahan, "Modes of resistance to anti-angiogenic therapy," *Nat Rev Cancer*, vol. 8, pp. 592–603, Aug 2008.

[49] P. Marzola, A. Degrassi, L. Calderan, P. Farace, C. Crescimanno, E. Nicolato, A. Giusti, E. Pesenti, A. Terron, A. Sbarbati, T. Abrams, L. Murray, and F. Osculati, "In vivo assessment of antiangiogenic activity of SU6668 in an experimental colon carcinoma model," *Clin Cancer Res*, vol. 10, pp. 739–750, Jan 2004.

[50] F. Demsar, T. P. Roberts, H. C. Schwickert, D. M. Shames, C. F. van Dijke, J. S. Mann, M. Saeed, and R. C. Brasch, "A MRI spatial mapping technique for microvascular permeability and tissue blood volume based on macromolecular contrast agent distribution," *Magn Reson Med*, vol. 37, pp. 236–242, Feb 1997.

[51] Z. M. Bhujwalla, D. Artemov, K. Natarajan, E. Ackerstaff, and M. Solaiyappan, "Vascular differences detected by MRI for metastatic versus nonmetastatic breast and prostate cancer xenografts," *Neoplasia*, vol. 3, pp. 143–153, Mar-Apr 2001.

[52] M. O. Leach, K. M. Brindle, J. L. Evelhoch, J. R. Griffiths, M. R. Horsman, A. Jackson, G. C. Jayson, I. R. Judson, M. V. Knopp, R. J. Maxwell, D. McIntyre, A. R. Padhani, P. Price, R. Rathbone, G. J. Rustin, P. S. Tofts, G. M. Tozer, W. Vennart, J. C. Waterton, S. R. Williams, P. Workman, and Pharmacodynamic/Pharmacokinetic Technologies Advisory Committee, Drug Development Office, Cancer Research UK, "The assessment of antiangiogenic and antivascular therapies in early-stage clinical trials using magnetic resonance imaging: issues and recommendations," *Br J Cancer*, vol. 92, pp. 1599–1610, May 2005.

[53] A. Jackson, J. P. O'Connor, G. J. Parker, and G. C. Jayson, "Imaging tumor vascular heterogeneity and angiogenesis using dynamic contrast-enhanced magnetic resonance imaging," *Clin Cancer Res*, vol. 13, pp. 3449–3459, Jun 2007.

[54] D. Checkley, J. J. Tessier, J. Kendrew, J. C. Waterton, and S. R. Wedge, "Use of dynamic contrast-enhanced MRI to evaluate acute treatment with ZD6474, a VEGF signalling inhibitor, in PC-3 prostate tumours," *Br J Cancer*, vol. 89, pp. 1889–1895, Nov 2003.

[55] E. O'Connor, N. Fieller, A. Holmes, and J. Waterton, "How to analyse dynamic MRI in oncology; advanced histogram analysis gives better statistical power & insight than simple averaging," in *Proceedings of the International Society of Magnetic Resonance in Medicine*, 2005.

[56] C. Ding and X. He, "Cluster structure of K-means clustering via principal component analysis," vol. 3056, pp. 414–418, 2004.

[57] C. Timke, H. Zieher, A. Roth, K. Hauser, K. E. Lipson, K. J. Weber, J. Debus, A. Abdollahi, and P. E. Huber, "Combination of vascular endothelial growth factor receptor/platelet-derived growth factor receptor inhibition markedly improves radiation tumor therapy," *Clin Cancer Res*, vol. 14, pp. 2210–9, Apr 2008.

[58] M. R. Horsman and D. W. Siemann, "Pathophysiologic effects of vascular-targeting agents and the implications for combination with conventional therapies," *Cancer Res*, vol. 66, pp. 11520–39, Dec 2006.

[59] P. Y. Lau, S. Ozawa, and F. C. T. Voon, "Using block-based multiparameter representation to detect tumor features on T2-weighted brain MRI images," *Methods of Information in Medicine*, vol. 46, no. 2, pp. 236–241, 2007.

[60] R. Duda, P. Hart, and D. Stork, *Pattern Classification*. John Wiley and Sons, second ed., 2001.

[61] U. Castellani, M. Cristani, P. Marzola, V. Murino, E. Rossato, and A. Sbarbati, "Cancer area characterization by non-parametric clustering," in *Workshop on Intelligent Data Analysis in bioMedicine And Pharmacology*, pp. 25–30, 2006.

[62] D. Buckley, "Uncertainty in the analysis of tracer kinetics using dynamic contrast enhanced T1-weighted MRI," *Magnetic Resonance Med*, vol. 47, pp. 601–606, 2002.

[63] J. U. Harrer, G. Parker, H. Haroon, D. Buckley, K. Embelton, C. Roberts, and et al., "Comparative study of methods for determining vascular permeability and blood volume in human gliomas," *Magnetic Resonance Imaging*, vol. 20, pp. 748–757, 2004.

[64] C. Lavinia, M. de Jongea, M. V. de Sandeb, P. Takb, A. J. Nederveena, and M. Maas, "Pixel-by-pixel analysis of DCE MRI curve patterns and an illustration of its application to the imaging of the musculoskeletal system," *Magnetic Resonance Imaging*, vol. 25, pp. 604–612, 2007.

[65] P. Tofts, G. Briks, D. Buckley, J. Evelhoch, E. Henderson, M. Knopp, and et al., "Estimating kinetic parameters from dynamic contrast enhanced T1-w MRI of a diffusible tracer: standardized quantities and symbols," *Magnetic Resonance Imaging*, vol. 10, pp. 223–232, 1999.

[66] M. J. Stoutjesdijk, J. Veltman, M. Huisman, N. Karssemeijer, J. Barents, and et al., "Automatic analysis of contrast enhancent in breast MRI lesions using Mean Shift clustering for roi selection," *Journal of Magnetic Resonance Imaging*, vol. 26, pp. 606–614, 2007.

[67] D. Comaniciu and P. Meer, "Mean shift: A robust approach toward feature space analysis," *IEEE Trans. Pattern Anal. Mach. Intell.*, vol. 24, no. 5, pp. 603–619, 2002.

[68] C. Burges, "A tutorial on support vector machine for pattern recognition," *Data Mining and Knowledge Discovery*, vol. 2, pp. 121–167, 1998.

[69] P. Marzola, S. Ramponi, E. Nicolato, E. Lovati, M. Sandri, L. Calderan, C. Crescimanno, F. Merigo, A. Sbarbati, A. Grotti, S. Vultaggio, F. Cavagna, V. L. Russo, and F. Osculati, "Effect of tamoxifen in an experimental model of breast tumor studied by dynamic contrast-enhanced magnetic resonance imaging and different contrast agents," *Investigative radiology*, vol. 40, no. 7, pp. 421–429, 2005.

[70] T. Twellmann, A. Saalbach, C. Muller, T. W. Nattkemper, and A. Wismuller, "Detection of suspicious lesions in dynamic contrast enhanced MRI data," in *Engineering in Medicine and Biology Society*, pp. 454–457, 2004.

[71] L. Leistritz, W. Hesse, T. Wüstenberg, C. Fitzek, J. R. Reichenbach, and H. Witte, "Time-variant analysis of fast-fMRI and dynamic contrast agent MRI sequences as examples of 4-dimensional image analysis," *Methods of Information in Medicine*, vol. 45, no. 6, pp. 643–650, 2006.

[72] C.-C. Chang and C.-J. Lin, *LIBSVM: a library for support vector machines*, 2001.

[73] P. Marzola, A. Degrassi, L. Calderan, P. Farace, E. Nicolato, C. Crescimanno, M. Sandri, A. Giusti, E. Pesenti, A. Terron, A. Sbarbati, and F. Osculati, "Early antiangiogenic activity of SU11248 evaluated in vivo by dynamic contrast-enhanced magnetic resonance imaging in an experimental model of colon carcinoma," *Clin Cancer Res*, vol. 11, pp. 5827–32, Aug 2005.

[74] M. L. Dombovy, "Understanding stroke recovery and rehabilitation: current and emerging approaches," *Curr Neurol Neurosci Rep*, vol. 4, pp. 31–5, Jan 2004.

[75] S. B. Frost, S. Barbay, K. M. Friel, E. J. Plautz, and R. J. Nudo, "Reorganization of remote cortical regions after ischemic brain injury: a potential substrate for stroke recovery," *J Neurophysiol*, vol. 89, pp. 3205–14, Jun 2003.

[76] P. D. Wall, "Mechanisms of plasticity of connection following damage in adult mammalian nervous system," in *Recovery of function: theoretical consideration for brain injury rehabilitation* (P. Bach-y Rita, ed.), pp. 91–100, Hans Huber, Bern, 1980.

[77] O. W. Witte, H. J. Bidmon, K. Schiene, C. Redecker, and G. Hagemann, "Functional differentiation of multiple perilesional zones after focal cerebral ischemia," *J Cereb Blood Flow Metab*, vol. 20, pp. 1149–65, Aug 2000.

[78] T. A. Jones and T. Schallert, "Overgrowth and pruning of dendrites in adult rats recovering from neocortical damage," *Brain Res*, vol. 581, pp. 156–60, May 1992.

[79] R. P. Stroemer, T. A. Kent, and C. E. Hulsebosch, "Enhanced neocortical neural sprouting, synaptogenesis, and behavioral recovery with D-amphetamine therapy after neocortical infarction in rats," *Stroke*, vol. 29, pp. 2381–93; discussion 2393–5, Nov 1998.

[80] T. Kawamata, W. D. Dietrich, T. Schallert, J. E. Gotts, R. R. Cocke, L. I. Benowitz, and S. P. Finklestein, "Intracisternal basic fibroblast growth factor enhances functional recovery and up-regulates the expression of a molecular marker of neuronal sprouting following focal cerebral infarction," *Proc Natl Acad Sci U S A*, vol. 94, pp. 8179–84, Jul 1997.

[81] B. Kolb, S. Cote, A. Ribeiro-da Silva, and A. C. Cuello, "Nerve growth factor treatment prevents dendritic atrophy and promotes recovery of function after cortical injury," *Neuroscience*, vol. 76, pp. 1139–51, Feb 1997.

[82] S. S. Magavi, B. R. Leavitt, and J. D. Macklis, "Induction of neurogenesis in the neocortex of adult mice," *Nature*, vol. 405, pp. 951–5, Jun 2000.

[83] S. T. Carmichael, L. Wei, C. M. Rovainen, and T. A. Woolsey, "New patterns of intracortical projections after focal cortical stroke," *Neurobiol Dis*, vol. 8, pp. 910–22, Oct 2001.

[84] R. J. Nudo, B. M. Wise, F. SiFuentes, and G. W. Milliken, "Neural substrates for the effects of rehabilitative training on motor recovery after ischemic infarct," *Science*, vol. 272, pp. 1791–4, Jun 1996.

[85] C. Xerri, M. M. Merzenich, B. E. Peterson, and W. Jenkins, "Plasticity of primary somatosensory cortex paralleling sensorimotor skill recovery from stroke in adult monkeys," *J Neurophysiol*, vol. 79, pp. 2119–48, Apr 1998.

[86] M. Landers, "Treatment-induced neuroplasticity following focal injury to the motor cortex," *Int J Rehabil Res*, vol. 27, pp. 1–5, Mar 2004.

[87] P. M. Rossini and G. Dal Forno, "Integrated technology for evaluation of brain function and neural plasticity," *Phys Med Rehabil Clin N Am*, vol. 15, pp. 263–306, Feb 2004.

[88] J. W. Krakauer, "Functional imaging of motor recovery after stroke: remaining challenges," *Curr Neurol Neurosci Rep*, vol. 4, pp. 42–6, Jan 2004.

[89] C. Weiller, S. C. Ramsay, R. J. Wise, K. J. Friston, and R. S. Frackowiak, "Individual patterns of functional reorganization in the human cerebral cortex after capsular infarction," *Ann Neurol*, vol. 33, pp. 181–9, Feb 1993.

[90] S. C. Cramer, G. Nelles, R. R. Benson, J. D. Kaplan, R. A. Parker, K. K. Kwong, D. N. Kennedy, S. P. Finklestein, and B. R. Rosen, "A functional mri study of subjects recovered from hemiparetic stroke," *Stroke*, vol. 28, pp. 2518–27, Dec 1997.

[91] R. J. Seitz, P. Höflich, F. Binkofski, L. Tellmann, H. Herzog, and H. J. Freund, "Role of the premotor cortex in recovery from middle cerebral artery infarction," *Arch Neurol*, vol. 55, pp. 1081–8, Aug 1998.

[92] P. M. Rossini, C. Caltagirone, A. Castriota-Scanderbeg, P. Cicinelli, C. Del Gratta, M. Demartin, V. Pizzella, R. Traversa, and G. L. Romani, "Hand motor cortical area reorganization in stroke: a study with fMRI, MEG and TCS maps," *Neuroreport*, vol. 9, pp. 2141–6, Jun 1998.

[93] S. C. Cramer and E. P. Bastings, "Mapping clinically relevant plasticity after stroke," *Neuropharmacology*, vol. 39, pp. 842–51, Mar 2000.

[94] P. Hagmann, M. Kurant, X. Gigandet, P. Thiran, V. J. Wedeen, R. Meuli, and J.-P. Thiran, "Mapping human whole-brain structural networks with diffusion MRI," *PLoS ONE*, vol. 2, p. e597, Jan 2007.

[95] R. S. Desikan, F. Ségonne, B. Fischl, B. Quinn, B. Dickerson, D. Blacker, R. Buckner, A. Dale, R. Maguire, B. Hyman, M. Albert, and R. Killiany, "An automated labeling system for subdividing the human cerebral cortex on mri scans into gyral based regions of interest," *Neuroimage*, vol. 31, no. 3, pp. 968–980, 2006.

[96] R. P. Wang and V. J. Wedeen, "Diffusion toolkit and trackvis," in *15th Annual Meeting of the ISMRM*, 2007.

[97] J. B. A. Maintz and M. A. Viergever, "A survey of medical image registration," *Medical Image Analysis*, vol. 2, no. 1, pp. 1–36, 1998.

[98] J. P. W. Pluim, J. B. A. Maintz, and M. A. Viergever, "Mutual-information-based registration of medical images: A survey," *IEEE Transactions on Medical Imaging*, vol. 22, no. 8, pp. 986–1004, 2003.

[99] A. Gholipour, N. Kehtarnavaz, R. Briggs, M. Devous, and K. Gopinath, "Brain functional localization: A survey of image registration techniques," *IEEE Transactions on Medical Imaging*, vol. 26, no. 4, pp. 427–451, 2007.

[100] M. Wu, L. C. Chang, L. Walker, H. Lemaitre, A. S. Barnett, S. Marenco, and C. Pierpaoli, "Comparison of EPI distortion correction methods in diffusion tensor MRI using a novel framework," *Med Image Comput Comput Assist Interv*, vol. 11, no. Pt 2, pp. 321–9, 2008.

[101] A. Klein, J. Andersson, B. A. Ardekani, J. Ashburner, B. Avants, M.-C. Chiang, G. E. Christensen, D. L. Collins, J. Gee, P. Hellier, J. H. Song, M. Jenkinson, C. Lepage, D. Rueckert, P. Thompson, T. Vercauteren, R. P. Woods, J. J. Mann, and R. V. Parsey, "Evaluation of 14 nonlinear deformation algorithms applied to human brain MRI registration," *Neuroimage*, vol. 46, pp. 786–802, Jul 2009.

[102] E. Heiervang, T. E. J. Behrens, C. E. Mackay, M. D. Robson, and H. Johansen-Berg, "Between session reproducibility and between subject variability of diffusion MR and tractography measures," *Neuroimage*, vol. 33, pp. 867–77, Nov 2006.

[103] C. Granziera, T. Benner, A. Kumar, D. Tuch, A. Singhal, W. Koroshetz, and G. A. Sorensen, "A comparison between diffusion tensor imaging and q-ball MRI in the study of post-stroke plasticity," in *16th meeting of The International Society for Magnetic Resonance in Medicine*, 2008.

[104] M. Nezamzadeh, V. J. Wedeen, R. Wang, Y. Zhang, W. Zhan, K. Young, D. J. Meyerhoff, M. W. Weiner, and N. Schuff, "In-vivo investigation of the human cingulum bundle using the optimization of MR diffusion spectrum imaging," *Eur J Radiol*, Jul 2009.

[105] C. Granziera, J. D. Schmahmann, N. Hadjikhani, H. Meyer, R. Meuli, V. Wedeen, and G. Krueger, "Diffusion spectrum imaging shows the structural basis of functional cerebellar circuits in the human cerebellum in vivo," *PLoS One*, vol. 4, no. 4, p. e5101, 2009.

[106] R. Nieuwenhuys, J. Voogd, and C. van Huijzen, *The Human Central Nervous System: A Synopsis and Atlas.* Springer, December 1988.

[107] P. Hagmann, T. Reese, W. Tseng, R. Meuli, J. Thiran, and V. Wedeen, "Diffusion Spectrum Imaging Tractography in Complex Cerebral White Matter: An Investigation of the Centrum Semiovale," in *International Society for Magnetic Resonance in Medicine, ISMRM TWELFTH SCIENTIFIC MEETING, Kyoto, Japan, 15-21 May 2004*, vol. 12 of *Proc. Intl. Soc. Mag. Reson. Med*, p. 623, International Society for Magnetic Resonance in Medicine, 2004.

[108] E. J. Canales-Rodríguez, Y. Iturria-Medina, Y. Alemán-Gómez, and L. Melie-García, "Deconvolution in diffusion spectrum imaging," *Neuroimage*, vol. 50, pp. 136–49, Mar 2010.

[109] J.-D. Tournier, C.-H. Yeh, F. Calamante, K.-H. Cho, A. Connelly, and C.-P. Lin, "Resolving crossing fibres using constrained spherical deconvolution: validation using diffusion-weighted imaging phantom data," *NeuroImage*, vol. 42, pp. 617–25, Aug 2008.

[110] T. Schultz and H.-P. Seidel, "Estimating crossing fibers: A tensor decomposition approach," *Visualization and Computer Graphics, IEEE Transactions on*, vol. 14, no. 6, pp. 1635–1642, 2008.

[111] L. O'Donnell, S. Haker, and C.-F. Westin, "New approaches to estimation of white matter connectivity in diffusion tensor MRI: Elliptic pdes and geodesics in a tensor-warped space," in *Fifth International Conference on Medical Image Computing and Computer-Assisted Intervention (MICCAI'02)*, (Tokyo, Japan), pp. 459–466, 2002.

[112] O. Ciccarelli, G. J. M. Parker, A. T. Toosy, C. A. M. Wheeler-Kingshott, G. J. Barker, P. A. Boulby, D. H. Miller, and A. J. Thompson, "From diffusion tractography to quantitative white matter tract measures: a reproducibility study," *Neuroimage*, vol. 18, pp. 348–59, Feb 2003.

[113] L.-W. Kuo, J.-H. Chen, V. J. Wedeen, and W.-Y. I. Tseng, "Optimization of diffusion spectrum imaging and q-ball imaging on clinical MRI system," *Neuroimage*, vol. 41, pp. 7–18, May 2008.

[114] C. Grefkes, S. B. Eickhoff, D. A. Nowak, M. Dafotakis, and G. R. Fink, "Dynamic intra- and interhemispheric interactions during unilateral and bilateral hand movements assessed with fMRI and DCM," *Neuroimage*, vol. 41, pp. 1382–94, Jul 2008.

[115] D. Mintzopoulos, L. G. Astrakas, A. Khanicheh, A. A. Konstas, A. Singhal, M. A. Moskowitz, B. R. Rosen, and A. A. Tzika, "Connectivity alterations assessed by combining fMRI and MR-compatible hand robots in chronic stroke," *Neuroimage*, vol. 47 Suppl 2, pp. T90–7, Aug 2009.

[116] R. P. Dum and P. L. Strick, "Motor areas in the frontal lobe of the primate," *Physiol Behav*, vol. 77, pp. 677–82, Dec 2002.

[117] A. Ferbert, A. Priori, J. Rothwell, B. Day, J. Colebatch, and C. Marsden, "Interhemispheric inhibition of the human motor cortex," *J Physiol*, vol. 453, pp. 525–546, 1992.

[118] Z. Ni, C. Gunraj, A. J. Nelson, I.-J. Yeh, G. Castillo, T. Hoque, and R. Chen, "Two phases of interhemispheric inhibition between motor related cortical areas and the primary motor cortex in human," *Cereb Cortex*, vol. 19, pp. 1654–65, Jul 2009.

[119] D. Tombari, I. Loubinoux, J. Pariente, A. Gerdelat, J.-F. Albucher, J. Tardy, E. Cassol, and F. Chollet, "A longitudinal fMRI study: in recovering and then in clinically stable sub-cortical stroke patients," *Neuroimage*, vol. 23, pp. 827–39, Nov 2004.

[120] S. C. Cramer, R. M. Weisskoff, J. D. Schaechter, G. Nelles, M. Foley, S. P. Finklestein, and B. R. Rosen, "Motor cortex activation is related to force of squeezing," *Hum Brain Mapp*, vol. 16, pp. 197–205, Aug 2002.

[121] S. C. Cramer, G. Nelles, J. D. Schaechter, J. D. Kaplan, S. P. Finklestein, and B. R. Rosen, "A functional MRI study of three motor tasks in the evaluation of stroke recovery," *Neurorehabil Neural Repair*, vol. 15, no. 1, pp. 1–8, 2001.

[122] F. Hummel and L. G. Cohen, "Improvement of motor function with noninvasive cortical stimulation in a patient with chronic stroke," *Neurorehabil Neural Repair*, vol. 19, pp. 14–9, Mar 2005.

[123] F. Hummel, P. Celnik, P. Giraux, A. Floel, W.-H. Wu, C. Gerloff, and L. G. Cohen, "Effects of non-invasive cortical stimulation on skilled motor function in chronic stroke," *Brain*, vol. 128, pp. 490–9, Mar 2005.

Publications

Journal papers

- A. Daducci, U. Castellani, M. Cristani, P. Farace, P. Marzola, A. Sbarbati, V. Murino. "Learning approach to analyze tumour heterogeneity in DCE-MRI data during anti-cancer treatment". *Lecture Notes in Computer Science (including subseries Lecture Notes in Artificial Intelligence and Lecture Notes in Bioinformatics)*, 5651 LNAI, pp. 385-389 (2009)

- S. Tambalo, A. Daducci, S. Fiorini, F. Boschi, M. Mariani, M. Marinone, A. Sbarbati, M. Marzola. "Experimental protocol for activation-induced manganese-enhanced MRI (AIM-MRI) based on quantitative determination of Mn content in rat brain by fast T1 mapping". *Magnetic Resonance in Medicine*, 62 (4), pp. 1080-1084 (2009)

- U. Castellani, M. Cristani, A. Daducci, P. Farace, P. Marzola, V. Murino, A. Sbarbati. "DCE-MRI data analysis for cancer area classification". *Methods of Information in Medicine*, 48 (3), pp. 248-253 (2009)

- P. Farace P, M. Galiè, F. Merigo, A. Daducci, L. Calderan, E. Nicolato, A. Degrassi, E. Pesenti, A. Sbarbati, P. Marzola. "Inhibition of tyrosine kinase receptors by SU6668 promotes abnormal stromal development at the periphery of carcinomas". *British Journal of Cancer*, 100 (10), pp. 1575-1580 (2009)

- P. Farace, F. Merigo, S. Fiorini, E. Nicolato, S. Tambalo, A. Daducci, A. Degrassi, A. Sbarbati, D. Rubello, P. Marzola. "DCE-MRI using small-molecular and albumin-binding contrast agents in experimental carcinomas with different stromal content". *European journal of radiology*, Article in press (2009)

- A. Masotti, A. Pitta, G. Ortaggi, M. Corti, C. Innocenti, A. Lascialfari, M. Marinone, P. Marzola, A. Daducci, A. Sbarbati, E. Micotti, F. Orsini, G. Poletti, C. Sangregorio. "Synthesis and characterization of polyethylenimine-based iron oxide composites as novel contrast agents for MRI". *Magnetic Resonance Materials in Physics, Biology and Medicine*, 22 (2), pp. 77-87 (2008)

Conferences

- A. Daducci, X. Gigandet, G. Krueger, L. Cammoun, P. Marzola, P. Hagmann, R. Meuli, J.P. Thiran, C. Granziera. "On the reproducibility and anatomical correspondence of DSI tractography". 16° *annual meeting of the Organization for Human Brain Mapping*, Barcelona, Spain, 6-10 June 2010.

- A. Daducci, N. Sonato, S. Fiorini, S. Tambalo, P. Fattoretti, M. Balietti, A. Sbarbati, P. Marzola. "MRI characterization of brain aging: an experimental study in animals". 1° *annual meeting of the Italian Chapter of the ISMRM*, Milan, Italy, 4-5 February 2010.

- S. Tambalo, S. Fiorini, A. Daducci, P. Fattoretti, M. Balietti, C. Zancanaro, P. Marzola. "fMRI in aging: an experimental study in rats". 26° *ESMRMB*, Antalya, Turkey, 1-3 October 2009.

- V. Colavito, G. Bertini, Y.Z. Xu, A. Daducci, S. Tambalo, S. Fiorini, P. Marzola, G. Grassi-Zucconi, M. Bentivoglio. "A manganese-enhanced (MEMRI) study of sleep and wake. Sleep deprivation points to a role of glial cells in sleep homeostasis". 62° *Congresso Nazionale S.I.A.I. (Società Italiana di Anatomia e Istologia)*, Verona, Italy, 14-16 September 2008.

- V. Colavito, G. Bertini G, Y.Z. Xu, P.F. Fabene, A. Daducci, S. Tambalo, S. Fiorini, P. Marzola, G. Grassi-Zucconi, M. Bentivoglio. "A manganese-enhanced (MEMRI) study of sleep homeostasis". 6° *FENS Forum of European Neuroscience*, Geneva, Switzerland, 12-16 July 2008.

- N. Faccioli, A. Daducci, P. Farace, S. Fiorini, P. Marzola, E. Nicolato, S. Tambalo, A. Degrassi, A. Sbarbati. "Magnevist^{TM}(Gd-DTPA) versus Vasovist^{TM}(MS-325) nella valutazione con DCE-MRI della angiogenesi tumorale in tumori pancreatici e prostatici impiantati nel topo". 43° *Congresso SIRM (Società Italiana di Radiologia Medica)*, Rome, Italy, 23-27 May 2008.

- S. Tambalo, S. Fiorini, A. Daducci, F. Boschi, E. Nicolato, P. Marzola. "Quantitative determination of Mn content in rat brain by Fast T1 mapping". *Proceedings of the Joint Annual Meeting ISMRM-ESMRMB*, Berlin, Germany, 19-25 May 2007.